**UC San Diego**
**UC San Diego Electronic Theses and Dissertations**

**Title**
New Constraints on Strain Partitioning Across Southern California's Diffuse Plate Boundary

**Permalink**
https://escholarship.org/uc/item/5692s0w6

**Author**
Derosier, Boe Jay

**Publication Date**
2022

Peer reviewed|Thesis/dissertation

eScholarship.org
Powered by the California Digital Library
University of California

UNIVERSITY OF CALIFORNIA SAN DIEGO

# New Constraints on Strain Partitioning Across Southern California's Diffuse Plate Boundary

A dissertation submitted in partial satisfaction of the requirements

for the degree Doctor of Philosophy

in

Earth Sciences

by

Boe Jay Derosier

Committee in charge:

Professor Neal Driscoll, Chair
Professor James Day
Professor Falko Kuester
Professor Ross Parnell-Turner
Professor David Sandwell

2022

©

Boe Jay Derosier, 2022

All rights reserved.

The dissertation of Boe Jay Derosier is approved, and it is acceptable in quality and form for publication on microfilm and electronically.

University of California San Diego

2022

# DEDICATION

To

My Mother

For showing me that with dedication and perseverance

anything is possible.

My Father

For showing me how to see and bring out the best

in those around me.

# EPIGRAPH

I have made this longer than usual because,
I have not had time to make it shorter.

Blaise Pascal

# TABLE OF CONTENTS

# LIST OF FIGURES

# ACKNOWLEDGEMENTS

I want to start by recognizing my advisor Neal Driscoll, who saw my potential and provided me with guidance, freedom, and tools to grow and mature as a scientist. I will be forever in his debt for this life-changing opportunity.

I also would like to take the opportunity to thank my committee,  James Day, Dave Sandwell, Ross Parnell-Turner, and Falco Kuester, for participating in these early stages of my academic career.

Special thanks to Dan Orange, Lee Ellett, and Bruce Appelgate for allowing me to sail on the R/V Sally Ride's sonar commissioning cruise and the front-row seat to the future of marine geoscience.

I want to thank the faculty of SIO, James Day, Lisa Tauxe, Geoff Cook, Peter Lonsdale, Jeff Gee, Pat Castillo, and Kevin Brown. They have provided the solid geologic foundation my academic laurels firmly rest.

Next, I would like to recognize and thank all the lab mates and shipmates I have had through the years, especially Jillian Maloney, Valerie Sahakian, James Holmes, Shannon Klotsko, Hector Perea, Jayne Borman, and Drake Singleton, for being sounding boards and exceptional role models to emulate. I would also like to thank Brendon Mendenhall, Colby Nicholson, Brian Oller, Daniel Schwartz, Aaron Hagadorn, Mackenzie Roberts, Lana Graves, Leanne Hirsch, and James Futty. Your friendship and camaraderie will always be treasured.

I would like to thank my family for the love and support during my journey as a graduate student; I would not have been able to do it without you.

Finally, I would like to acknowledge my partner Mackenzie Roberts, who has been my rock through this long journey. She has provided me with emotional support, stability, and freedom to pursue my dreams. However, most importantly, she has motivated and given me the confidence to continue moving forward, and for that, I will be forever grateful.

Chapter 2 will be resubmitted for publication in: Derosier, B.J., Driscoll, N.W., In-Prep. Uplift and Subsidence of the Inner California Borderland Constrained by Abrasion Platforms. *Geosphere.* The dissertation author is the primary researcher and author, and the co-author listed in this manuscript directed and supervised this research.

Chapter 3 Derosier, B.J., Driscoll, N.W., Seismic facies analysis of the Catalina Basin; Implications of the Evolution of The Inner California Borderland. The author of the dissertation was the primary researcher and author of this manuscript. This manuscript is not currently ready for publication as further data is needed. Additional ship-time is necessary to collect high-resolution sub-bottom data scheduled for August 2022 onboard the R/V Sally Ride.

Chapter 4 is being prepared for publication in: Derosier, B.J., Driscoll, N.W., In Prep. New High-Resolution Sub-bottom Profiler Resolves Active Deformation Within the Outer California Borderland. *Geophysical Research Letters.* The author of the dissertation is the sole researcher and author of this publication.

Chapter 5 has been accepted for publication in: Sahakian, V.J., Derosier, B.J., Rockwell, T.K., Stock, J.M., Accepted. Shallow Distributed Faulting in the Imperial Valley. *Geology*. The dissertation author was involved in the acquisition, interpretation, and manuscript preparation that forms the basis of this chapter. The author of the dissertation is the secondary author of this publication.

# VITA

2005-2012 U.S. Navy

2014 Bachelor of Science, University of California San Diego

2014-2018 Teaching Assistant, University of California San Diego

2018 Master of Science, University of California San Diego

2018-2021 Research Assistant, University of California San Diego

2022 Doctor of Philosophy, University of California San Diego

## PUBLICATIONS

Derosier, B.J., Driscoll, N.W., In-Prep. Uplift and Subsidence of the Inner California Borderland Constrained by Abrasion Platforms. *Geosphere.*

Sahakian, V.J., Derosier, B.J., Rockwell, T.K., Stock, J.M., Accepted. Shallow Distributed Faulting in the Imperial Valley. *Geology*.

Derosier, B.J., Driscoll, N.W., In Prep. New High-resolution Sub-Bottom Profiler Resolves Active Deformation Within the Outer California Borderland. *Geophysical Research Letters.*

## FIELDS OF STUDY

Major Field: Earth Sciences

Studies in Marine Geology

Professor Neal Driscoll

## ABSTRACT OF THE DISSERTATION

# New Constraints on Strain Partitioning Across Southern California's Diffuse Plate Boundary

by

Boe Derosier

Doctor of Philosophy in Earth Sciences

University of California San Diego, 2022

Professor Neal Driscoll, Chair

Geologic observations provide an important lens to objectively view the natural world and contextualize the processes that have and continue to shape Earth's brittle crust. As a result, many geologic and geophysical tools have been developed. This dissertation uses high-resolution sub-bottom and multi-channel seismic data to observe sequence stratigraphic and morphologic signatures of deformation encoded into Southern California and its offshore component, the California Continental Borderland (CCB).

Using geophysical tools, this dissertation first investigates the vertical displacement history of the Inner California Borderland (ICB) using marine terraces. By Imaging marine terraces with sub-bottom profilers offshore San Clemente and Santa Catalina Islands and contextualizing them with legacy on and offshore data, it is possible to extend our current Quaternary understanding of the vertical displacement history of the ICB through to the Middle Miocene. In addition, this model provides a framework for the formation of disputed marine terraces observed at depths deeper than the Last Glacial Maximum (LGM).

Second, I conducted a seismic stratigraphic analysis of the Catalina Basin, one of the many basins that make up the ICB, to constrain the late Cenozoic evolution of the region and put into context basin-wide markers of historic relative sea level with regional geology.

Third, this dissertation outlines the use of the Kongsberg SBP 29, recently installed on the R/V Sally Ride in June of 2021, to image and characterize active deformation within the Outer California Borderland (OCB). The OCB, a relatively under-surveyed region within the CCB, has not been widely recognized as accommodating active deformation. Interpretation of the high-resolution sub-bottom data is constrained by proximal Ocean Drilling Project cores. As a result, it is possible confidently report that the Ferrelo Fault has been active within the last 1,000 years, accommodating Pacific/North American relative strain.

Lastly, the novel use of a sub-bottom profiler is employed, typically a marine and or lacustrine instrument, to image onshore deformation along an unlined section of the All-American Canal. This survey images deformation within the Imperial Valley, along the Imperial,

Dixieland, and Michoacán Faults, in an area where anthropogenic activity has otherwise made direct observations of surface deformation difficult.

# Chapter 1

# Introduction

Plate tectonic theory posits that Earth's brittle crust comprises numerous ridged plates. Over geological time, these plates have been and continue to be dynamically displaced around the surface of the Earth through density contrasts and viscous coupling between the Earth's crust and the convecting mantle. These ridged plates primarily deform along their borders, generally described as convergent, divergent, and transform plate boundaries. Observations made along these deformational boundaries provide insight into the many processes that shape the Earth's surface. One of the objectives of Earth Science is to study and characterize how the Earth deforms along active plate boundaries. These observations provide context for unsettled academic questions of uniformitarianism and, more importantly, provide insight into seismic hazard, which is of significant socioeconomic importance to populations living along active plate boundaries, such as Southern California, as well as economic interests related to natural resources.

Southern California and its offshore component, the California Continental Borderland, provide an important case study with which to observe how strain has been accommodated along an actively deforming margin. Signatures of all deformation styles mentioned above have been recorded in the morphology and geology of the region, as the region transitioned from a convergent to divergent and now transform boundary over the last 30 million years (My). Before 30 million years ago (Ma), Farallon plate subduction dominated the western margin of North America and is notably recorded by Mesozoic plutonism observed through Southern California

(Glazner, 1991) and the Catalina-Schist belt (Grove et al., 2008), an inverted metamorphic sequence emplaced through subduction-related processes. At around 30Ma, Farallon subduction began to stall as hot and increasingly buoyant and young ocean crust fresh from the proximal Pacific-Farallon Ridge became progressively harder to subduct under the western margin of North America (Atwater, 1970; Lonsdale, 1991; Bohannon and Parsons, 1995). Subduction under what is now Southern California and the concomitant Pacific-Farallon Ridge activity ceased at ~20Ma, resulting in large-scale extension of the once active forearc, imparting much of the offshore submarine morphology we observe today (Bohannon and Geist, 1998). During this, approximately 5 million year period of regional extension, transtension, and microplate capture resulted in >90º clockwise rotation of the Western Transverse Range (Luyendyk et al., 1980; Hornafius et al., 1986; Nicholson et al., 1994; Levi and Yeats, 2003). A consequence of this >90º clockwise rotation was large-scale regional unroofing that exposed the Catalina Schist Belt to Middle Miocene hemipelagic sedimentation (Grove et al., 2008). Following the stage of extension and rotation (20 to 15 Ma), a noticeably less dynamic deformation stage dominated the region (15 Ma to present), characterized by NW-SE dextral faulting along the many troughs going faults within this diffuse plate boundary, but associated with regional volcanism (Dickinson, 1997).

Today the Catalina Schist Belt, also referred to as the Inner California Borderland, together with onshore Southern California through a stable North American Plate, geodetically account for ~44mm/yr of dextral motion, ~92% of the total (~48mm/yr) Pacific-North American (PNA) plate relative motion (Kreemer et al., 2010; Platt and Becker, 2010; Walton et al., 2020). How and where the 48mm/yr of dextral motion is accommodated is still an active field of research. Currently, the ICB and the onshore region, which includes the San Andreas Fault, account for 92% of the total PNA relative plate motion, leaving a critical and currently outstanding question of where the other 8% (~4 mm/yr) might be.

Despite there being 8% of the total PNA relative plate motion unaccounted for, the lateral Quaternary deformation history of the region is relatively well constrained; the same can also be said regarding the vertical Quaternary deformational history for the region. Quaternary marine terraces are distinct features along Southern California's coastline. They are records of a long-lived coastal uplift rate of ~0.13 m/ky, derived from carbonate fossils found on subaerial marine terraces (Kern and Rockwell, 1992a; Muhs et al., 2014; Haaker et al., 2016). Flank uplift from rifting of the Salton Trough has been used to explain the observed coastal uplift (Mueller et al., 2009). However, despite rift flank uplift being a reasonable explanation for the well documented coastal uplift, it does not explain the marine terraces observed on the offshore islands within the ICB that have analogous uplift rates (~0.13 m/ky)(Muhs and Szabo, 1982; Adler, 2003; Muhs et al., 2012; Muhs and Groves, 2018). Furthermore, Quaternary constrained subaerial marine terraces place important temporal constraints for the timing of submerged marine terraces observed above and below the regional depths (~95 mbsl) of the Last Glacial Maximum (LGM)(Muhs et al., 2012).

There are still many questions regarding how vertical and horizontal strain has and is currently being accommodated within this actively deforming margin. However, it is possible to demonstrate here that sub-bottom profilers provide the resolution, and sequence stratigraphy provides the context required to resolve important characteristics of deformation as well as important proxies of deformation. The observations within this dissertation have implications for the geologic evolution of Southern California, California Continental Borderland, and the region's seismic hazard, home to >20 million residents.

## 1.1 Outline of the Dissertation

This dissertation focuses on the historic and active deformation within onshore Southern California and its offshore component, the California Continental Borderland. The tectonic processes that have and continue to shape this diffuse plate boundary are investigated sub-bottom profilers coupled with multibeam bathymetry, legacy seismic, geochemical, fossil, and geodetic data.

Chapter 2 explores the morphologic signatures of paleo sea-level fluctuations known as marine terraces within the California Continental Borderland. Using sub-bottom profilers, it is possible to map multiple submarine terraces at or above regional Last Glacial Maximum (LGM) depths (~95 mbsl) (Muhs et al., 2012), that likely represent Quaternary interglacial sea-level still stands. It is also possible to map submarine terraces below LGM sea levels that are not consistent with Quaternary sea-level processes, which may serve as a record of pre-Quaternary relative sea-level fluctuations. The manuscript associated with Chapter 2 has been submitted to *Geosphere* for publication but was not accepted. However, recent observations made on Santa Catalina Island by McInnis and Pinter (2021) support the conclusions of this manuscript. Therefore, we will resubmit as soon as possible.

In Chapter 3, we characterize Late Cenozoic deformation within the Catalina Basin. Utilizing multi-channel seismic data collected within the Inner California Borderland, we identify, map, and put into context basin-wide unconformities to constrain the tectonic and relative sea-level histories of the Catalina Basin. Observations of the stratigraphic framework within the Catalina Basin support a two-stage evolution model for the basin, constrained by regional geologic observations. This manuscript is awaiting more data, scheduled to be collected in summer 2022.

Chapter 4 images and characterize tectonic deformation within the Outer California Borderland, a relatively under-surveyed region within the diffuse North American Pacific Plate boundary. We use a new, high-resolution sub-bottom profiler recently installed on the R/V Sally Ride (June 2021) to image surface and subsurface deformation along the Ferrelo Fault within the South Tanner Basin. These observations provide robust evidence of active deformation along a fault that has not been widely accepted as being active and, consequently, not been used to inform Southern California's seismic hazard. This manuscript is being prepared and will be submitted for publication in *Geophysical Research Letters* as soon as possible.

In Chapter 5, we image and characterize tectonic deformation below an unlined section of the All-American Canal through the novel application of a high-resolution sub-bottom profiler, an instrument typically used in marine and or lacustrine environments. We image sub-surface deformation attributable to the Imperial, Dixieland, and Michoacán Faults in a region where anthropogenic activities have made direct surface observations difficult. This manuscript was published in *Geology* March 2022.

# Chapter 2

# Uplift and Subsidence of the Inner California Borderland Constrained by Abrasion Platforms

## 2.1.0 Abstract

Recently acquired seismic reflection data images submarine terraces that constrain the Late Cenozoic vertical displacement history of the Inner California Borderland (ICB). These new constraints provide a chronostratigraphic framework for the formation of disputed geomorphological features of the ICB. The surface and subsurface morphology within the broad shelf around San Clemente Island (SCI) exhibits multiple paleo shoreline features associated with marine terraces. Submerged marine terraces at ~95 meters below sea level (mbsl) appear to correlate with the local relative sea-level depth of the Last Glacial Maximum (LGM) and are consistent with the reported Quaternary uplift rate for SCI (0.13m/ky). Terraces deeper than the local LGM levels (~95 mbsl) are observed offshore SCI and Santa Catalina Island (CI). Previous researchers have interpreted these deeper terraces as Quaternary in age; such an interpretation requires recent subsidence to explain their depths that are greater than local LGM sea levels. The differential subsidence, faulting, and tilting purported to explain the depths of deeper terraces are not observed in seismic data. Knudsen sub-bottom profiler data recently collected off CI image what is interpreted as a prograding low stand wedge that downlaps onto a deeper terrace (255

mbsl). Based on recently collected seismic reflection data coupled with legacy seismic reflection, bathymetric, geochemical, petrological, and macrofossil data, we propose that the abrasion platforms observed below ~95mbsl are Middle to Late Neogene in age and were formed by extensional unloading and uplift that was followed by thermal subsidence. A renewed phase of regional uplift occurred in the Early Pleistocene, giving rise to the observed subaerial terraces in and around the ICB.

## 2.2.0 Introduction

The California Continental Borderland (CCB), comprised of numerous basins bounded by NW-SE trending ridges and faults, is a prominent morphological domain along the margin of the Southern California coast. Pervasive NW-SE dextral faulting observed throughout the Inner California Borderland (ICB), and Outer California Borderland (OCB) contrasts with the W-E sinistral faulting of the Western Transverse Range (WTR) (Figure 2.1). The lateral displacement of the ICB has been constrained by numerous onshore and offshore geophysical, geologic and geodetic studies (Darigo and Osborne, 1986; Legg, 1991; Lindvall and Rockwell, 1995; Hogarth et al., 2007; Ryan et al., 2009; Platt and Becker, 2010; Le Dantec et al., 2010; Brothers et al., 2015; Maloney et al., 2016a; Gold et al., 2017; Walton et al., 2020). In addition, quaternary vertical displacement rates for the ICB and the Southern California Coast are reasonably well constrained (Kern and Rockwell, 1992b; Muhs et al., 1992, 1994, 2021; Mueller et al., 2009; Schumann et al., 2012; Haaker et al., 2016; Castillo et al., 2019; McInnis and Pinter, 2021), however, there are various models employed to explain the offshore morphology.

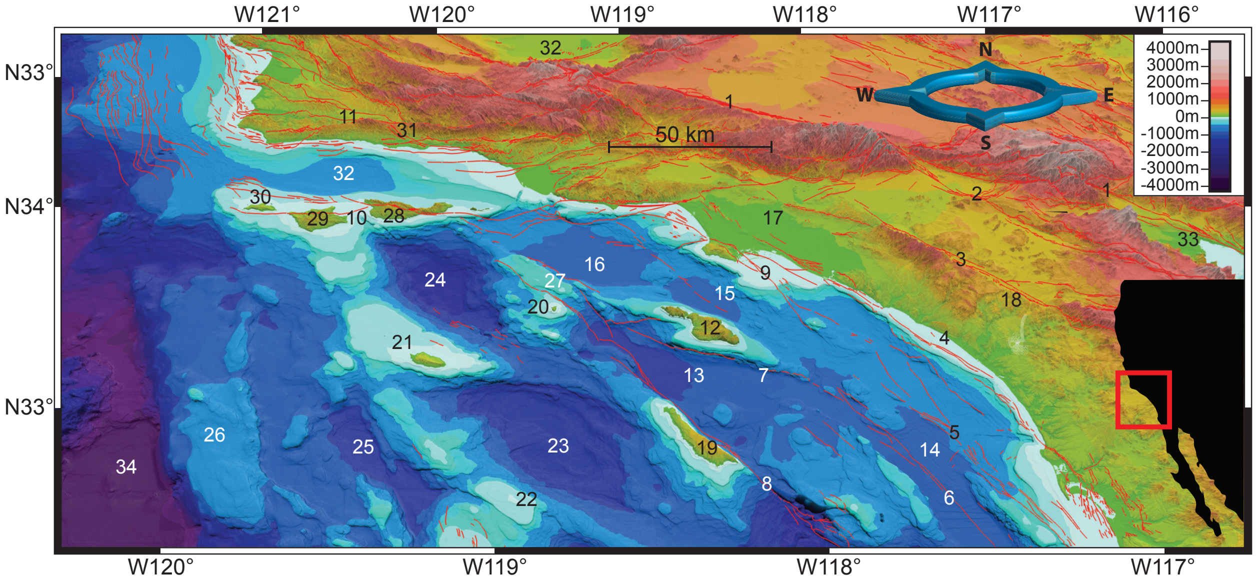

Figure 2.1 3D perspective of the California Continental Borderland looking North.

The California Borderland dissected by numerous NW trending faults (red lines #1 San Andreas Fault Zones, #2 San Jacinto Fault Zone, #3 Elsinore Fault Zone, #4 Newport Inglewood – Rose Canyon Fault Zone, #5 Coronado Bank Fault zone, #6 San Diego Trough Fault Zone, #7 Catalina Fault, #8 San Clemente Fault Zone, #9 Palos Verdes Fault Zone, #10 Santa Cruz Island Fault, #11 Santa Ynez Fault Zone, (U.S. Geological Survey)) have been shaped by 26.5 My of dextral oblique extension. The Inner California Borderland (ICB), also known as the Catalina Schist Belt, is located inboard of the San Clemente fault (#12 Santa Catalina Island, #13 Catalina Basin, #14 San Diego Trough, #15 San Pedro Basin, #16 Santa Monica Basin, #17 Los Angeles Basin, #27 Pilgrim Banks) and outboard of the (#18) Peninsular Range. The Outer California Borderland (OCB), known as Nicolas Forearc Belt (#19 San Clemente Island, #20 Santa Barbra Island, #21 San Nicholas Island, #22 Tanner Bank, #23 San Nicholas Basin, #24 Santa Cruz Basin, #25 Tanner Basin) is analogous to the (#32) Great valley sequence of Central California and is flanked to the West by the (#26) Patton Accretionary Belt, a remnant subduction wedge, comparable to the Franciscan complex (Bohanon and Geist; 1998) and the (#34) Pacific Plate. The Western Transverse Range (WTR) to the North (#28 Santa Cruz Island, #29 Santa Rosa Island, #30 San Miguel Island, #31 Santa Ynez Mountains, #32 Santa Barbara Basin) is an enigmatic region of the California Continental Borderland, where it is theorized the WTR has rotated coherently CCW more than 90 degrees during the Miocene. Topo bath from (NOAA- NGDC, 2003).

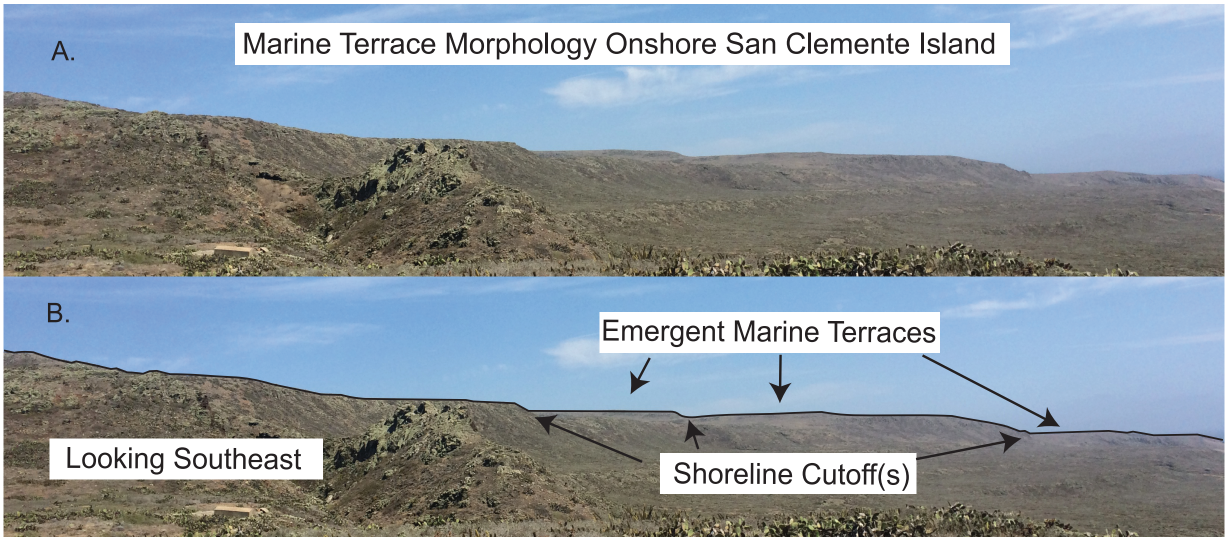

Figure 2.2 A. Emergent marine terraces on San Clemente Island (looking southeast).

B. marine terrace morphology along the western slope of SCI.

Marine terraces and their respective shoreline cutoffs are excellent vertical fiducial markers for studying Quaternary uplift and subsidence along coastal margins (Figure 2.2). Marine terraces, the result of wave-based erosion and scouring during times of diminished relative sea-level (RSL) change, have been used by researchers to constrain North American Quaternary shoreline uplift and subsidence rates along much of the West Coast and offshore California Continental Borderland (Muhs and Szabo, 1982; Muhs, 1983, 2002; Kern and Rockwell, 1992b; Muhs et al., 1994, 2012, 2014; Chaytor et al., 2008; Haaker et al., 2016; Castillo et al., 2019). Unfortunately, the processes that scour marine terraces into their characteristically flat

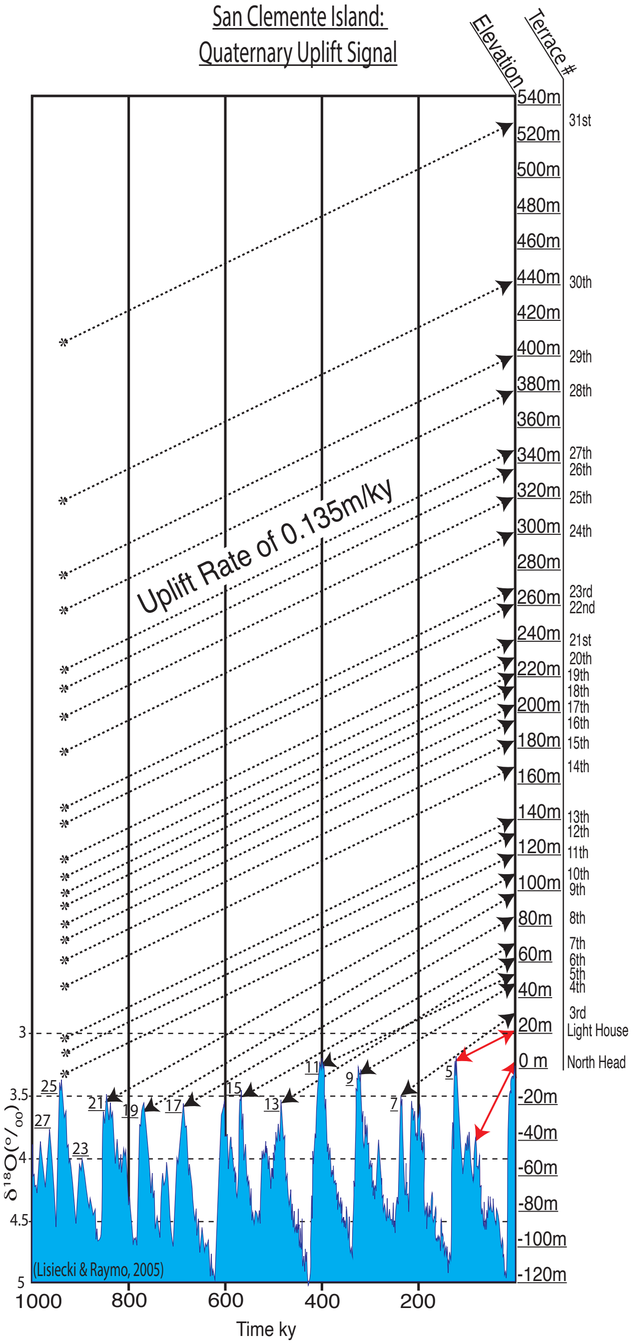

Figure 2.3 Observed uplift signal is derived from the emergent marine terrace on SCI.

Dated (bold red) and correlated (black dash) terrace regressions suggest SCI uplift (0.135m/ky), post - 3Ma to 4Ma (Adler, 2003). Terrace elevations and respective numbers are recorded along the vertical axis (Adler, 2003), and the benthic marine isotope stack of Lisiecki & Raymo (2005) is displayed on the horizontal axis, MIS interglacials 5-27 are numbered. Asterisks represent regressions of marine terraces that were formed before MIS 27.

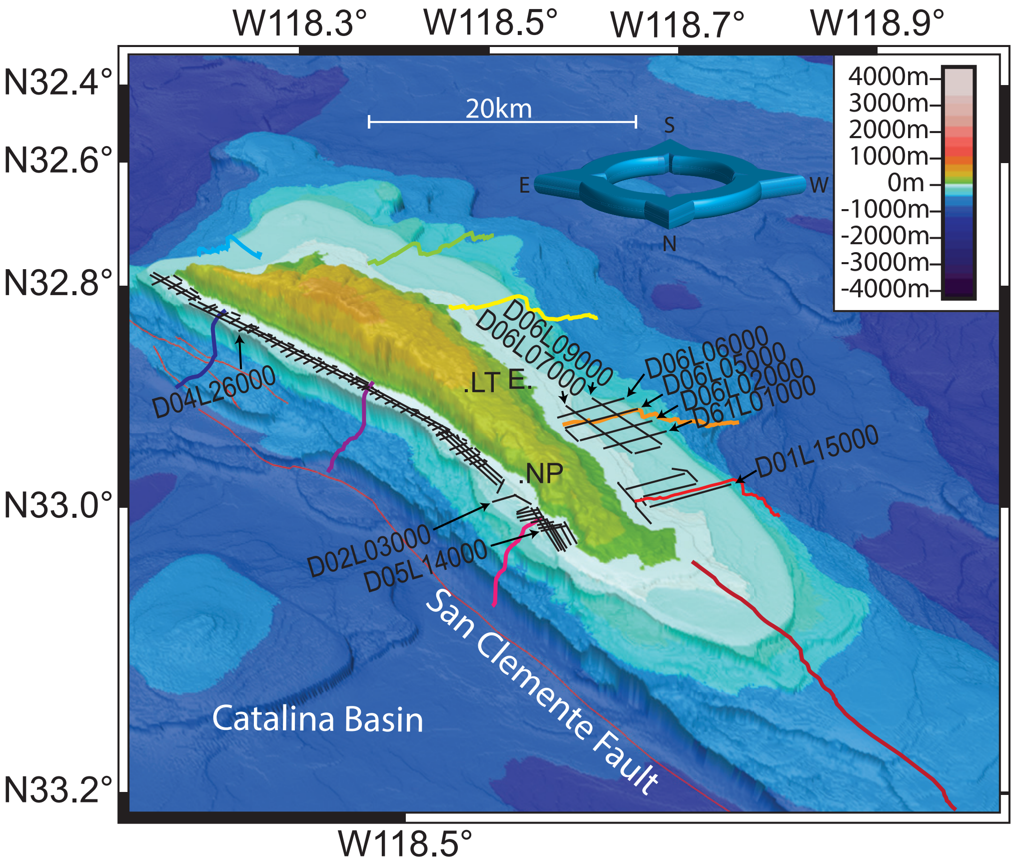

Figure 2.4 3D perspective view looking South.

San Clemente Island (SCI) is noticeably asymmetrical, with its steep eastern cliff, the emergent trace of the San Clemente Fault, and its gently dipping western side that exhibits 31 pristine marine terraces. Eel Point (E) is the borehole location of the discontinuous suite of mid-Miocene volcanics collected on SCI (Merifield et al., 1971). The Lemon Tank (LT) site is the location of crucial fiducial marks in SCI's tectonic history (Vedder, 1976). Anomalously shallow marine terraces are imaged within the NOTS pier area (NP). CHIRP profiles collected in summer 2015 onboard the R/V Point Loma are indicated in black. Color-coded profiles are shown in Figure 2.7.

(~1-2°) terrace morphology is predominantly erosive, leaving little dateable material for age constraints.

Carbonate secreting fauna that exploit the intersection of the photic and littoral zones along these wave-cut platforms are preserved when coastal uplift sequesters these fossils on subaerial marine terraces. Conversely, carbonate secreting fauna that are not sequestered on subaerial marine terraces remains in the littoral zone where they are broken down, reworked, and

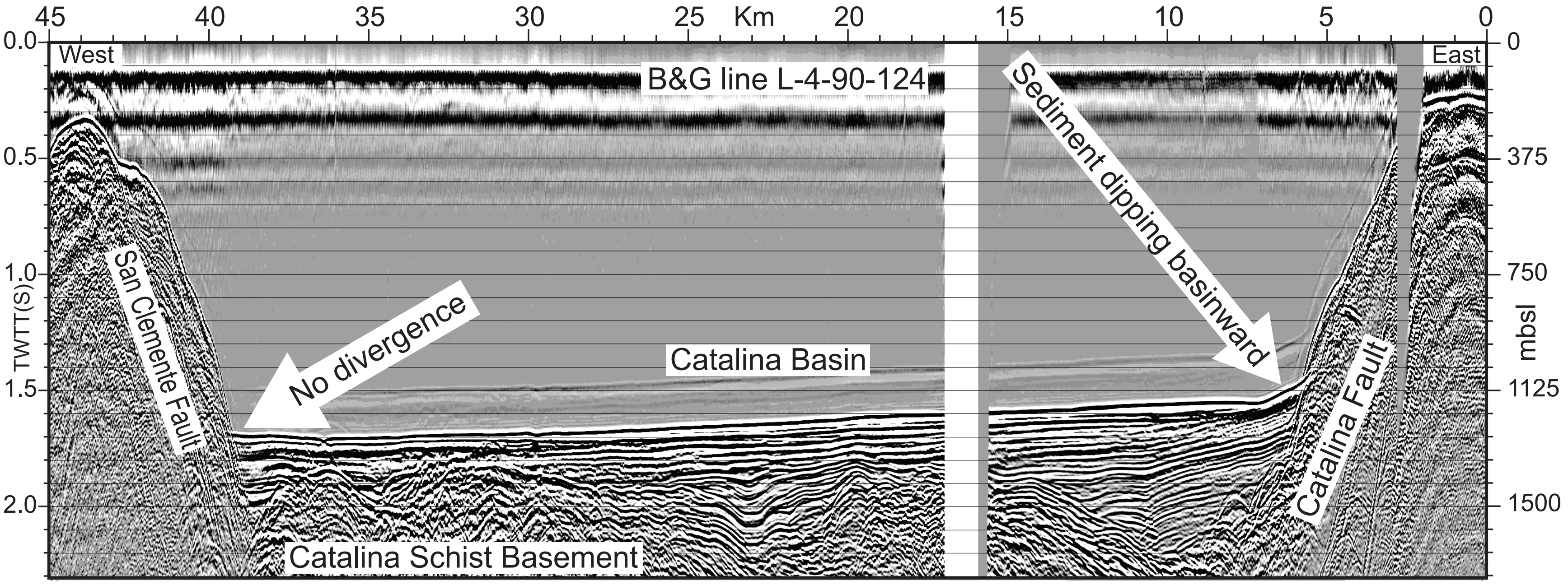

Figure 2.5 Multi-Channel Seismic line (See Figure 6 for location)

L-4-90-124 collected in 1990 (Bohanon & Geist, 1998) to constrain Borderland Neogene extension, show no observable post-Miocene divergence along the San Clemente Fault (SCF) bounding the Catalina Basin to the West. This MCS seismic data also images sediments dipping away from the SCF. (https://walrus.wr.usgs.gov/infobank/l/l490sc/html/l-4-90-sc.meta.html) ultimately transported by wave action alongshore and downslope, leaving a dearth of reliable, datable material. Almost all of the recorded vertical displacement rates within the ICB are constrained by subaerial marine terraces and have yielded comparable uplift rates of 0.13-0.2 m/ky referred to herein as the "regional uplift signal" (Muhs and Szabo, 1982; Kern and Rockwell, 1992b; Muhs, 2002; Adler, 2003; Muhs et al., 2014; Haaker et al., 2016). Exceptions to the regional uplift signal fall into two main categories. The first exception is local tectonic processes due to active thrusting or faulting, the Santa Barbara Fold Belt (Gurrola et al., 2014),

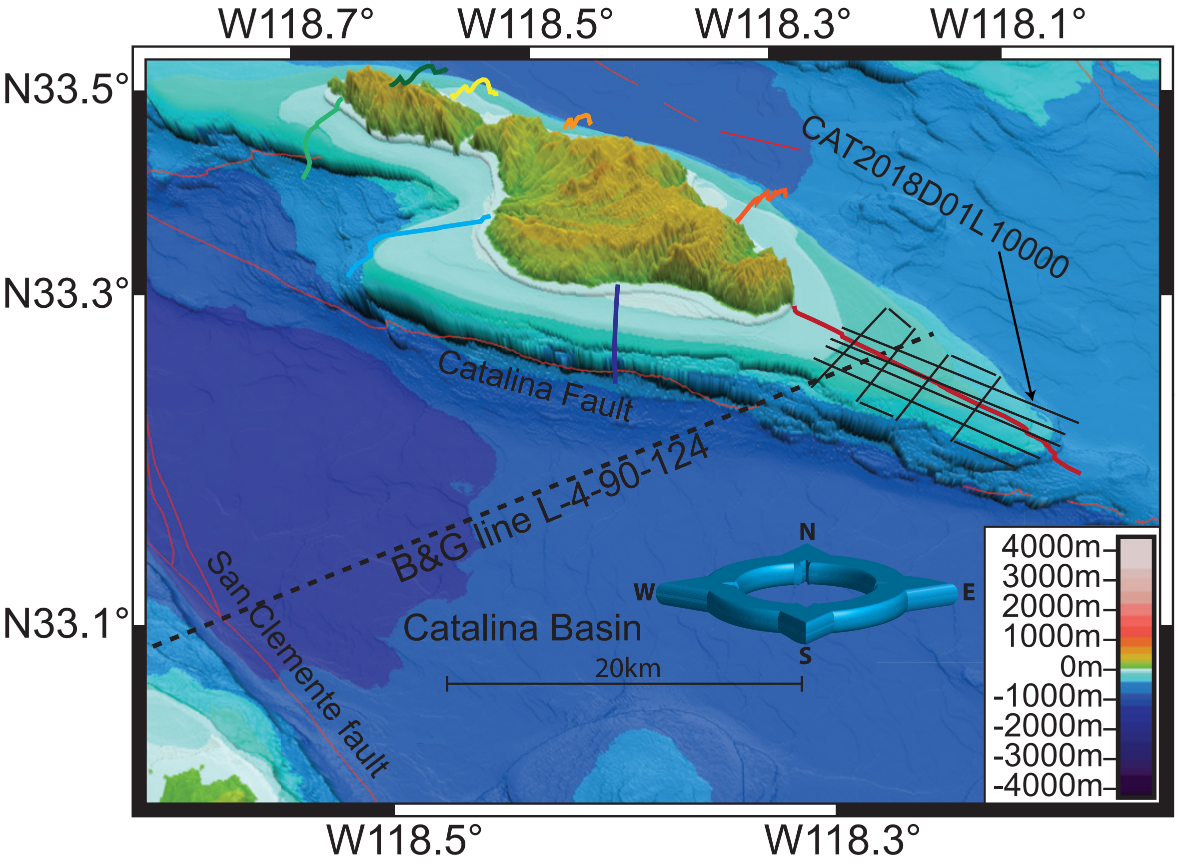

Figure 2.6 3D prospective view of Catalina Island looking North.

Knudson 3.5khz echo sounder profiles collected offshore Santa Catalina Island (CI) are highlighted in black. B&G line L-4-90-124 is highlighted with a dashed line, and the color-coded profiles are highlighted in Figure 7. Red faults are from the USGS fault catalog.

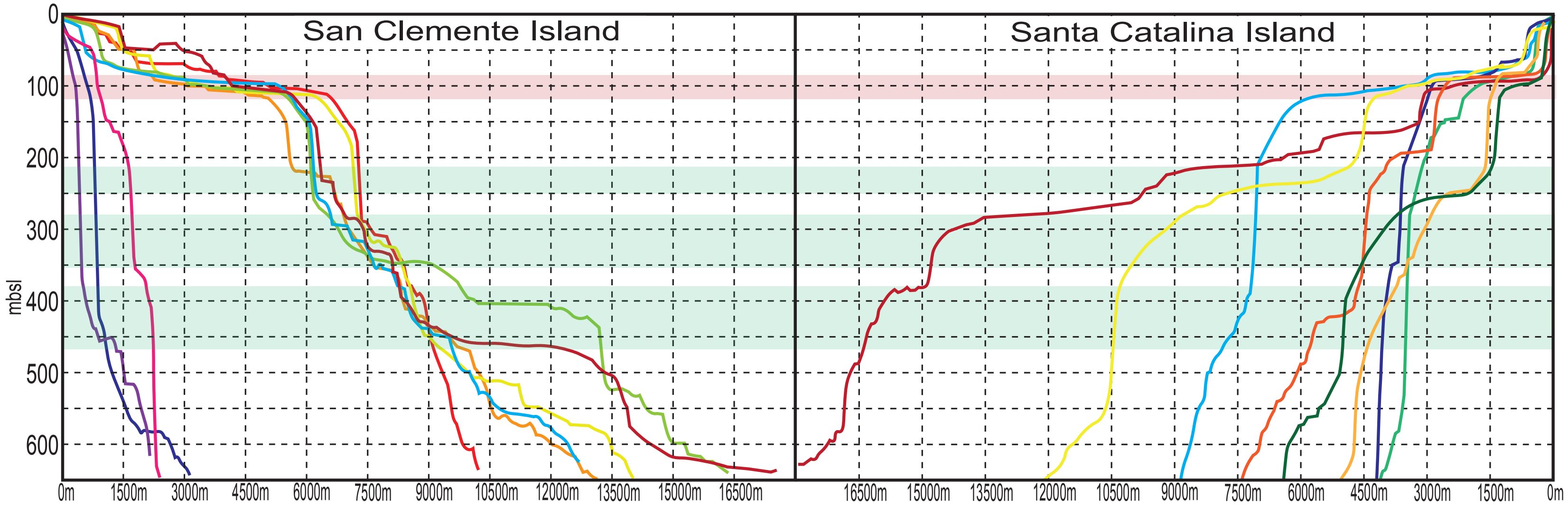

Figure 2.7 Cross-section profiles extracted from bathymetry data

(NOAA- NGDC, 2003)(https://www.ncei.noaa.gov) appear to image multiple scouring events (see Figures 4 & 6 for profile locations). The bathymetry data also suggest terraces below the depth of regional LGM (95mbsl). Highlighted green are depths where marine terraces are observed and inferred on both islands. Given the observed emergent terraces and Quaternary eustatic sea-level models, these terraces appear older than the Quaternary.

the Palos Verdes Hills (Muhs et al., 1992), and Punta Banda in northern Baja California (Rockwell et al., 1989) are a few notable examples. The second group of uplift rates outside the regional uplift signal is derived from samples collected from submerged marine terraces. Datable material collected from submerged marine terraces has resulted in reported uplift rates for the Northern Channel Islands (NCI) that are an order of magnitude higher (1.5 ± 0.59 m/ky, Chaytor et al., 2008) than the regional uplift signal recorded by the onshore NCI terraces (Muhs et al., 2014). Datable material collected from submerged marine terraces has also resulted in subsidence rates of 0.08- 0.27m/ky and 0.3m/ky for Santa Catalina Island (CI) and Pilgrim Banks (PB), respectively (Castillo et al., 2019). The attendant deformation required to explain subsidence and uplift rates derived from submerged samples are not observed in regional seismic data (Francis et al., 2019).

To calculate vertical displacement rates using subaerial marine terraces a chronostratigraphic framework is established by first dating corals (U-Th) on emergent marine terraces and comparing the calculated coral ages with their respective Marine Isotopic Stage (MIS; Figure 2.3; Fairbanks, 1989; Lisiecki and Raymo, 2005; Thompson and Goldstein, 2006). Observed differences in the elevation of the dated marine terraces and respective height of the identified MIS are attributed to uplift or subsidence of the region (Muhs & Szabo, 1982; Bull, 1994).

Submarine terraces below RSL of the Last Glacial Maximum (LGM) (~95 meters below sea level (mbsl)), Muhs et al., 2012) within the ICB have been identified by Emery (1958), Ridlon (1972), Chaytor et al. (2008), Castillo et al. (2018) and others with vastly different explanations for their formation. Emery (1958) highlights the existence of marine terraces below the LGM eustatic low stand, and as such, he suggested that they predate the emergent Quaternary terraces observed in and around the ICB. Conversely, others have suggested that these deeper terraces correlate with the LGM or other glacial maximums of the Quaternary (Ridlon, 1972; Chaytor et al., 2008; Castillo et al., 2019). The implication of Quaternary marine terraces at depths below the LGM low stand (~ 95 mbsl) implies that isolated localities within the ICB have subsided, slumped, or tilted. Here, we present new high-resolution CHIRP data collected offshore San Clemente Island (SCI) and CI and existing legacy data to test these two alternative hypotheses for the formation of the marine terraces found at depths deeper than LGM (~ 95 mbsl). Understanding the processes that engender vertical displacement of the ICB have important implications for other actively deforming margins, specifically being able to differentiate between localized effects due to constraining and releasing bends from more regional processes such as in-plane force (Karner et al., 1993). Furthermore, understanding the character and style of uplift and basin formation within these settings has societal relevance, as these basin-forming processes control the distribution of hydrocarbons, sand reservoirs, and aquifers.

## 2.3.0 Regional Setting

### 2.3.1 California Borderland

The morphology of the western margin of Southern California is a record of the dynamic transition from a convergent margin with episodes of dextral and sinistral deformation (Glazner, 1991) >30 Ma to the dextral transform margin active today (Bohannon and Geist, 1998). The California Continental Borderland (CCB) dynamic transition is widely attributed to the eastward migration and collision of the East Pacific Rise (EPR) with the North American plate; the inner buoyancy forces of the subducted plate, fresh from the EPR stalling subduction and ridge spreading (Atwater, 1970; Severinghaus and Atwater, 1990; Lonsdale, 1991). Without the presence of an actively spreading EPR west of the Southern Californian margin, far-field forces related to the Pacific Plate subduction to the Northwest, along with triple junction migration, engendered oblique extension (NW-SE ) of the previously active subduction forearc (Atwater, 1970; Bohannon and Parsons, 1995; Bohannon and Geist, 1998).

The OCB is likely to be relatively intact, comprised of an accretionary wedge and forearc sediments analogous to the Franciscan Subduction Complex and the Great Valley Forearc Sequence observed along most of the Central California Coast (Bohannon and Geist, 1998). Bohanon and Geist (1998) proposed a robust two-stage extension model for the California Continental Borderland based on multichannel seismic data, constrained by the Ocean Drilling Program (ODP) cores (Leg 167) and industry wells. The dynamic first stage of rifting caused much of the observed morphology and culminated in widespread volcanism throughout the American Southwest ~15Ma (Cole and Basu, 1995; Dickinson, 1997), exposing the Catalina Schist Belt that is also referred to as the ICB (Bohannon and Parsons, 1995; Bohannon and Geist, 1998; Rivero et al., 2000). The second stage, notably less dynamic than the first, consists primarily of dextral slip along the NW-SE trending faults of the ICB, which currently accommodate between 10% and 20% of the displacement between the Pacific and North American Plates (Legg, 1991; Platt and Becker, 2010; Walton et al., 2020).

### 2.3.2 San Clemente Island

The marked asymmetry of SCI (Figure 2.4) suggests it is the uplifted crustal footwall from active faulting (Ward and Valensise, 1994). The steep leeward (eastern) side, which is also the scarp of the San Clemente Fault (SCF), contrasts with the gently dipping windward (western) side of the island. The west slope of SCI exhibits 31 of the best-preserved marine terraces observed along the California coast (Muhs and Szabo, 1982; Adler, 2003).

The result of numerous significant prolonged volcanism and extrusion of andesite, rhyolitic, and dacite flows, SCI formed a subaerial plateau over time (Olmsted, 1958; Lamar et al., 1968; Merifield et al., 1971). Potassium-Ar ages from a drill core at Eel Point (Figure 2.4) collected at depths of 12 m and 353 m yielded respective ages of 15.7+/-0.8Ma and 15.5+/-0.7Ma, indicating a rapid effusive process lasting less than 1My (Lamar et al., 1968; Merifield et al., 1971). Middle to Upper Miocene marine sediments are observed intercalated with the youngest volcanics cored on SCI, confirming the Middle Miocene K-Ar dates coincide with the end of volcanism (Olmsted, 1958). Lapilli tuff observed mantling the islands volcanics suggest SCI was subaerially exposed during the Middle Miocene, and the overlying volcanic sands record the period of erosion and sediment transport (Vedder and Moore, 1976). Marine shales mantle the volcanics and related deposits of SCI (Olmsted, 1958), signifying an increase in RSL towards the Late Miocene.

Megafossils identified by Vedder and Moore (1976) at the Lemon Tank Reservoir Zone (+335m; location shown in Figure 2.4) and the NOTS Pier (+23m; location shown in Figure 2.4) are key Neogene paleoenvironmental indicators for the tectonic history of SCI. Middle to Late Miocene fossils found at the Lemon Tank site suggests a shallow depositional environment (< 75 mbsl) existed at this time. Overlying Pliocene megafossils recovered at the same locations reveal a slightly deeper sublittoral environment (< 150 mbsl). The agreement between the macrofossil and geologic records of SCI provides strong evidence that SCI experienced inundation due to rising RSL during the latter part of the Miocene (Vedder and Moore, 1976). The paleoenvironmental observations of Vedder and Moore (1976), together with those of Olmsted (1958), suggest that following the subaerial Middle Miocene exposure of SCI's volcanic core, SCI experienced an episode of subsidence in the Late Miocene. Similar macrofossil assemblages that record Miocene subsidence are also observed on CI (Vedder et al., 1979; Vedder and Howell, 1980). Based on sediment facies and shell fragments of unknown age, Smith (1933) proposed a location on CI presently at an elevation of ~475 m was submerged in the Pleistocene to water depths up to ~425 mbsl. Although there is some uncertainty concerning the ages of the shell fragment reported by Smith (1933), the paleo sea-level record of CI is consistent with observations from SCI.

### 2.3.3 Emergent Terraces

To date, the most extensive survey of emergent marine terraces on SCI was conducted by Adler (2003), research that built upon the work of Muhs & Szabo (1982). Muhs & Szabo (1982) used absolute dating methods (U-Th) to date the lowest two terraces at Eel point (Figure 2.4) with present elevations of 5m and 32m to 60ka and 107ka, respectively, yielding the first uplift rates for SCI (0.2m/ky - Muhs and Szabo, 1982; Muhs, 1983). Adler (2003) identified the same terraces observed by Muhs & Szabo (1982) on both the western and eastern sides of the island as being the interglacial terraces corresponding to MIS 5a and 5e (80ka and 120ka; Figure 2.3). Furthermore, these two emergent terraces are observed at comparable elevations around the perimeter of SCI, signifying that SCI has experienced uniform uplift post-MIS 5e, lowering the previously calculated uplift rate to 0.135m/ky. Additionally, Adler (2003) mapped 31 discrete emergent marine terraces onshore SCI, and as a suite, they were found to strongly correlate to the interglacial high stands of the Pliocene through Quaternary providing a robust uplift signal for SCI 3-4Ma to present (see Supplementary Figure S1).

Identified interglacial terraces within San Diego County (SDC) (Kern and Rockwell, 1992b; Muhs, 2002; Haaker et al., 2016, S1) are found at comparable elevations to the terraces on SCI (Adler, 2003), with similar uplift rates of 0.13m/ky and 0.135m/ky, respectively. Rift-flank uplift from the opening of the Salton Trough can explain the uniform Quaternary uplift observed along the SDC coast (Kern and Rockwell, 1992b; Muhs, 2002; Mueller et al., 2009; Haaker et al., 2016). However, it does not explain the flight of terraces observed on SCI (~115 km offshore)(Muhs, 1983; Adler, 2003) or analogous marine terraces observed within the NCI (Muhs et al., 2014). According to the crustal flexural models of Mueller et al. (2009), uplift diminishes to zero before reaching SCI, which suggests a process other than flexure drives the observed regional uplift.

CI stands out as an anomaly within the regional uplift signal, the defined marine terraces observed throughout the ICB appear to be absent from CI (Schumann et al., 2012). Some have attributed the absence of these morphologic features as evidence that CI is subsiding (Castillo et al., 2019), which places Quaternary age predictions on the marine terraces observed around CI. However, the stream profiles from the ephemeral drainages that dissect the island (Schumann et al., 2012) do not support this interpretation. If CI is undergoing subsidence as predicted by Castillo et al. (2019), marine and estuarian sediments will backstep landward as RSL rises, infilling the new accommodation (Christie-Blick and Driscoll, 1995). In contrast, what is observed is that the lower reaches of the drainage systems on CI are steep-walled, deeply incised, event-dominated drainages with a morphology more characteristic of a falling limb than a rising limb of RSL (Schumann et al., 2012). Others attribute the lack of preserved subaerial marine terraces to landscape rejuvenation from rapid uplift, removing almost all evidence of subaerial terraces onboard CI (Schumann et al., 2012) and poor terrace preservation in schists (Figueiredo et al., 2013).

Until recently, there have only been a few disputable marine terraces identified on CI (Smith, 1933; Vedder et al., 1979; Vedder and Howell, 1980), which has led to decades-long disputes regarding the RSL history of CI. However, recent field observations within the Little Harbor area of CI have identified three separate marine terraces capped with Pholad-bored cobbles and Miocene-Pliocene marine sediments (McInnis and Pinter, 2021). The Pholad-bored cobbles and Miocene-Pliocene marine sediments strongly support that subaerial marine terraces exist on CI and, possibly more importantly, the marine terraces identified by McInnis and Pinter (2021) predate the Quaternary. This strong constraint needs to be honored when discussing the RSL history of CI.

### 2.3.4 Faulting on San Clemente Island

Further examination of the core at Eel Point (Figure 2.4) shows dipping flat bottom vesicles within the andesite, dacite, and rhyolite flows (Lamar et al., 1968; Merifield et al., 1971). The presence of dipping flat bottom vesicles (21°- 31°) throughout the core suggests that SCI may have experienced a "folding/faulting" event during its effusive growth, possibly imparting the island's marked asymmetry. Faulting onshore SCI mostly trends N 30° E, indicating an oblique component along the San Clemente Fault (SCF) (Olmsted, 1958; Merifield et al., 1971; Adler, 2003). SCI's faulting does not appear to offset the subaerial terraces on SCI, suggesting any trans-island faulting predates the Quaternary (Adler, 2003).

Offshore MCS data collected by Bohannon and Geist (1998), Maier et al.( 2018), Francis et al. (2019), and Walton et al.(2020) show that the stratigraphic deformation or divergence that would accompany 400m of Quaternary subsidence (Castillo et al., 2019) within the Catalina Basin and or in the San Pedro Basin does not exist (Figure 2.5). Furthermore, the stratigraphy dips slightly away from the CF, which is not consistent with the localized subsidence of CI (Figure 2.5).

### 2.3.5 Submerged Terraces

The outboard shelves off SCI and CI are prominent features observed in the bathymetry data (Figures 2.4, 2.6 & 2.7; NOAA, 2003). In Chapter 1, we highlight the usefulness of bathymetry data but caution its use alone to identify submarine terraces, as there is a potential to introduce artifacts in the data that resemble wave-cut platforms known as "terracing" (Smith and Sandwell, 2004). Therefore, we strongly suggest that any submarine terrace observed in bathymetry data needs to be vetted with other data sets.

The shelf encircling SCI has been interpreted (Castillo et al., 2019) as being one single marine terrace. With depths ≤125 mbsl, the shelf depth is consistent with LGM (~22ka) and younger events when using global eustatic LGM models (~120 mbsl, Peltier and Fairbanks, 2006) or the LM2 model of Muhs et al. (2012). However, these RSL models place the MIS 5.5 and MIS 5.3 terraces at depths of ~20 mbsl for their respective interglacials. This means that these models do not accurately predict the dated emergent marine terraces observed throughout the ICB, an inconsistency that cannot be overlooked. Therefore, we use the local paleo sea-level model (LM1) predicted by Muhs et al. (2012), which places LGM at 95 mbsl for the ICB, ~25m shallower than that of the deeper paleo sea-level models (e.g., ~120 mbsl, Peltier and Fairbanks, 2006). This change in LGM depth for the CCB suggests the large shelf encircling SCI is not one single terrace incised by an LGM occupation, as previously interpreted (Castillo et al., 2019).

Castillo et al. (2019) imaged several sequences along the broad shelf encircling CI and attributed these subsurface reflectors to RSL changes of the late Quaternary. They employed parameters identified by Patruno et al. (2015) to differentiate between subaerial and submarine delta clinoforms. Their interpretation suggests CI is experiencing Quaternary subsidence (0.08-0.27m/ky), in stark contrast with the regional uplift signal observed throughout the ICB. Based on their analysis (Castillo et al., 2019; Figure 4B & 4D), the LGM transgressive surface is mantled by oblique prograding clinoforms. Such an interpretation of the LGM transgressive surface is not consistent with the facies architecture that accompanies an increase in base level (Posamentier et al., 1992; Driscoll and Karner, 1999; Catuneanu, 2006) or with observations from other margins within the ICB. For example, offshore San Onofre the LGM transgressive surface separates dipping and truncated sediments below from flat-lying marine deposits above (Hogarth et al., 2012; Klotsko et al., 2015). Farther south, offshore La Jolla, similar stratal geometries are observed above and below the transgressive surface (Hogarth et al., 2007; Le Dantec et al., 2010). During the LGM transgression, accommodation increases, and associated facies backstep landward; the new accommodation allows overlying regional deposits to mantle the dipping and truncated deposits. There are no clinoform topsets (i.e., sigmoidal clinoforms) observed in Figures 4B & 4D of Castillo et al. (2019); the clinoforms are all oblique with no aggradation. This striatal pattern is difficult to explain during a transgression with increased accommodation (Christie-Blick and Driscoll, 1995).

## 2.4.0 Methods

During the summer of 2015, Compressed High-Intensity Radar Pulse (CHIRP) data were collected off SCI, onboard the R/V Point Loma using an EdgeTech 512 sub-bottom profiler towed at ~1m below the surface. An acoustic source with a swept frequency of 1-15kHz was used with a pulse length of 50ms. Real-time GPS navigation data were collected for each acoustic shot. Navigation and shot data were converted into JSF file format using the R/V Point Loma's onboard computer. JSF files were later converted into SGY file format and de-heaved and post-processed using SIOSEIS (Henkart, 2003). The seismic interpretation was performed using IHS Kingdom suite. In winter 2018, seismic data also were collected along the broad southern tip of CI, using the R/V Sally Ride's hull-mounted Knudson 3.5khz echosounder. SGY files were enveloped and processed using SIOSEIS (Henkart, 2003) and interpreted using IHS Kingdom suite. All conversions between the Two-Way Travel Time (TWTT) (seconds) and depths (mbsl) were calculated using nominal velocities of 1500 m/s.

A recording window error was recorded in lines SCI2015D01L13000, SCI2015D01L14000, and SCI2015D01L15000. This recording error biased the resultant profiles, as the upper 0.04 seconds were not recorded. Figures derived from these lines were depth corrected using the relationship between the sediment-water interface and the true multiple recorded in the SGY files.

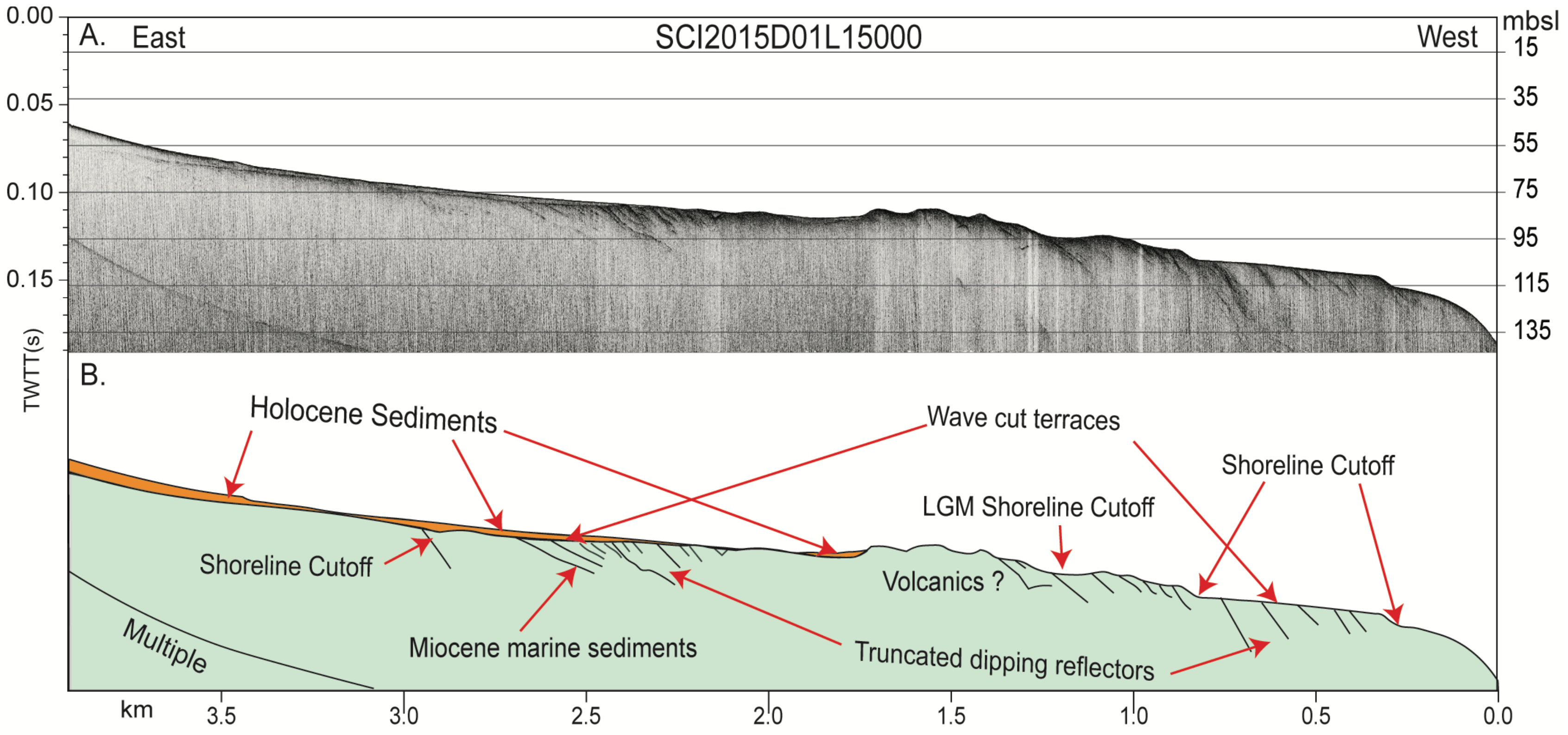

Figure 2.8 A. Uninterpreted CHIRP dip line SCI2015D01L15000.

B. Interpreted CHIRP dip line SCI2015D01L15000. Depths for all seismic profiles were calculated using a nominal water velocity of 1500m/s. The location of the profile is shown in Figures 2.4 and S3.

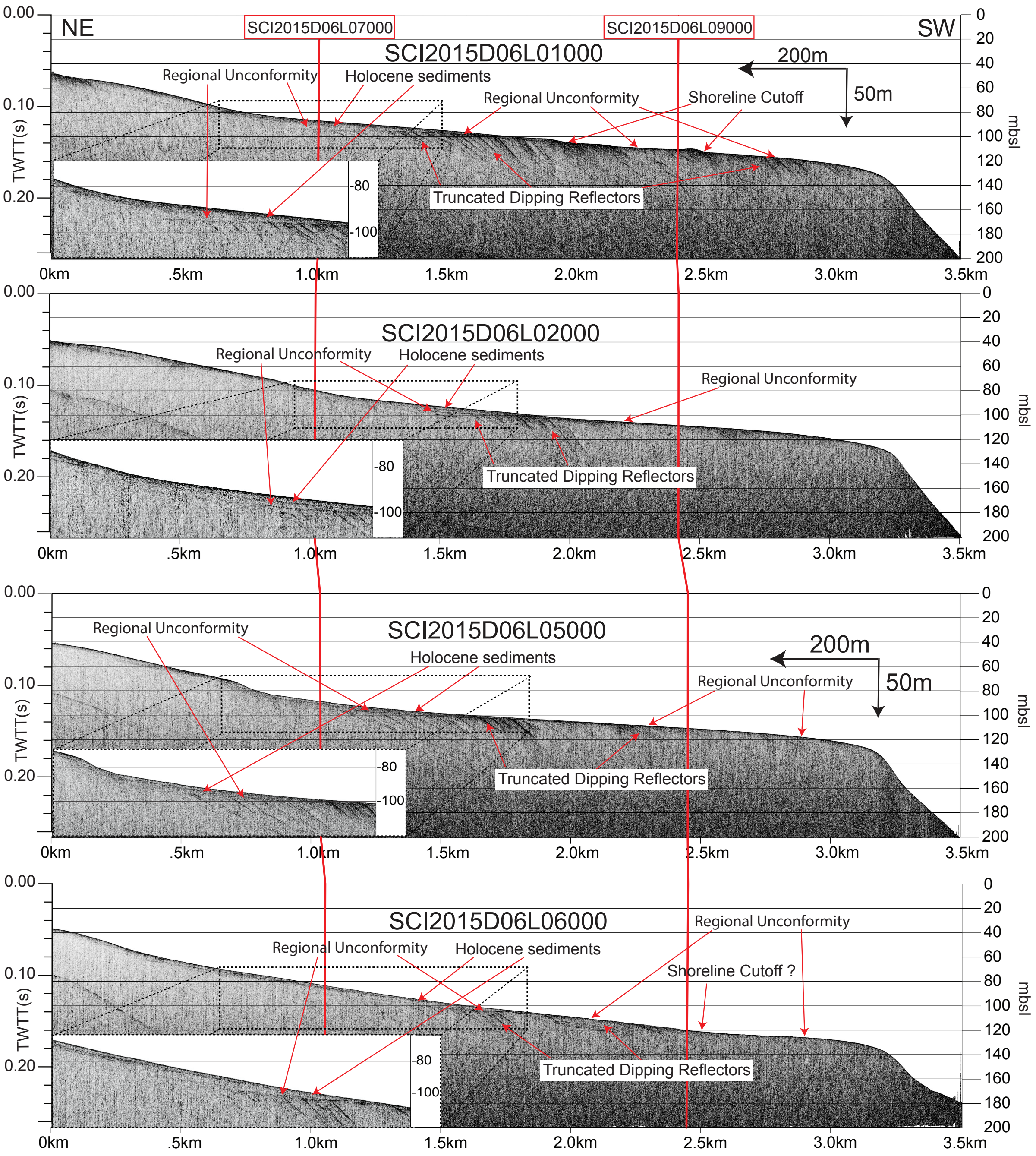

Figure 2.9 Dip lines across the western shelf of SCI.

Red lines indicate strike line crossings (Figure 2.10). Dipping and truncated reflectors beneath the interpreted regional unconformity are imaged. The relationship between the erosive surface and the thin units of the younger sediments is highlighted within the dip profile inset(s). The locations of profiles are shown in Figures 2.4 and S3.

Figure 2.10 Strike Lines from survey group 2.

Red lines show the location of dip line crossings. Numerous dipping, truncated reflectors beneath the regional unconformity are imaged. One identifiable feature in profile line SCI2015D06L09000 is a potential paleochannel; no-fault offset is observed. The locations of profiles are shown in Figures 2.4 and S3.

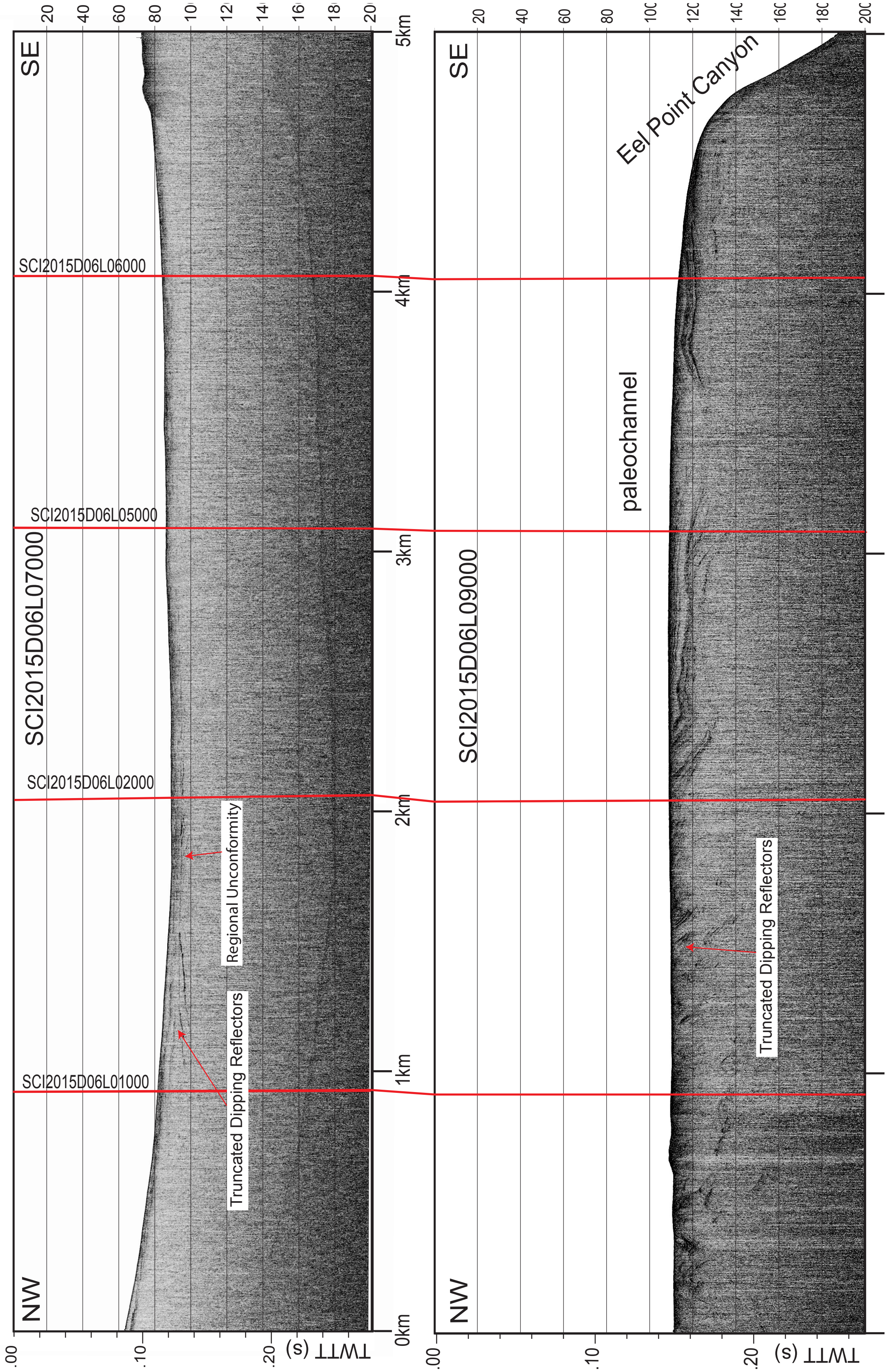
NW
SE
SCI2015D06L07000
SCI2015D06L01000
SCI2015D06L02000
SCI2015D06L05000
SCI2015D06L06000
Truncated Dipping Reflectors
Regional Unconformity
0km
1km
2km
3km
4km
5km
.00
.10
.20
TWTT (s)
20
40
60
80
10
12
14
16
18
20
NW
SE
SCI2015D06L09000
paleochannel
Eel Point Canyon
Truncated Dipping Reflectors
0km
1km
2km
3km
4km
5km
.00
.10
.20
TWTT (s)
20
40
60
80
100
120
140
160
180
200

## 2.5.0 Results

### 2.5.1 Regional Unconformity

Dip lines collected offshore of SCI image a seaward dipping truncated section that in some places is overlain by a thin acoustically transparent package that slightly thickens landward (Figure 2.8, 2.9, 2.10, 2.11, & S4). High-amplitude reflectors mark the truncated seaward dipping unit. The upper boundary of these truncated seaward dipping reflectors is the most prominent reflector within the survey area and is referred to as the regional unconformity. The regional unconformity is well preserved with minimal overprinting by tectonic folding or faulting. The regional unconformity exhibits a series of steps or terraces separated by an increase in slope. These changes in slope are characteristic of the observed onshore terraces of SCI (Figure 2.2). We will refer to the base of the increase in slope as the shoreline cutoff and associated flat eroded surface as a terrace, which is consistent with the nomenclature used by other researchers (Kern and Rockwell, 1992; Adler, 2003; Haaker et al., 2016).

### 2.5.2 Western shelf

Erosional surfaces along the western flank are distinct morphological features in the high-resolution CHIRP data. CHIRP line SCI2015D01L015000 (Figure 2.8) images at least three marine terraces; the deepest shoreline cutoff is at 115 mbsl and is accompanied by a narrow terrace. The most prominent marine terrace is observed from 102 mbsl to 110 mbsl and is just outboard of a very narrow erosive surface at 95 mbsl that abuts what are possibly more erosive resistant volcanic rocks. The more erosive resistant section separates the deeper erosional surfaces from shallower marine scouring events at 75mbsl to 85 mbsl and 70mbsl, where it shallows to an unknown depth. The shallower eroded surfaces are overlain by thin, draping sedimentary units, while the deeper scoured surfaces are sediment starved.

Dip profiles across the western shelf of SCI also image multiple erosional events within the broad western shelf (Figure 2.9). When precise shoreline cutoffs are not clearly imaged, individual terraces are challenging to identify. The relationship between young sediment units and the regional unconformity suggests at least two, possibly three, discreet erosional events are evident in the dip profiles collected along the western shelf of SCI, inboard of the shelf edge at ~125 mbsl. CHIRP profile SCI2015D06L07000 images a thin layer of young draping sediments

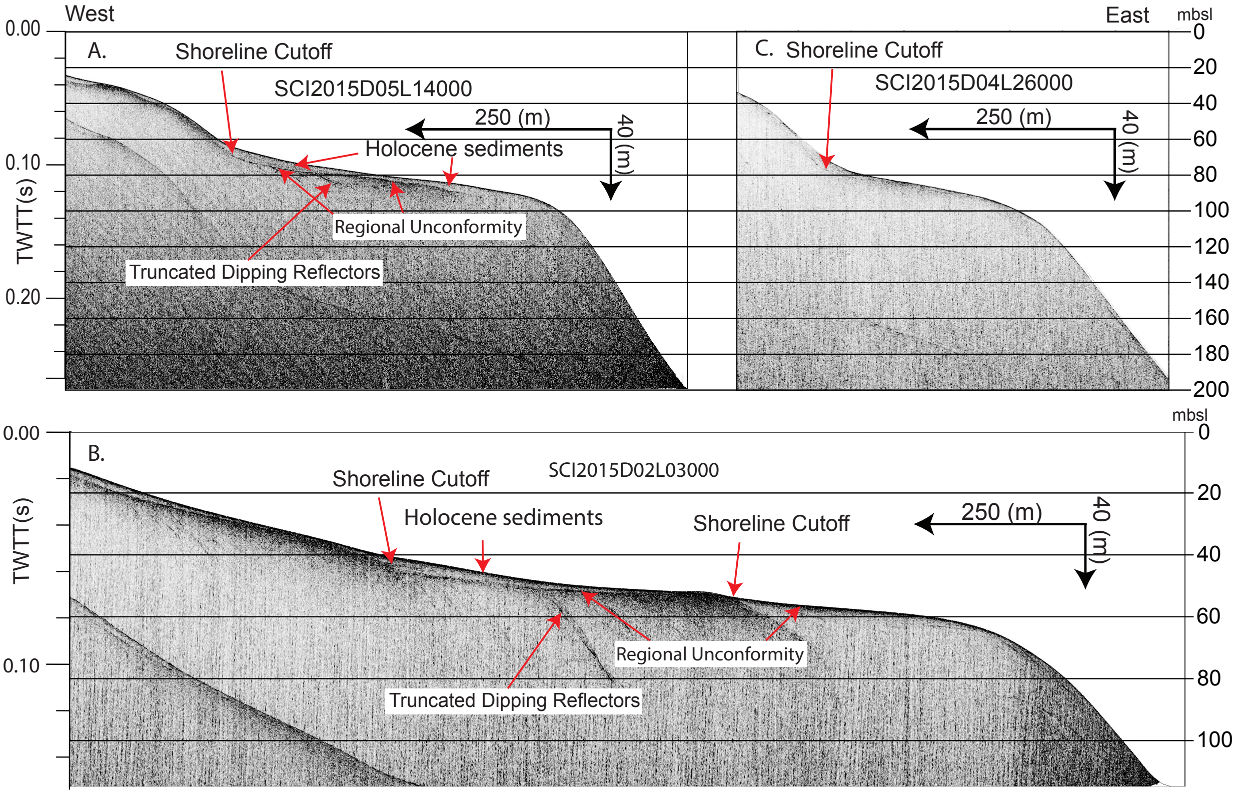

Figure 2.11 Erosion events are recorded within the morphology of the eastern shelf.

Insets A & C both show a shoreline cutoff at -75mbsl, mantled by younger sediments. Profile B is located at NOTS pier and has two shoreline cutoff offs at -45mbsl and -55mbsl. No active faulting is observed to explain the shallower erosive surfaces in B from those observed in A & C. The locations of profiles are shown in Figure 2.4.

above the regional conformity to the NW; no younger sediment packages are observed above the regional unconformity just inboard of the shelf edge along strike profile SCI2015D06L09000 (Figure 2.10). CHIRP profile SCI2015D06L09000 does image a potential channel that appears to predate the earliest erosional event, just north of the canyon off Eel Point.

### 2.5.3 Eastern Shelf

Characteristics that define erosion on the western shelf also are observed in profiles around Wilson Cove and NOTS Pier, where the shelf is at its widest on the leeward side (Figure 2.11). The seaward dipping reflectors are truncated at these localities and covered by thin layers of younger sediments, similar to the inboard scoured surface observed along the western shelf.

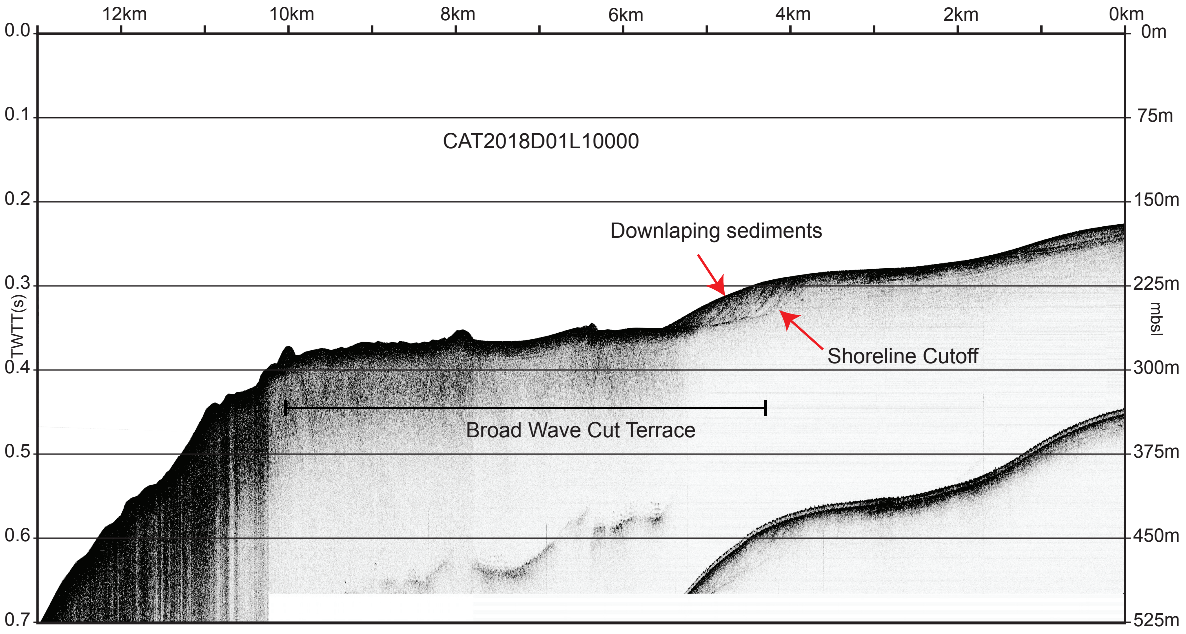

Figure 2.12 Dip line collected onboard the R/V Sally Ride.

Using a hull-mounted Knudson 3.5khz CHIRP echosounder, shows a distinct marine cut terrace. The Shoreline cutoff of this marine terrace is observed at (-255m), and a prograding sediment package downlaps onto the marine terrace.

The shelf edge on the leeward side of SCI occurs at depths of ~ 95m along the entire trace of the San Clemente Fault, except for the NOTS Pier area, where the shelf edge depth is ~ 65 mbsl. With the noted exception of the NOTS pier area, there appears to be a marine terrace with a shoreline cutoff of ~ 73 mbsl within the broader parts of SCI's eastern shelf. At the NOTS pier area, where the eastern shelf edge is shallow, at least one, possibly two, marine terraces with shoreline cutoffs at 55 mbsl and 45 mbsl respectably (Figure 2.11). Faulting to account for the anomalously shallow shelf edge and terraces within the NOTS pier area are not observed. Unfortunately, most of the eastern shelf is narrow with few sub-bottom reflectors imaged in the CHIRP data; the sediment-water interface and the shelf edge are the most discernible features along the eastern side of SCI and the adjoining San Clemente Fault scarp (Figure 2.11).

### 2.5.4 Deeper terraces of Santa Catalina Island

A well-defined submarine terrace is observed on the southeastern margin of CI at ~250 mbsl (Figure 2.12). The shoreline cutoff of this 5km wide terrace is observed at ~225 mbsl and has been covered by a pronounced progradational package that down laps onto the submarine terrace. The topsets of this oblique prograding clinoform are not observed in the data.

## 2.6.0 Discussion

### 2.6.1 Submarine Terraces of Santa Catalina Island

Submarine terraces below LGM sea levels are observed offshore CI (Figures 2.7 & 2.12) and have been interpreted to be formed during Quaternary glacial still stands (Castillo et al., 2019). Seismic profiles collected offshore CI images a well-defined marine terrace at 250 mbsl (Figure 2.12). Schumann et al. (2012) noted this submarine terrace offshore CI, but because of the potential for this feature to be an artifact of data processing, they could not identify it as a submarine terrace confidently. Based on the data presented herein (Figures 2.4, 2.6, 2.7, 2.8, 2.9, 2.12, and S4), the flat-lying morphologic features observed below the regional LGM sea level around CI and SCI are interpreted as marine terraces of varying depths.

The shoreline cutoff (225 mbsl) for the deep terrace offshore CI is overlain by a downlapping, oblique prograding sediment package (Figure 2.12). The facies architecture of this oblique progradational package likely records a time when the accommodation was not increasing rapidly, possibly just following a base-level low. Topsets of this oblique progradational package are not observed in the data, suggesting either there was minimal aggradation accompanying this deposition or the topsets have been scoured away by a subsequent erosional event. A future scientific campaign tasked with dating the fossil assemblages within this low stand wedge has the potential to constrain the age of these deep submarine terraces.

### 2.6.2 Marine Terraces on and around San Clemente Island

The exposed subaerial marine terraces on San Clemente Island, the Southern California Coast, as well as the Northern Channel Islands have been dated and correlate to the interglacial high stands of the Quaternary, yielding a regional uplift signal (0.13m/ky - 0.2m/ky) for the California Borderland (Muhs and Szabo, 1982; Kern and Rockwell, 1992b; Muhs et al., 1992, 2014; Muhs, 2002; Adler, 2003; Haaker et al., 2016).

Multiple submarine terraces have been imaged within the broad shelf along the western margin of SCI. Terraces and their associated features are imaged at consistent depths of 95 mbsl, 102 mbsl to 110 mbsl, and 115 mbsl throughout multiple dip profiles along the western margin of SCI. Based on the regional RSL history (Muhs et al., 2012), the submarine terraces imaged at 95 mbsl are consistent with an LGM occupation (Figure 2.8, 2.9, & S4). However, given the recorded uplift of SCI, terraces deeper than LGM observed at 102 mbsl to 110 mbsl and 115 mbsl are inconstant with LGM and earlier glacial stillstands of the Quaternary.

Younger Dryas (~12ka) marine terraces (55-70 mbsl) are observed along the Southern California Coast with a shoreline cutoff at ~55 mbsl (Klotsko et al., 2015; Hogarth et al., 2012). The two shallower scouring events imaged inboard of the LGM terrace on the western shelf of SCI (Figure 2.8) were observed at 75 mbsl to 85 mbsl and 70 mbsl (which shoals landward). The latter may be related to Younger Dryas; however, the former is not.

The eastern shelf of SCI (Figure 2.11), with the exception of the NOTS pier area, has a consistent marine terrace with a shoreline cutoff at ~73 mbsl inboard of the shelf edge of ~95 mbsl. This ~73mbsl shoreline cutoff is consistent with the depth of the 75-85 mbsl terrace observed on the western shelf. In addition, the NOTS pier has two shallower marine terraces at 55 mbsl and 45 mbsl, respectively.

Eight discrete erosional events within the broad shelf encircling SCI were imaged between 115mbsl and 45mbsl. Based on regional RSL (Muhs et al., 2012), scoured surfaces 95mbsl and shallower would have been exposed to wave-based erosion throughout the later part of the Quaternary. Terraces and terrace features observed offshore SCI below 95mbsl, at 102mbsl, 110mbsl, and 115mbsl do not correlate to still stands of the Quaternary.

Based on the deeper pre-Quaternary terraces offshore SCI and the deeper terrace offshore CI, we propose a new model for the formation of the marine terraces within the ICB. Our conceptual model suggests that the observed submarine and subaerial terraces most likely represent terraces initially scoured in the Middle to Late Miocene when shelves and slopes around San Clemente Island and Santa Catalina Island were subjected to wave-based erosion (Figure 2.13).

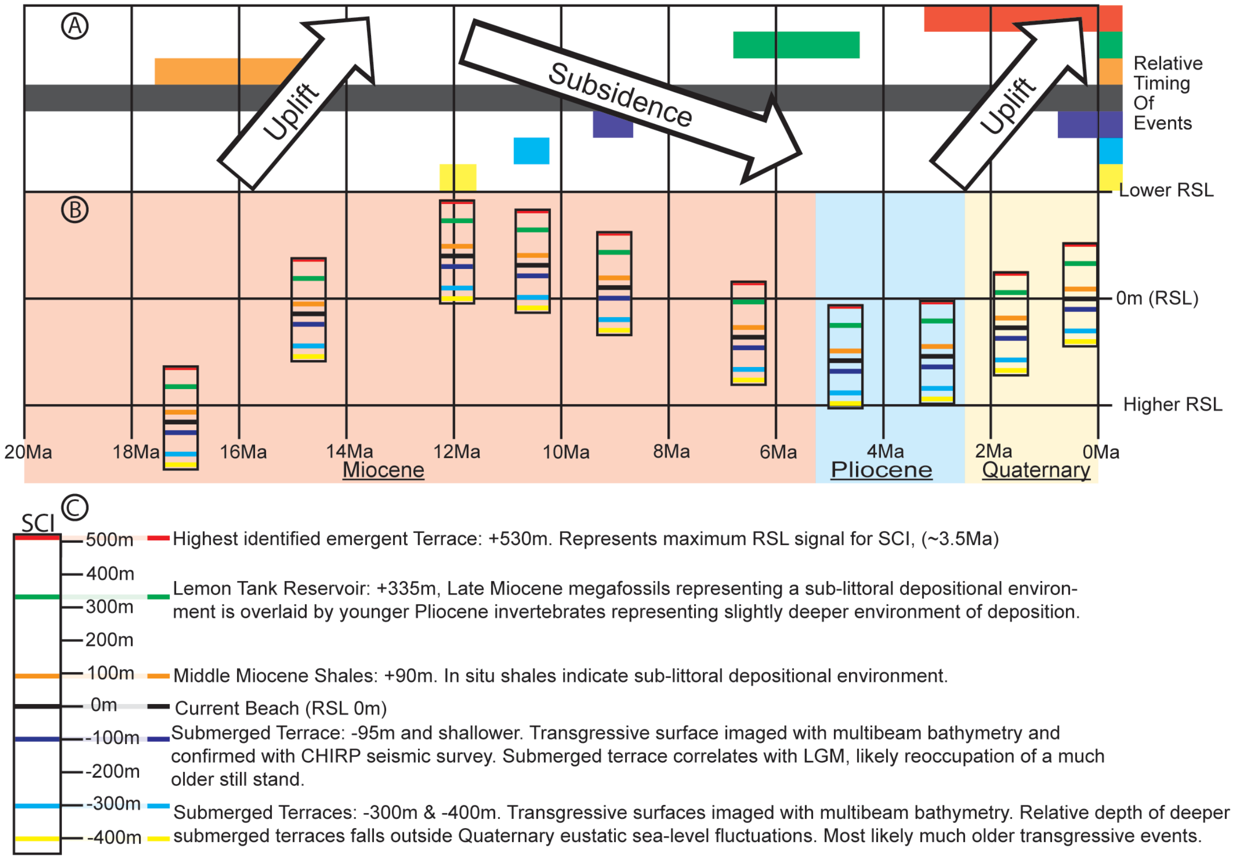

Figure 2.13 Kinematic model of SCI's uplift signals as a function of time.

Inset A. represents the relative timing of evidence for SCI (see section C. for the color-coded explanation.) Inset B. represents the 15My of RSL change for SCI. Finally, inset C. represents the in-situ color-coded placement for critical lines of evidence for the RSL history of SCI.

### 2.6.3 Paleo-reconstruction

We present the following new conceptual model for ICB Neogene and Quaternary marine terrace formation (Figure 2.13):

1. San Clemente Island was formed during a rapid effusive volcanic process, possibly induced by dilation along the San Clemente Fault, which engendered decompression melting (Olmsted, 1958; Merfield, 1971). SCI's formation and CI's exhumation (Grove et al., 2008) coincide with large-scale regional volcanism and extension of the ICB. Following the volcanism, the CCB transitioned to a transform margin with predominantly dextral deformation still active today. Middle Miocene shales (16.5-15.5 Ma) of the Monterey Group are subaerially exposed on CI (Olmsted, 1958; Smith, 1960; Vedder and Moore, 1976; Grove et al., 2008; Schumann et al., 2012) and are interbedded within the volcanics that comprise more than 95% of SCI (Olmsted, 1958). These observations indicate that the prevalent Middle to Late Miocene depositional environment was marine for both SCI and CI and concurrent with volcanism (Figure 2.13).
2. With no noticeable post-Middle Miocene divergence or deformation along the SCF and the CF bounding the Catalina Basin (Figure 2.6), any regional tectonic deformation and or RSL fluctuations would likely affect SCI and CI similarly.
3. Observed lapilli tuff and volcanic sands intercalated within the shale and claystone atop the Middle Miocene volcanics of SCI (Merifield et al., 1971; Vedder and Moore, 1976) and CI (Vedder et al., 1979) indicate that shortly after the islands formed, they experienced an episode of subaerial erosion. The calcium carbonate concentration increases as a function of depth within the autochthonous sediments suggesting an increase in RSL following the episode of erosion (Ward and Valensise, 1996).

4. Marine terraces identified below LGM sea level predate the Quaternary using fiducial markers identified on SCI and CI. If correct, in this scenario, submarine marine terraces identified below 95 mbsl could record initial Middle to Late Miocene occupations (Figure 2.13). Likewise, this model also suggests Quaternary dated marine terraces shallower than LGM, as well as subaerial terraces could be reoccupations of terraces formed in the Middle to Late Miocene. For example, abrasion platforms observed in seismic profiles that correlate with Quaternary occupations offshore SCI (Figures 2.8, 2.9, 2.10 & 2.11) were possibly scoured in the Middle Miocene to Late Pliocene (Figure 2.13).
5. Megafossils found on SCI at the Lemon Tank Reservoir Site (+335m) indicate that from Late Miocene to the Pliocene, the environment of deposition transitioned from shallow to deeper water environments of ~150 mbsl (Vedder and Moore, 1976). Recently identified marine terraces on CI capped by Pholad-bored cobbles and Miocene Pliocene marine sediments (McInnis and Pinter, 2021) support this increase in RSL for the CI. Megafossils collected on CI also record this subsidence signal (Vedder et al., 1979); as well as the regional subsidence is observed throughout the ICB at this time.
6. Quaternary uplift signals derived from emergent marine terraces are well constrained and record a regional uplift at ICB, SDC, and NCI (S5). Emergent marine terrace-like features have been speculated to exist on CI (Smith, 1933; Vedder et al., 1979; Schumann et al., 2012), recent observations (McInnis and Pinter, 2021) suggest they do, a valuable constraint when contextualizing the vertical tectonic signals from the ICB.

### 2.6.4 Regional Vertical Tectonic Signals

Before the late Oligocene/Early Miocene, the strain and morphology of the western margin of North America was dominated by Farallon plate subduction. The cessation of subduction ushered in a complex tectonic sequence involving block rotation, extension, and an eventual switch to a transform margin (e.g., Legg, 1991; Crouch and Suppe, 1993; Nicholson et al., 1994; Bohannon and Geist, 1998). The Early to Middle Miocene extension of the ICB (Bohannon and Geist, 1998) engendered the footwall and hanging wall morphology observed throughout much of the ICB. This early stage of deformation also resulted in the rapid thinning and unloading of the ICB lithosphere, which would have resulted in the upwelling of hot and buoyant asthenosphere, which would have resulted in regional uplift (Driscoll and Karner, 1998).

During the second stage of deformation (~15 Ma) estimates of the extensional deformation and an initial crustal thickness (30km) reported by McKenzie (1978) and Weissel and Karner (1989) and Bohannon and Geist (1998) suggest a beta (ß) stretching factor of 1.5 to 2 (Equation 1 & Table 2) (McKenzie,1978; Weissel and Karner,1989), which would have resulted in at least 1km of ICB subsidence (S5). The magnitude of thermal subsidence predicted by the model of McKenzie (1978) and Weissel and Karner (1989) given a stretching factor 1.5 to 2 is 1km to 1.5km, which is consistent with the RSL indicated by the Miocene and Pliocene megafossils found on both SCI and CI (Parsons and Sclater, 1977; McKenzie, 1978; Driscoll and Karner, 1998; Figure S5).

As subduction waned, a transform style margin was initiated. Currently, within the CCB, roughly 10-20 percent (5-8 mm/yr) of the dextral motion between the Pacific and North American plates is being accommodated by offshore strike-slip fault systems (Platt and Becker, 2010; Bennett et al., 1996; Maloney et al., 2016). Understanding how strain is accommodated throughout the CCB region is essential to reconstruct the deformational history and has significant societal relevance, as it is important to assess the potential offshore seismic hazards in Southern California. Until now, our understanding of the vertical strain experienced within the

CCB has been limited to the Quaternary and interpreted to be caused by discrete local lithospheric processes (Ward and Valensise, 1996; Chaytor et al., 2008; Mueller et al., 2009). These lithospheric models cannot explain the Quaternary regional uplift signal observed through the SDC, the ICB, and the NCI (S1). Margin reorganization and a change in plate motion are often invoked to explain this regional uplift, but the age of reorganization predates the uplift signal by ~4 My (Atwater and Stock, 1998).

Another potential explanation for the Late Neogene and Quaternary regional uplift signal observed within the ICB, California Coast, and NCI is dynamic topography supported by a mantle super swell. Mantle super swells have been observed around Hawaii and Bermuda (Detrick et al., 1986; McNutt and Fisher, 1987; McNutt, 1998). In fact, Southern California being dynamically supported by mantle flows is not a new theory. Romanyuk et al. (2007) noted that the lack of evidence for a root supporting the high topography in Bouguer gravity data suggests dynamic mantle support and volcanic rocks along the southern ICB may suggest larger-scale thermal anomalies (Day et al., 2019). A significant volume of research employs or concludes slab-gap or slab-window to explain unexpected tectonic and geochemical signatures observed within the American West (Severinghaus and Atwater, 1990; Humphreys, 1995; Thorkelson, 1996; Murphy et al., 1998; Sonder and Jones, 1999; Liu and Stegman, 2012). These papers agree that slab-gap is a consequence of the cessation of subduction but disagree concerning the geometry of the anomaly. Definitive evidence for slab gap notwithstanding, mantle upwelling would cause a regional topographic response within the ICB and along the Southern California Coast, the magnitude of which would increase with proximity to the center of the super swell. Additional research is required to understand the potential cause for the observed regional Late Neogene and Quaternary uplift across the ICB (Figure 2.13).

## 2.7.0 Conclusions

Marine oxygen isotope records provide a powerful proxy to reconstruct eustatic sea-level fluctuations through time, recording the Earth's cyclic transitions between glacial and interglacial periods of the Late Phanerozoic. The reconstructed eustatic and regional sea-level curves have allowed researchers to use dated emergent marine terraces to constrain coastal uplift and subsidence rates. A suite of 31 subaerial marine terraces has been identified on SCI, which correlate to interglacial high stands of the Quaternary, yielding a robust Pliocene to present uplift signal for SCI (0.135m/ky). Similar uplift signals are observed along with SDC (0.13m/ky) and the NCI (0.12 m/ky - 0.2m/ky).

Newly collected CHIRP seismic profiles nested with USGS MCS profiles and other legacy data of the ICB suggest the Quaternary age constraint is only valid for the suite of emergent marine terraces and should not be ascribed to submerged marine terraces within ICB below local LGM levels 95 mbsl. Without the a priori Quaternary age constraint, a regional tectonic model can explain the depth and history of the marine terraces observed offshore SCI and CI from 15Ma to the present. Geological and geophysical data suggest that shortly after regional volcanism resulted in SCI's effusive volcanic growth, SCI was uplifted and became emergent (Figure 2.13).

Megafossils collected on SCI and CI record the subsequent subsidence of the ICB region as RSL increased towards the end of the Neogene. This period of subsidence correlates to the submarine terraces below LGM levels and possibly the initial scouring of marine terraces that have been reoccupied throughout Quaternary RSL changes. Furthermore, the local Quaternary uplift signatures of SCI (0.135m/ky), SDC (0.13m/ky), and NCI (0.12m/ky-0.2m/ky) appear to record a large ICB regional uplift signal, the cause of which remains unknown.

## 2.8.0 Acknowledgments

We would like to thank the crews of the R/V Point Loma and the R/V Sally Ride for allowing us access to the sea and a safe working environment. We also would like to thank the Navy Base San Clemente Island for access to the nearshore and onshore regions around San Clemente Island and James Color for facilitating all logistical requirements while on Navy Base San Clemente Island. Mackenzie Roberts, James Day, and Hector Perea reviewed previous versions of the manuscript, and their comments are greatly appreciated.

Chapter 2 will be resubmitted for publication in: Derosier, B.J., Driscoll, N.W., In-Prep. Uplift and Subsidence of the Inner California Borderland Constrained by Abrasion Platforms. *Geosphere.* The dissertation author is the primary researcher and author, and the co-author listed in this manuscript directed and supervised this research.

# 2.9.0 Supplemental Material

S 1 Color-coded terrace map (Plate 1).

From Adler (2003), with an explanation of terraces, their respective elevations (meters), ages, and inferred ages for $^1$SCI (Adler, 2003; supplemental Figure S2), $^2$SDC (Kern and Rockwell, 1992b; Haaker et al., 2016), and $^3$NCI (Muhs et al., 2014)

| [1] SCI Terrace (Elevation(m)) | Age (ka)/(MIS) |
|---|---|
| North Head (4-6) | 80 (5a) |
| Light House (21-24) | 120-125 (5e) |
| 3rd (28-33) | 215-225 (7) |
| 4th (46-48) | 319-345 (9) |
| 5th (52) | 385-413 (11) |
| 6th (62) | 459-450 (13) |
| 7th (70) | 518-510 (15) |
| 8th (86) | 615-630 (17) |
| 9th (97) | 719-698 (19) |
| 10th (108) | 800-795 (21) |
| 11th (120) | 889-855 |
| 12th (132) | 978-930 |
| 13th (140) | 1081-975 |
| 14th (169) | 1252-1050 |
| 15th (184) | 1363-1160 |
| 16th (195) | 1444-1290 |
| 17th (204) | 1511 |
| 18th (214) | 1585 |
| 19th (220) | 1629 |
| 20th (230) | 1704 |
| 21st (241) | 1785 |
| 22nd (260) | 1926 |
| 23rd (269) | 1993 |
| 24th (302) | 2237 |
| 25th (320) | 2370 |
| 26th (338) | 2503 |
| 27th (346) | 2563 |
| 28th (380) | 2815 |
| 29th (400) | 2963 |
| 30th (442) | 3275 |
| 31st (530) | 3926 |

| [2] SDC Terrace (Elevation(m)) |
|---|
| Bird R (9-11) |
| Nestor (22-23) |
| Stuart Mesa (32-34) |
| Guy Flemming (46-48) |
| Perry Grove (55) |
| Golf Course (60) |
| San Elijo (68)) |
| Fire Mountian (84) |
| Clairemont (93) |
| Tecolote (106) |
| Linda VIsta (114)) |
| Tierra Santa (124) |
| 13th (130) |
| 14th (140) |
| Rifle Range (155)) |
| Aquaduct (172) |

| [3] NCI Terrace (Elevation(m)) |
|---|
| 1st (7) |
| 2nd (21-24) |

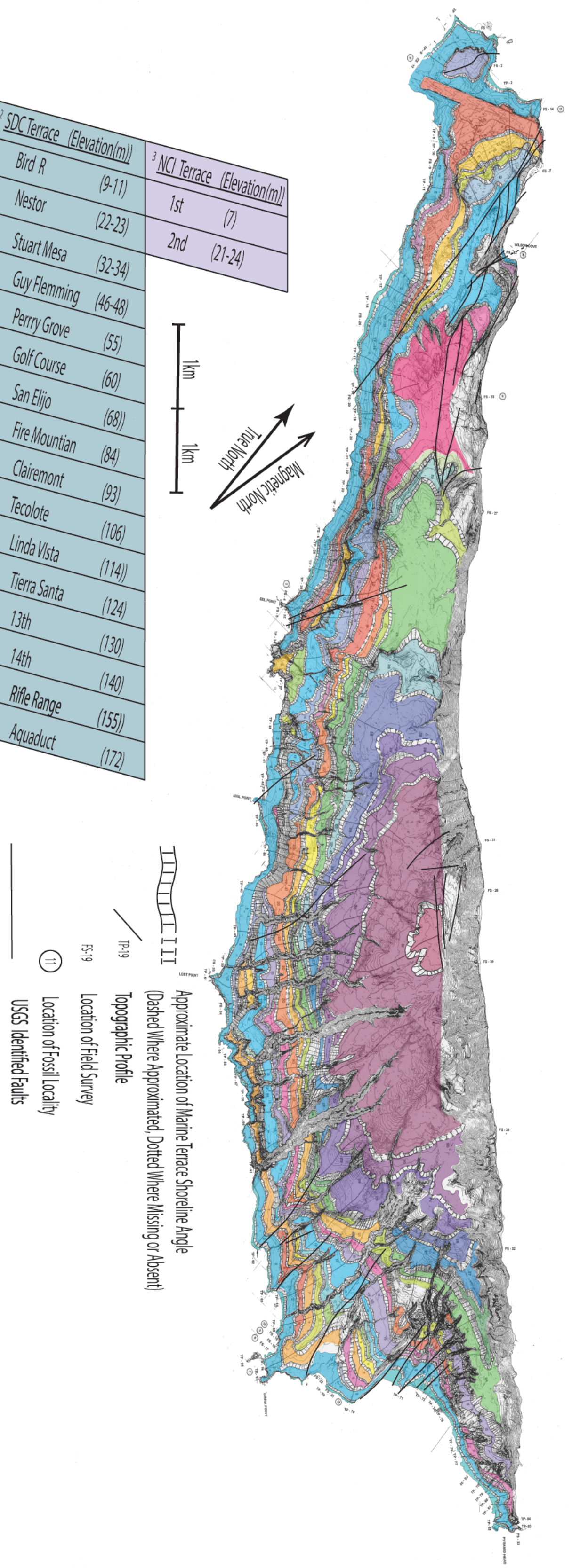

Approximate Location of Marine Terrace Shoreline Angle (Dashed Where Approximated, Dotted Where Missing or Absent)

Topographic Profile

Location of Field Survey

Location of Fossil Locality

USGS Identified Faults

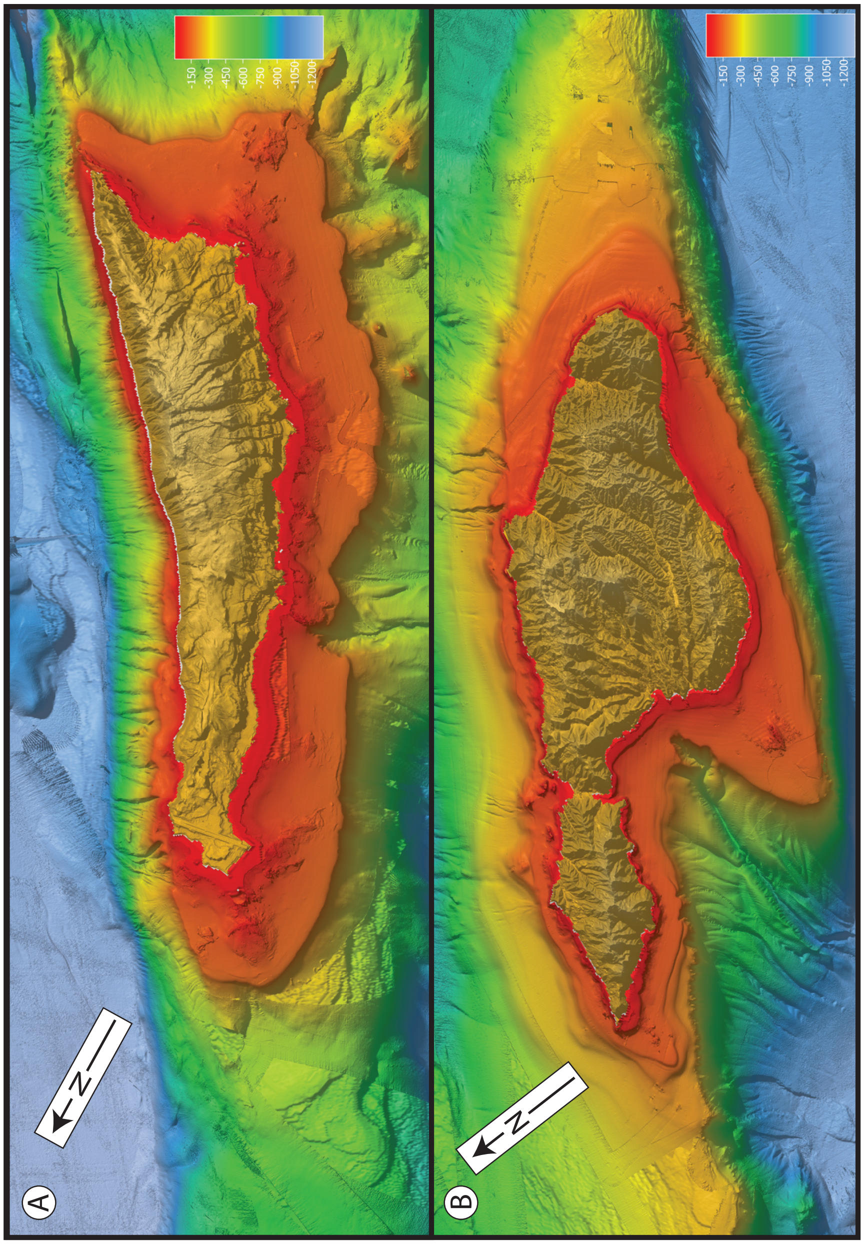

S 2 Topobathymetric map of San Clemente Island and Santa Catalina Island.

Insets A. and B. respectively. Multibeam data collected from numerous cruises (Table S2) were incorporated into a ½ second (15m cell size) bathymetric surface. Underlaying the high resolution multibeam is a 3-second Bathymetric grid provided by NGDC(NOAA- NGDC, 2003). Both bathymetric datasets have a shading azimuth of 90° and a sun angle of 10°, as well as the same color ramp. Topographic data in orange is the Orange County, California 1/3 arc-second Coastal Digital Elevation Model (NOAA-NCEI, 2015), it also is displayed with a shading azimuth of 90° and a sun angle of 10°.

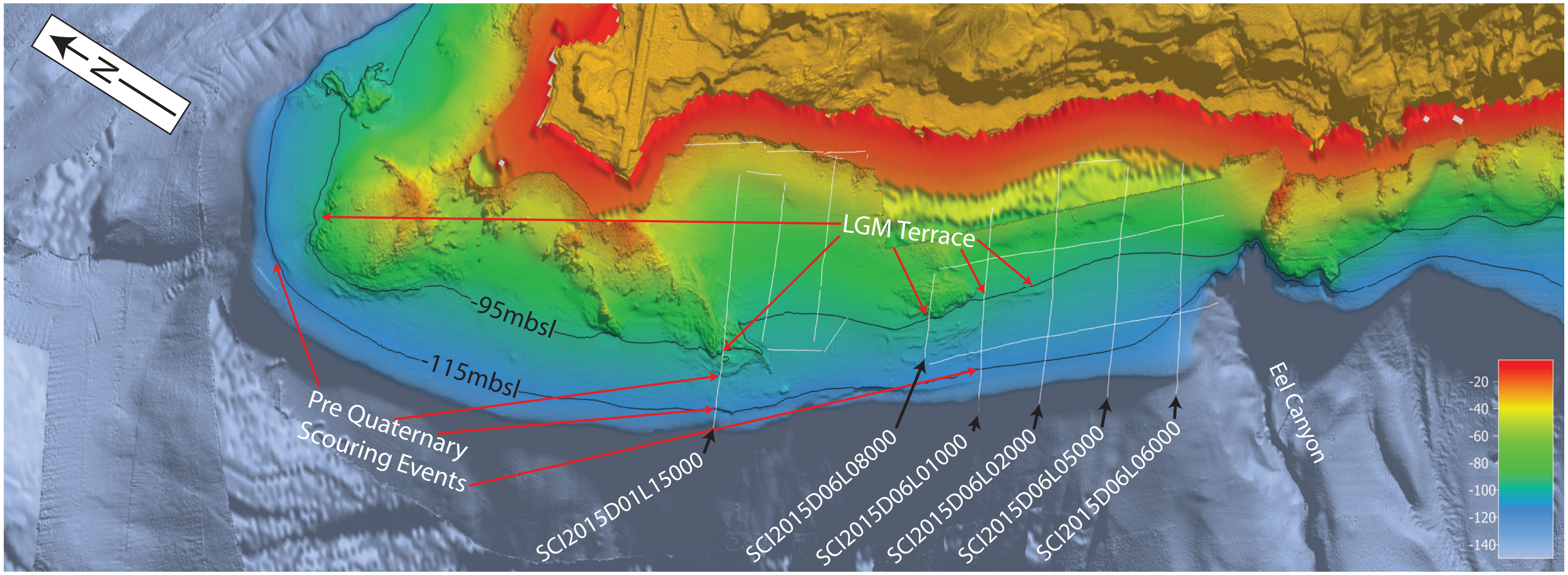

S 3 Topobathymetric map of San Clemente Island.

Data sources explained in S4, White lines represent CHI. RP profiles collected along the western margin of the SCI (See figures, 8, 9, S6). It has been proposed that the broad shelf surrounding SCI is comprised of a single submarine terrace (Francis et al., 2019; Castillo et al., 2019). Not only do the seismic data presented within this paper refutes this claim, the ½ second multibeam data that compliments the subsurface data clearly shows multiple scouring events within the shelf

Table 1 Sources of raw multibeam and topographic data used to create the topobathymetric surfaces shown in figures S2 and S3.

**Table : S2** * denotes unpublished data

| **Cruise** | **Platform** | **Equipment** | **Year** | **source** |
|---|---|---|---|---|
| SKQ201616T | R/V Siquliaq | Kongsberg EM302 | 2016 | NGDC |
| SKQ201607S | R/V Siquliaq | Kongsberg EM302 | 2016 | NGDC |
| SKQ201605S | R/V Siquliaq | Kongsberg EM302 | 2016 | NGDC |
| SKQ201606S | R/V Siquliaq | Kongsberg EM302 | 2016 | NGDC |
| MV1010 | R/V Melville | Kongsberg EM122 | 2010 | NGDC |
| MV1106 | R/V Melville | Kongsberg EM122 | 2011 | NGDC |
| MV1209 | R/V Melville | Kongsberg EM122 | 2012 | NGDC |
| MV1210 | R/V Melville | Kongsberg EM122 | 2012 | NGDC |
| MV1211 | R/V Melville | Kongsberg EM122 | 2012 | NGDC |
| MV1214 | R/V Melville | Kongsberg EM122 | 2012 | NGDC |
| MV1216 | R/V Melville | Kongsberg EM122 | 2012 | NGDC |
| MV1217 | R/V Melville | Kongsberg EM122 | 2012 | NGDC |
| MV1306 | R/V Melville | Kongsberg EM122 | 2013 | NGDC |
| MV1308 | R/V Melville | Kongsberg EM122 | 2013 | NGDC |
| MV1314 | R/V Melville | Kongsberg EM122 | 2013 | NGDC |
| MV1401 | R/V Melville | Kongsberg EM122 | 2014 | NGDC |
| MV1404 | R/V Melville | Kongsberg EM122 | 2014 | NGDC |
| MV1405 | R/V Melville | Kongsberg EM122 | 2014 | NGDC |
| MV1406 | R/V Melville | Kongsberg EM122 | 2014 | NGDC |
| MV1407 | R/V Melville | Kongsberg EM122 | 2014 | NGDC |
| RR1710 | R/V Roger Revelle | Kongsberg EM122 | 2017 | NGDC |
| RR1711 | R/V Roger Revelle | Kongsberg EM122 | 2017 | NGDC |
| RR1719 | R/V Roger Revelle | Kongsberg EM122 | 2017 | NGDC |
| SR1701 | R/V Sally Ride | Kongsberg EM122 | 2017 | NGDC |
| SR1704 | R/V Sally Ride | Kongsberg EM122 | 2017 | NGDC |
| SR1706 | R/V Sally Ride | Kongsberg EM122 | 2017 | NGDC |
| SR1707 | R/V Sally Ride | Kongsberg EM122 | 2017 | NGDC |
| SR1709 | R/V Sally Ride | Kongsberg EM122 | 2017 | NGDC |
| SR1714 | R/V Sally Ride | Kongsberg EM122 | 2017 | NGDC |
| SR1716 | R/V Sally Ride | Kongsberg EM122 | 2017 | NGDC |
| SR1717 | R/V Sally Ride | Kongsberg EM122 | 2017 | NGDC |
| SR1801 | R/V Sally Ride | Kongsberg EM122 | 2018 | R2R |
| SR1802 | R/V Sally Ride | Kongsberg EM122 | 2018 | NGDC |
| SR1815 | R/V Sally Ride | Kongsberg EM122 | 2018 | NGDC |
| SR2001 | R/V Sally Ride | Kongsberg EM122 | 2020 | * |
| TN335 | R/V Thomas G. Thompson | Kongsberg EM302 | 2016 | NGDC |
| TN338 | R/V Thomas G. Thompson | Kongsberg EM302 | 2016 | NGDC |
| TN339 | R/V Thomas G. Thompson | Kongsberg EM302 | 2016 | NGDC |
| FK181005 | R/V Falkor | Kongsberg EM302 | 2016 | NGDC |
| KM1312 | R/V Kilo Moana | Kongsberg EM122 | 2018 | NGDC |
| MCD0212 | R/V Mc Donnell | Simrad EM3000 | 2002 | NGDC |
| EX1101 | NOAA Ship Okeanos Explorer | Simrad EM302 | 2011 | NGDC |
| NA104 | R/V Nautilus | Kongsberg EM302 | 2018 | NGDC |
| NA105 | R/V Nautilus | Kongsberg EM302 | 2019 | NGDC |
| AT26-06 | R/V Atlantis | Kongsberg EM122 | 2013 | NGDC |
| | | | | |
| R2R data acquired at | https://www.rvdata.us/ | | | |
| NGDC data acquired at | https://maps.ngdc.noaa.gov/viewers/bathymetry/ | | | |

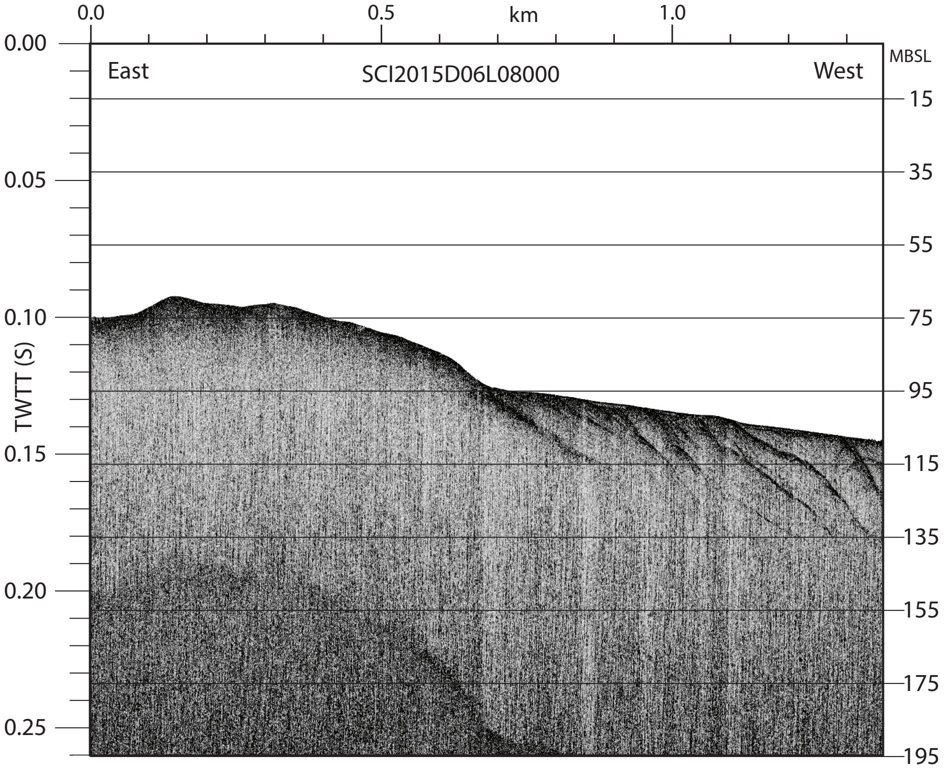

S 4 CHIRP line (SCI2015D06L08000) collected along the western shelf of SCI.

This CHIRP line (see S5 for location), images a clear shoreline cutoff is at 95 mbsl. Outboard this shoreline cutoff, truncated seaward dipping reflectors are observed, characteristic of the regional unconformity. The regional unconformity is observed along this line to at least 110 mbsl.

Equation 1 Initial subsidence model

as a function of extensional stretching (ß) using equation (1) of McKenzie (1978) and parameters from (Parsons and Sclater, 1977; McKenzie, 1978; Table S1).

$$S_i = \frac{a\left[(\rho_o - \rho_c)\frac{t_c}{a}\left(1 - \alpha T_1 \frac{t_c}{\alpha}\right) - \frac{\alpha T_{1\rho_o}}{2}\right]\left(1 - \frac{1}{\beta}\right)}{\rho_o(1 - \alpha T_1) - \rho_w} \text{, equation (1)}$$

Table 2 Parameters used in Equation 1.

From Parsons and Sclater (1977) and Mckenzie (1978)

$S_i$ = Initial subsidence post extension
$a$ = Isostatic continental crustal thickness (125km)
$\rho_0$ = Density of sea water (1.0 g/cm$^3$)
$\rho_c$ = Density of continental crust (2.8 g/cm$^3$)
$\rho_m$ = Density of mantel (3.33 g/cm$^3$)
$\alpha$ = Thermal expansion coefficient of both the mantel and the crust (3.28 X10$^{-5}$ °C$^{-}$
$T_1$ = Temperature of the asthenosphere (1333 °C)
$\beta$ = Stretching factor; $\beta = \frac{b}{a}$ $a$ is the initial width and $b$ is the stretched width.

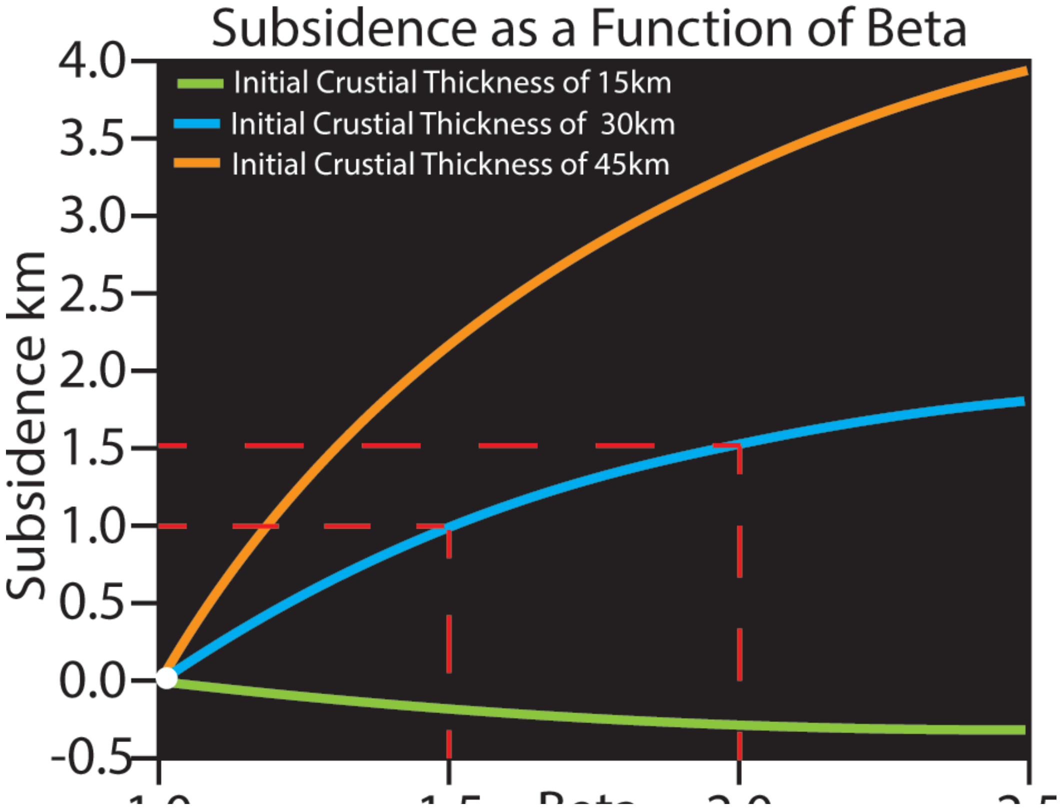

S 5 Subsidence as a Function of Beta.

Model of subsidence as a function of Beta stretching, using the parameters from Table 2 in Equation 1.

# Chapter 3

# Seismic Stratigraphic Analysis of the Catalina Basin; Implications for the Evolution of the Inner California Borderland

## 3.1.0 Abstract

Multi-channel seismic data collected within the Catalina Basin, one of the many basins of the Inner California Borderland, image two basin-wide unconformities. The timing of these two surfaces has implications for the Catalina Basin's tectonic evolution as well as the seismic hazard of Southern California, home to >20 million people. Seismic stratigraphic analysis suggests these two unconformities occurred during the  Early and Middle Miocene and are temporally significant to the tectonic evolution of the Catalina Basin. It is essential to understand the sequence stratigraphic architecture observed within the Catalina Basin as these are important recorders of the tectonic evolution of the Inner California Borderland and the California Borderland as a whole.

## 3.2.0 Introduction

The California Continental Borderland (CCB) (Figure 3.1) records the last ~30 million years (My) of crustal deformation (Atwater, 1970; Nicholson et al., 1994; Bohannon and

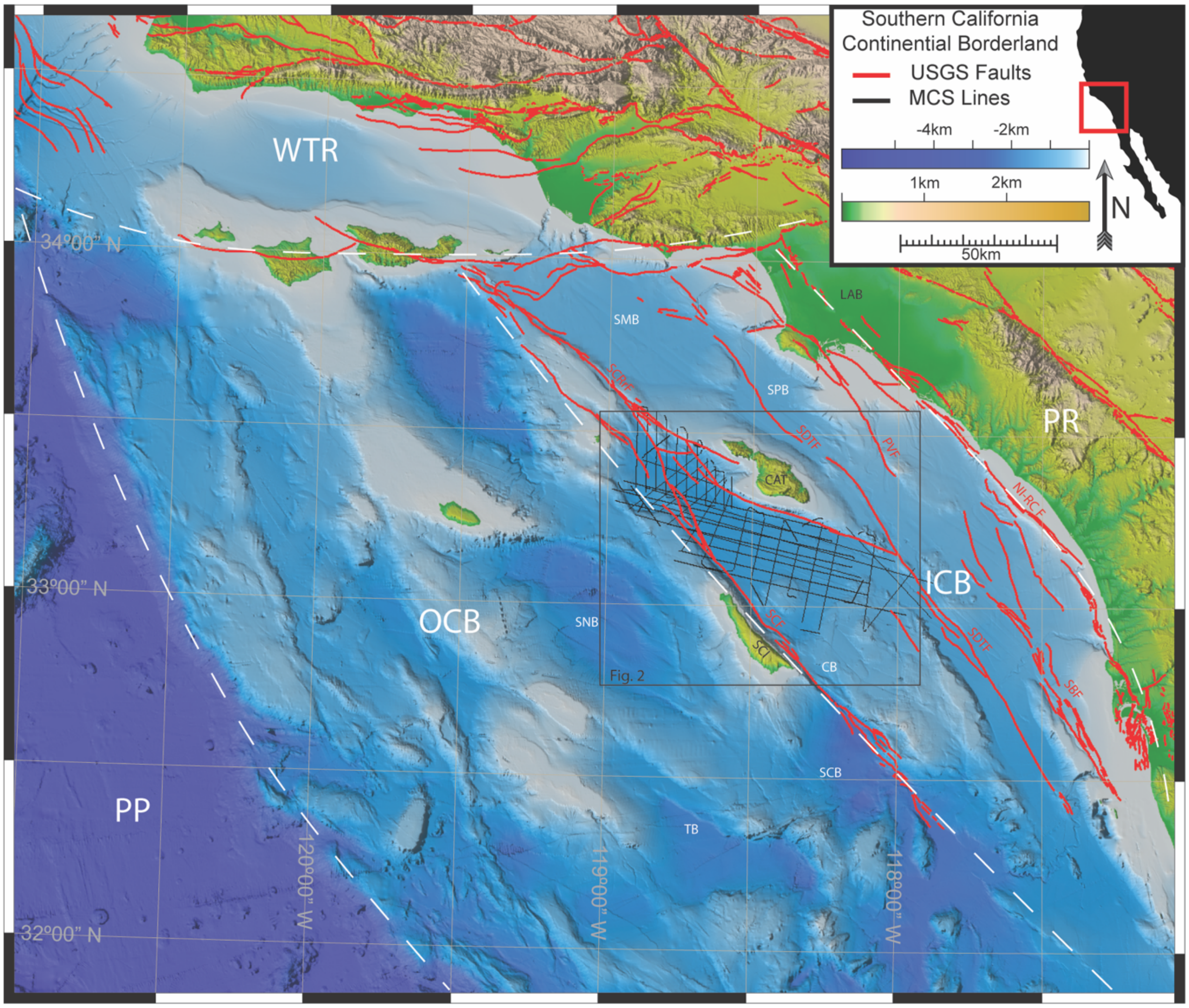

Figure 3.1 Map of the Southern California Borderland.

Topobathymetric surface (National Geophysical Data Center, 2012), and the respective locations of the Inner California Borderland (ICB), Outer California Borderland (OCB), and the Western Transverse Range (WTR), as well as the Peninsular Range (PR) and the Pacific Plate (PP), the boundaries for which have been delineated by dashed white lines. Red lines highlight Quaternary active faults for the region (U.S. Geological Survey). Black Lines are the released Multi-Channel Seismic data used for this seismic facies analysis (Balster-Gee et al., 2017, 2020). See Figure 3.2 for an inset map with the specific lines used within.

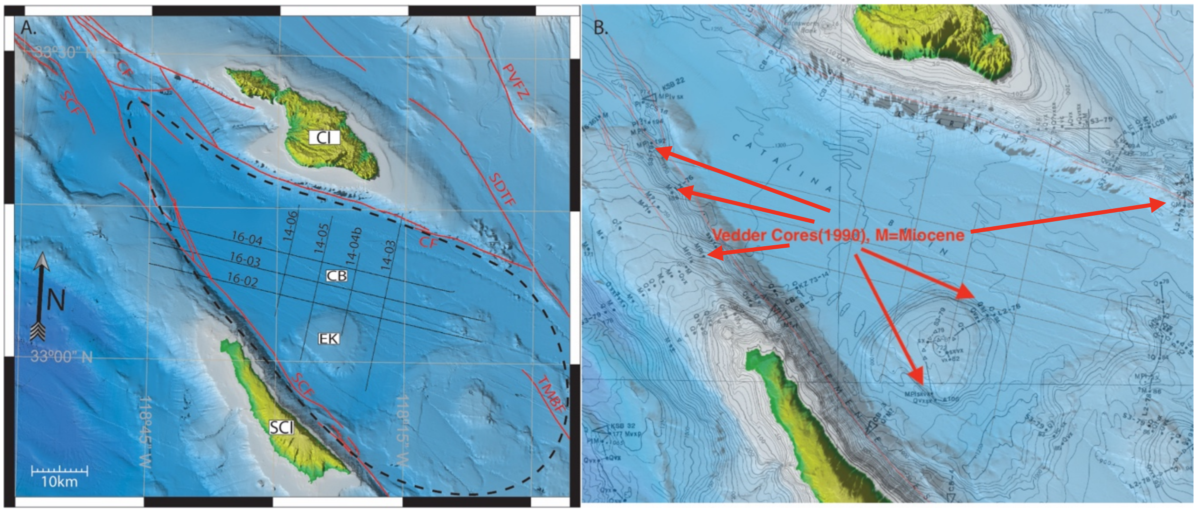

Figure 3.2 A. Detailed map of the Catalina Basin (CB).

CB is denoted with a dashed black line and the respective lines used for this analysis are solid black. The locations of Emory Knoll (EK), San Clemente Island (SCI), and Catalina Island, as well as the faults (red lines) are highlighted for reference. See Figure 1 for location. 2. B. Vedder's (1990) map overlaid on the topobathymetric surface; locations of Miocene aged sampled are highlighted with red arrows.

Parsons, 1995; Atwater and Stock, 1998), including the transition of the southwestern margin of the United States from a subduction zone to the oblique transform margin observed today. There have been many models to explain the morphology of the CCB and distribution of the Phanerozoic rocks (Normark and Piper, 1972; Vedder and Moore, 1976; Vedder et al., 1979; Berner et al., 1983; Teng and Gorsline, 1989; Legg et al., 1991; Glazner, 1991; Legg, 1991; Cole and Basu, 1995; Bohannon and Parsons, 1995; Atwater and Stock, 1998; Bohannon and Geist, 1998; Behl, 1999; Grove et al., 2008; Morton et al., 2014; Francis et al., 2019; Walton et al., 2020). These models generally describe various processes that have resulted in the current distribution of geologic providences within the CCB: the Inner California Borderland (ICB), the Outer California Borderland (OCB), the Western Transverse Range (WTR), as well as the offshore islands within the CCB (Figures 3.1 & 3.2).

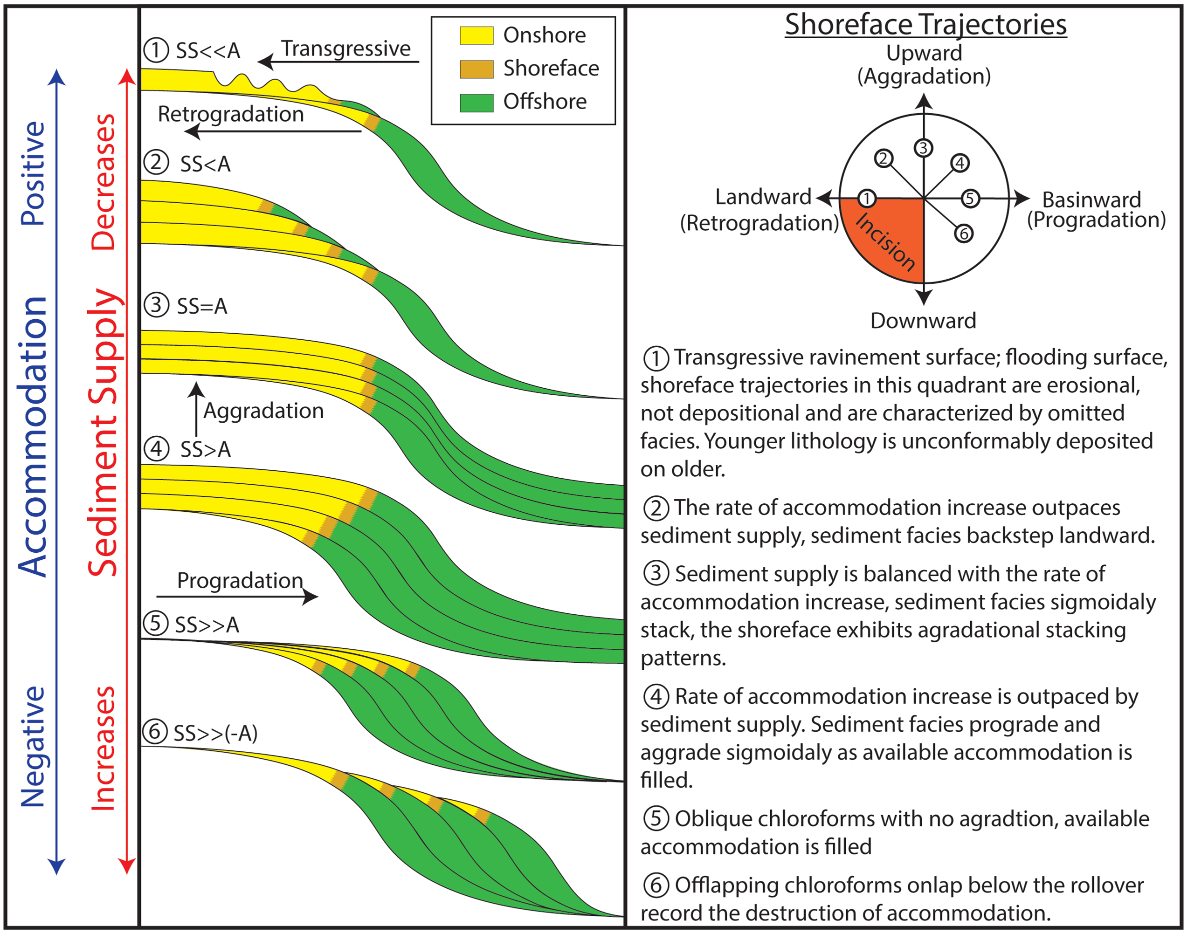

① Transgressive ravinement surface; flooding surface, shoreface trajectories in this quadrant are erosional, not depositional and are characterized by omitted facies. Younger lithology is unconformably deposited on older.

② The rate of accommodation increase outpaces sediment supply, sediment facies backstep landward.

③ Sediment supply is balanced with the rate of accommodation increase, sediment facies sigmoidaly stack, the shoreface exhibits agradational stacking patterns.

④ Rate of accommodation increase is outpaced by sediment supply. Sediment facies prograde and aggrade sigmoidaly as available accommodation is filled.

⑤ Oblique chloroforms with no agradtion, available accommodation is filled

⑥ Offlapping chloroforms onlap below the rollover record the destruction of accommodation.

Figure 3.3 Shoreface trajectories modified from VanWagoner et al. (1990).

Shoreface trajectories detail the resultant sequence stratigraphic architecture formed by the interplay of accommodation and sediment supply.

Recently released Multi-Channel Seismic (MCS) data (Figure 3.1) (Balster-Gee et al., 2017, 2020) collected within the Catalina Basin, one of the many basins that make up the ICB, were used to develop a conceptual model for the evolution of the CB (Walton et al., 2020). Walton et al. (2020) makes several predictions for the geologic evolution of the CB and the timing of recent active deformation within the ICB. In order to test their conceptual model predictions, we interpreted the MCS data in combination with the sediment data of Vedder (1990) (Figures 3.1 & 3.2). Employing a sequence stratigraphic approach (Figures 3.3 & 3.4), we present key indicators of relative sea-level (RSL) change and the attendant depositional response (Figures 3.3 & 3.4) (Christie-Blick and Biddle, 1985; Van Wagoner et al., 1990; Christie-Blick, 1991; Posamentier et al., 1992; Driscoll and Karner, 1999; Catuneanu, 2006).

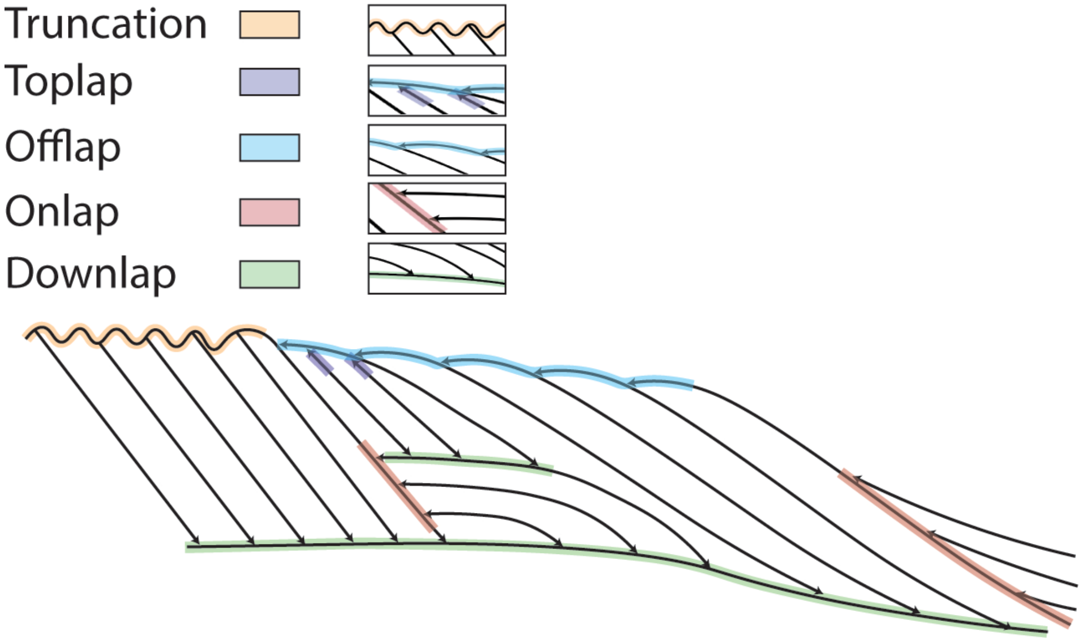

Figure 3.4 Types of stratal terminations (highlighted for clarity).
Stratal terminations used to interpret basin architecture, modified from Catuneanu (2006).

# 3.4.0 Background

There is broad agreement that Cretaceous and Tertiary subduction influenced much of the geology that defines the physiography of North America, and Southern California is no exception. Subduction with distinct episodes of dextral and sinistral convergence (Glazner, 1991) emplaced the Peninsular Range (PR) (Figure 3.1), the now subaerial batholith (Morton et al., 2014) of the once active continental-oceanic convergent plate boundary (Atwater, 1970; Lonsdale, 1991). Regionally significant metamorphic blueschist, characteristic of pressures and temperatures found at typical subduction zones, are observed stratigraphically lower than higher temperature amphibolite facies (Grove et al., 2008). This apparent juxtaposition describes an inverted metamorphic sequence known as the Catalina Schist proposed to be the basement rock underpinning the ICB (Figure 3.1 & 3.2).

Subduction along this western margin continued through the first half of the Cenozoic (~30 Ma), gradually slowed, and finally ceased ~20 Ma as increasingly buoyant oceanic crust fresh from the approaching Pacific-Farallon spreading center resisted subduction under the North American Plate (Atwater, 1970; Lonsdale, 1991; Bohannon and Parsons, 1995; Atwater and Stock, 1998). The termination of subduction and active spreading (~20 Ma) initiated the first phase of deformation of the CCB. Far-field forces from active subduction under the North American Plate to the northwest began to rift the proto-CCB forearc through the same basial shear that stopped subduction in the first place (Atwater, 1970; Lonsdale, 1991; Bohannon and Parsons, 1995; Atwater and Stock, 1998). During the first phase of CCB deformation, regional transtension (Bohannon and Parsons, 1995), triple junction migration (Atwater, 1970; Lonsdale, 1991; Bohannon and Parsons, 1995; Atwater and Stock, 1998), and microplate capture (Nicholson et al., 1994) shaped much of the morphology observed today. The most significant result of this first deformation phase is the >90º clockwise rotation of the WTR, unroofing resulting in the exposure of the Catalina Schist Belt, also referred to as the ICB (Figures 3.2 & 3.3). The >90º rotation of the WTR is generally described as having rotated as one large consolidated block (Nicholson et al., 1994). Others, however, contend the consolidated block model of Nicholson et al. (1994) is unlikely and suggest the paleomagnetic data support the rotation of the WTR was accommodated by smaller microplates, analogous to bookshelf faulting (Schwartz, 2019). Regardless of how the WRT rotated, the evidence of rotation and resultant unroofing of the Catalina Schist is well documented (Kamerling and Luyendyk, 1979; Luyendyk et al., 1980; Hornafius et al., 1986; Nicholson et al., 1994; Schwartz, 2019). Catalina Schist is observed intermingled with many outcrops of the San Onofre Breccia, an early to middle Miocene sedimentary rock, which is strong evidence the Catalina Schist was exposed to erosion and deposition during the early Miocene (Vedder and Howell, 1976; Savage and Weigand, 1994).

The transition between the first phase of CCB deformation and the second phase is marked by regional volcanism, responsible for the formation of many of the offshore islands, such as San Clemente Island (SCI) (Olmsted, 1958; Lamar et al., 1968; Merifield et al., 1971; Cole and Basu, 1995), as well as the exhumation and emplacement of the metamorphic and volcanic rocks that comprise Catalina Island (CI) (Figures 3.1 & 3.2) (Vedder et al., 1979; Savage and Weigand, 1994; Weigand, 1994; Grove et al., 2008). Following this dynamic transition period, the second phase of CCB deformation is noticeably less dynamic, characterized by pervasive dextral faulting. This second deformational stage is also characterized by high RSL, evident by a significant marine incursion into what is presently an onshore subaerial environment, depositing Monterey Group sedimentary rocks throughout the CCB and onshore Southern California (Figure 1) (Arnal and Vedder, 1974; Vedder and Moore, 1976; Vedder and Howell, 1980; Behl, 1999). Following this late Miocene-Pliocene RSL high, base level began to fall to present-day levels, imparting the characteristic marine terrace morphology observable all along the Southern California Coast and the offshore island. Some of the highest subaerial marine terraces are suspected as being Pliocene and are observed at elevations of >500m above present-day sea level (Muhs, 1983; Rockwell et al., 1989; Kern and Rockwell, 1992b; Muhs et al., 1992, 2014; Adler, 2003; Mueller et al., 2009; Haaker et al., 2016; McInnis and Pinter, 2021).

The ICB annually accounts for 15% of the ~48 mm of geodetic right lateral transform offset between the Pacific and North American Plates (Figure 3.1) (Platt and Becker, 2010; Walton et al., 2020). Outboard the Southern California coast, the ICB is bounded to the west by the OCB and the north by the WTR (Figure 3.1). The southern boundary of the ICB extends roughly 100 km into the northern coast of Baja Mexico, where the major through-going faults coalesce onshore.

Measured active slip rates on the offshore faults (Figures 3.1 & 3.2) remain poorly constrained. Onshore expressions are minimal and sampling to provide precise and accurate age constraints on coseismic offset is difficult within the marine environment (Brothers et al., 2009b). The eastern extent of the ICB is the Newport-Inglewood-Rose Canyon Fault (NI-RC) system. The NI-RC is expressed onshore at multiple localities along the highly populated Southern California coast (Figure 3.1) (Maloney et al., 2016b; Sahakian et al., 2017). Onshore and offshore estimates of slip accommodated along the NI-RC range from 0.35-0.55 mm/yr in the North (Grant et al., 1997) and up to 0.5-2.0 mm/yr in the South (Lindvall and Rockwell, 1995). The Palos Verdes Fault (PV) system, west of the NI-RC, is only expressed onshore at its northern extent, as it runs under the Port of Los Angeles, contiguous to the Port of Long Beach, respectively the first and second busiest ports within North America, respectively. Published onshore and offshore estimates of slip along the PV vary by order of magnitude (0.3-3.8 mm/yr) inboard of the San Diego Trough Fault (SDTF) (Fischer et al., 1987; Stephenson et al., 1995; McNeilan et al., 1996; Brothers et al., 2015). The wide variability of slip estimates of the NI-RC and PV systems can be explained by the highly segmented region inboard of the SDTF, having many right and left jogs within a dextral system (Maloney et al., 2015, 2016b; Sahakian et al., 2017; Holmes et al., 2021). Published slip estimates for the SDTF are 1.5 mm/yr (Ryan et al., 2012) and until recently (Walton et al., 2020) marked the western extent for measured Quaternary slip constraints for the ICB. Of the 6-8 mm/yr of geodetic slip, up to 40% is unaccounted for, leading some to speculate the outboard San Clemente Fault (SCF) is responsible for the unaccounted slip rate of ~3.5 mm/yr (Brothers et al., 2009b; Platt and Becker, 2010; Ryan et al., 2012; Walton et al., 2020). Prior to the work of Walton et al. (2020) the SCF had yet to be investigated and characterized with high-resolution seismic reflection data. In a recently published manuscript, Walton et al. (2020) present their observations of data collected within the Catalina Basin (CB), in which they purport that the SCF accommodates a maximum of 3.6 mm/yr of dextral slip.

## 3.5.0 Data and Methods

Approximately 2000km of Multi-Channel Seismic (MCS) reflection data (Figures 3.1 & 3.2) collected within the Santa Cruz and Catalina Basins by the USGS onboard the R/V Robert Gordan Sproul (2014) and the R/V Thomas Thompson (2016) were processed and recently released to the public (Balster-Gee et al., 2017, 2020). Processed MCS data were obtained from the USGS data archive and imported into IHS Kingdom Suite for interpretation.

Topobathymetric surfaces presented within this manuscript (Figures 3.1 & 3.2) have been provided by the National Geophysical Data Center (2012), and are a compilation of available bathymetric datasets gridded together at a resolution of 1 arc-second and also brought into IHS Kingdom Suite for interpretation.

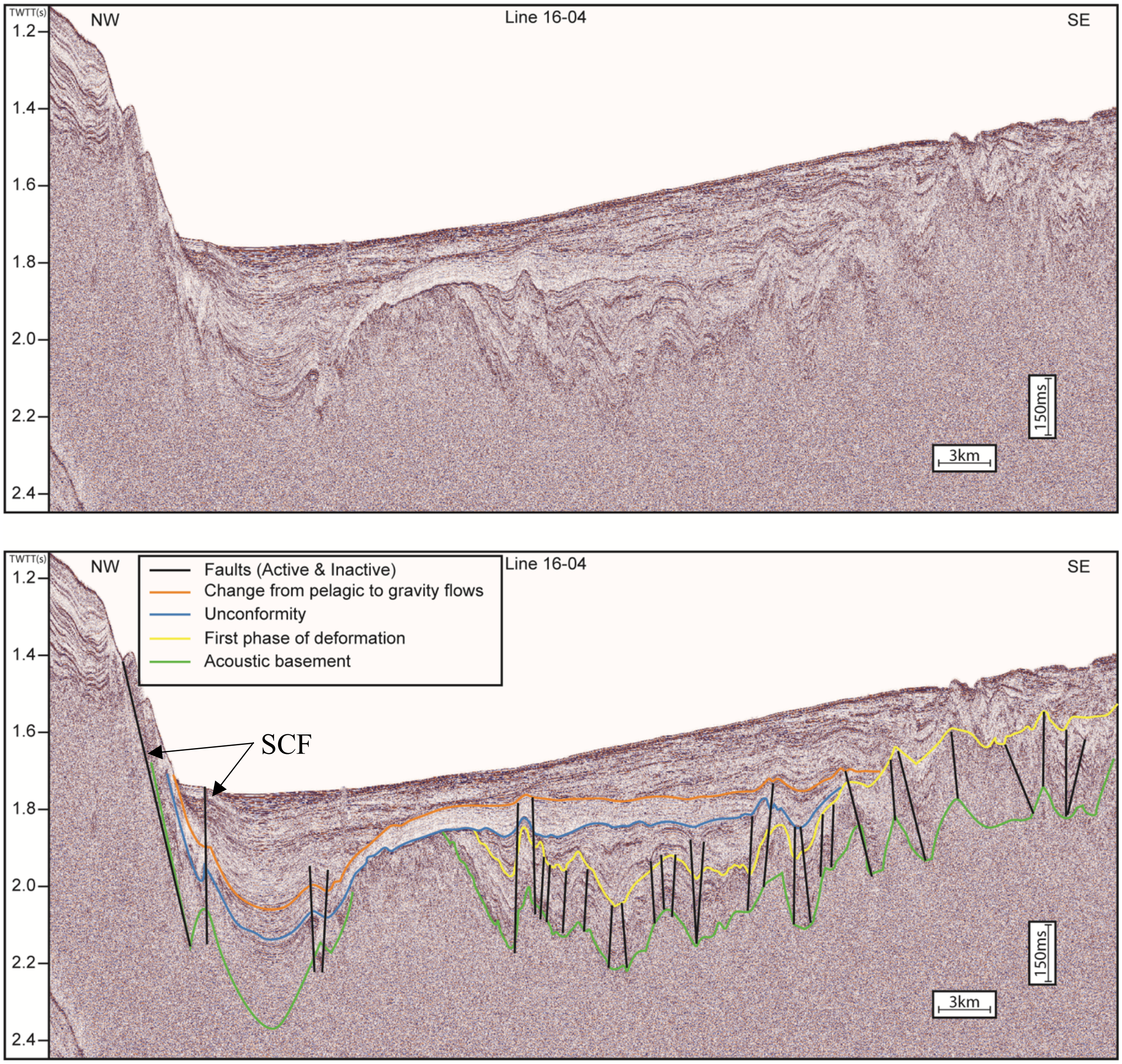

Figure 3.5 Uninterpreted Multi-Channel Seismic (MCS) Profile (16-04) above. Interpreted profile below. See Figure 2 for location. The San Clemente Fault (SCF) is highlighted for reference.

Maps of the compositions and ages of the CCB seafloor (Vedder, 1990) were acquired through the USGS data archive. PDFs were downloaded and digitized and geo-referenced in Google Earth; digitized maps were imported into IHS Kingdom Suite for interpretation (Figure 3.2. B).

## 3.6.0 Results

Here, we present observations of recently released MCS reflection data collected within the Catalina Basin. Seismic data presented herein is described using a combination of structural

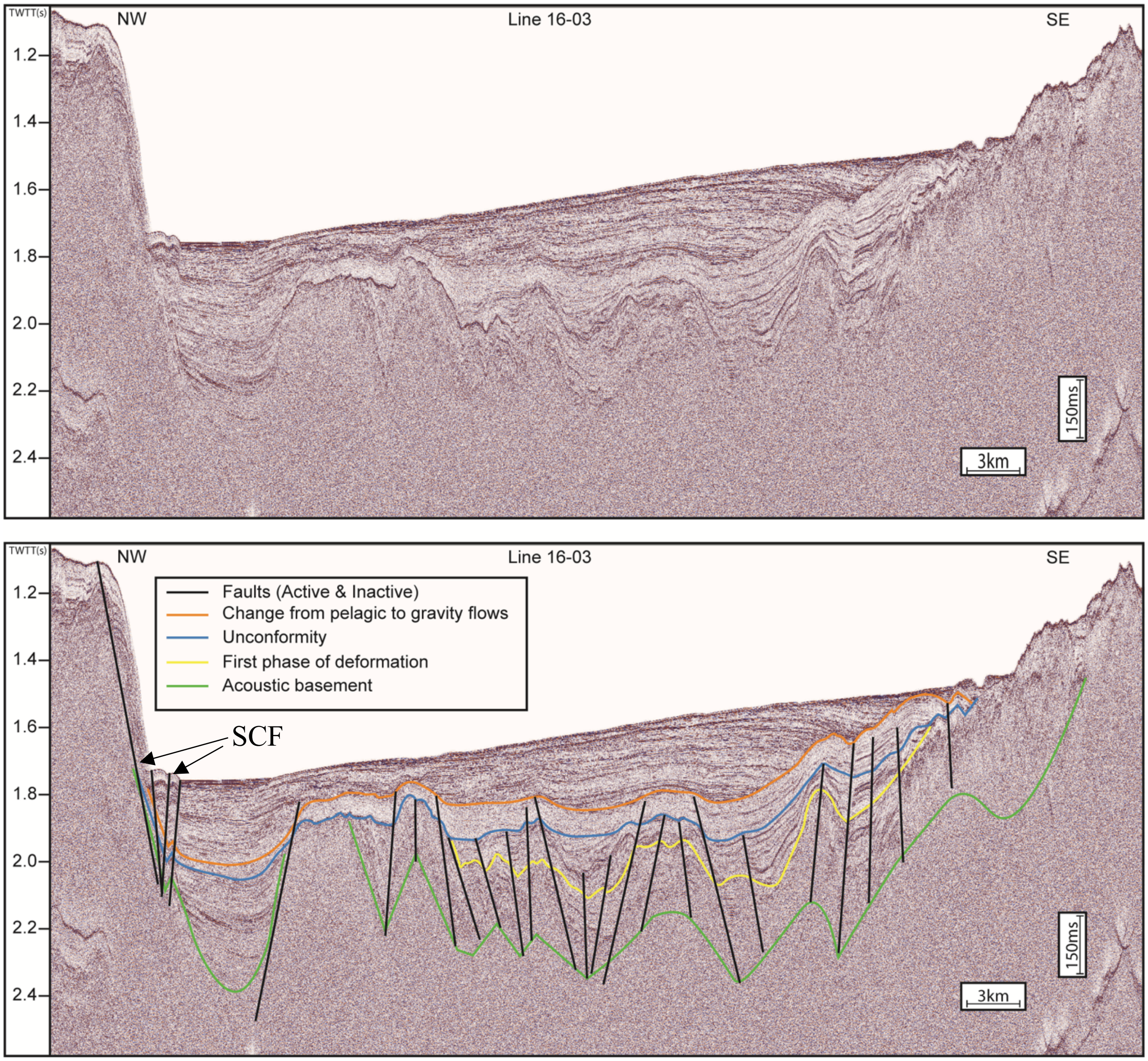

Figure 3.6 Uninterpreted Multi-Channel Seismic (MCS) Profile (16-03) above.

Interpreted profile below. See Figure 3.2 for location. The San Clemente Fault (SCF) is highlighted for reference.

and sequence stratigraphic terminologies (Figures 3.3 & 3.4). Any discussion of depths in meters uses a nominal water velocity of 1500m/s for conversion.

### 3.6.1 Identified Horizons

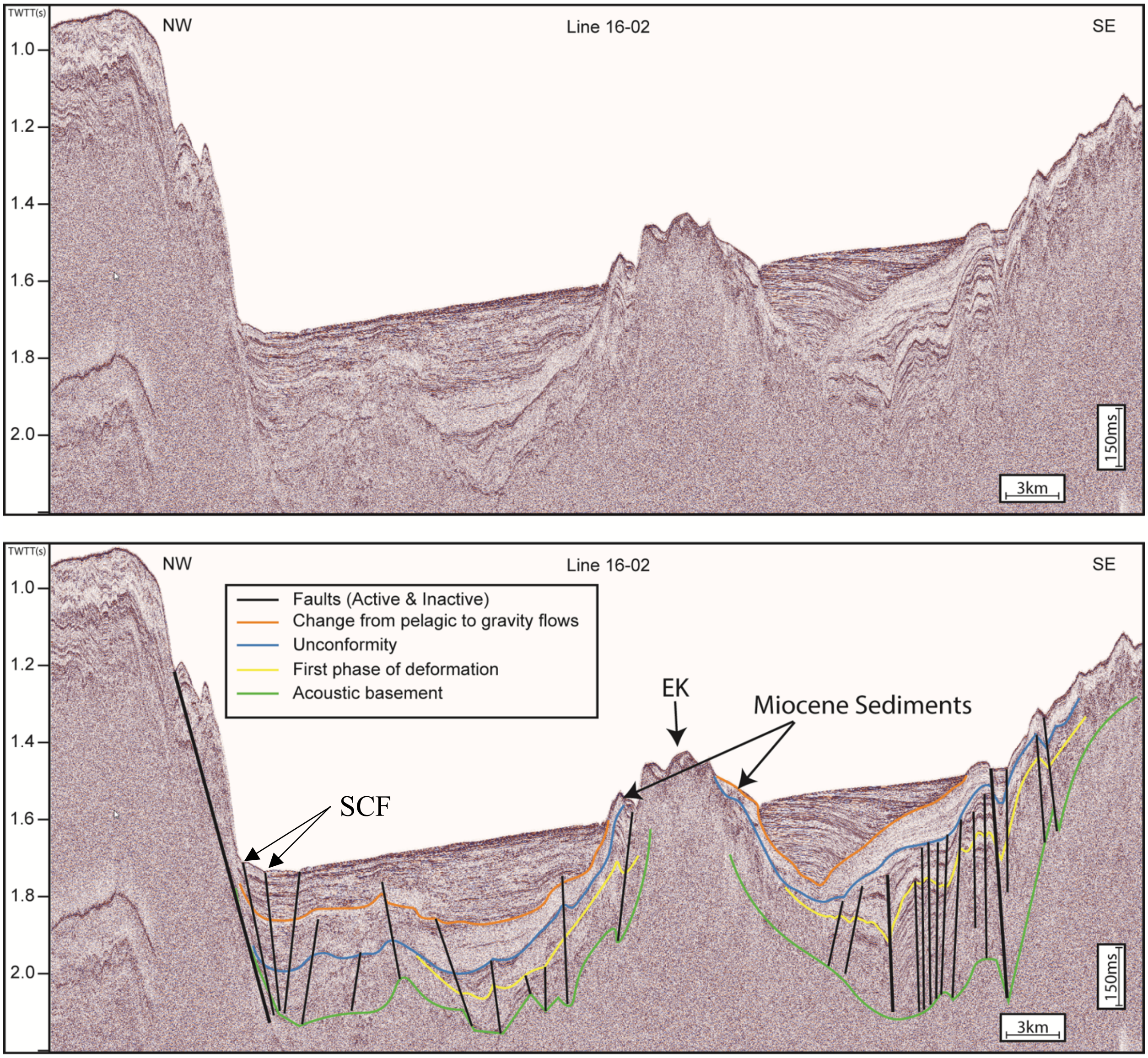

Figure 3.7 Uninterpreted Multi-Channel Seismic (MCS) Profile (16-02) above.

Interpreted profile below. See Figure 2 for location. Locations of Emory Knoll (EK), the San Clemente Fault (SCF) and the location of the Miocene sediments (Vedder, 1990) are highlighted for reference.

Four surfaces observed throughout Catalina Basin have been identified and described below within the MCS data (Figures 3.5, 3.6, 3.7, 3.8, 3.9, 3.10 & 3.11). The deepest surface highlighted in green, is referred to as acoustic basement, separates acoustically incoherent noise below from coherent and highly faulted laminar sediments above. A yellow horizon separates the highly faulted acoustically laminar sediments below from less laminar faulted sediments above. The less laminar sediments exhibit divergence; thickness variations appear being fault controlled.

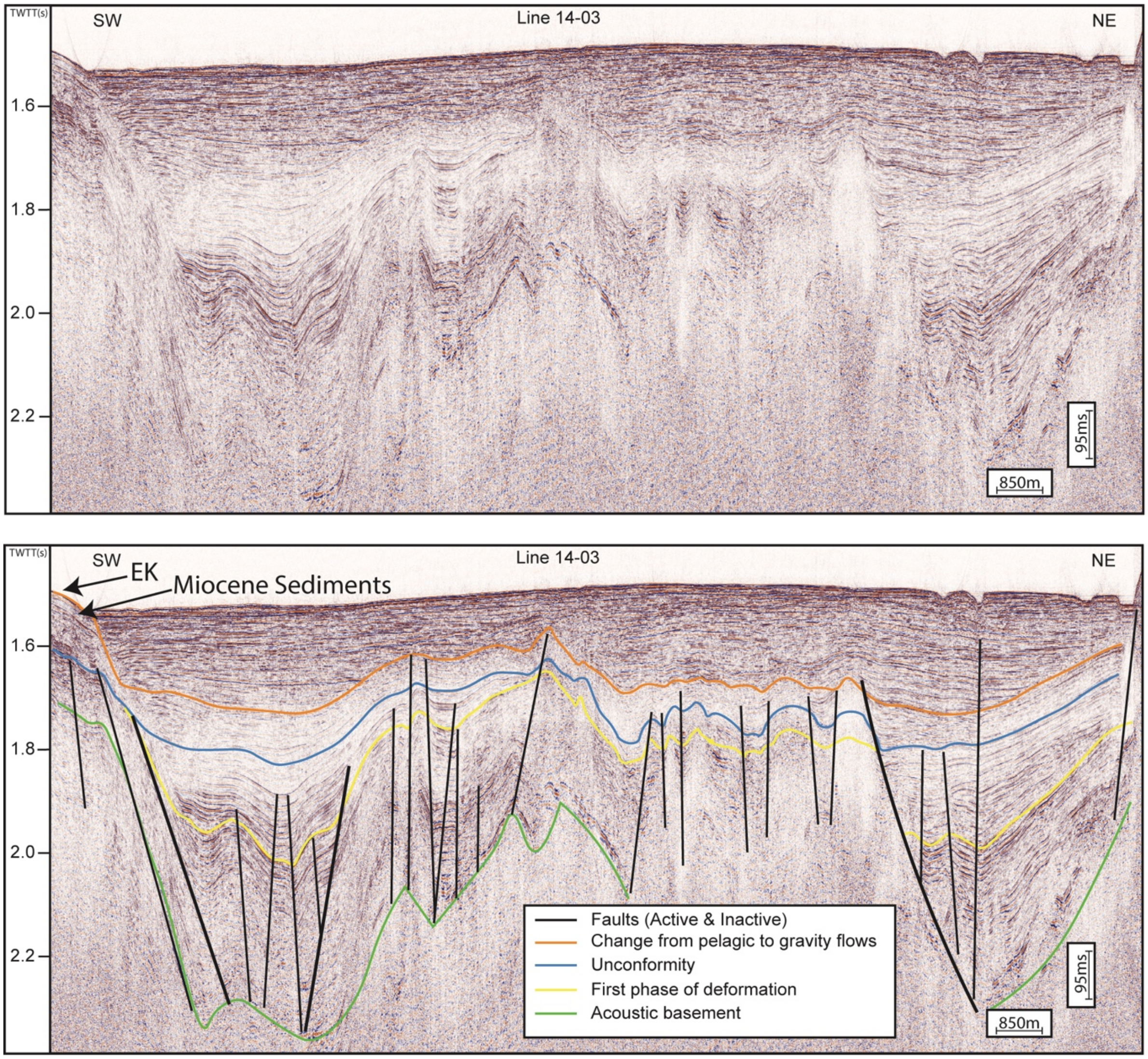

Figure 3.8 Uninterpreted Multi-Channel Seismic (MCS) Profile (16-03) above. Interpreted profile below. See Figure 2 for location.

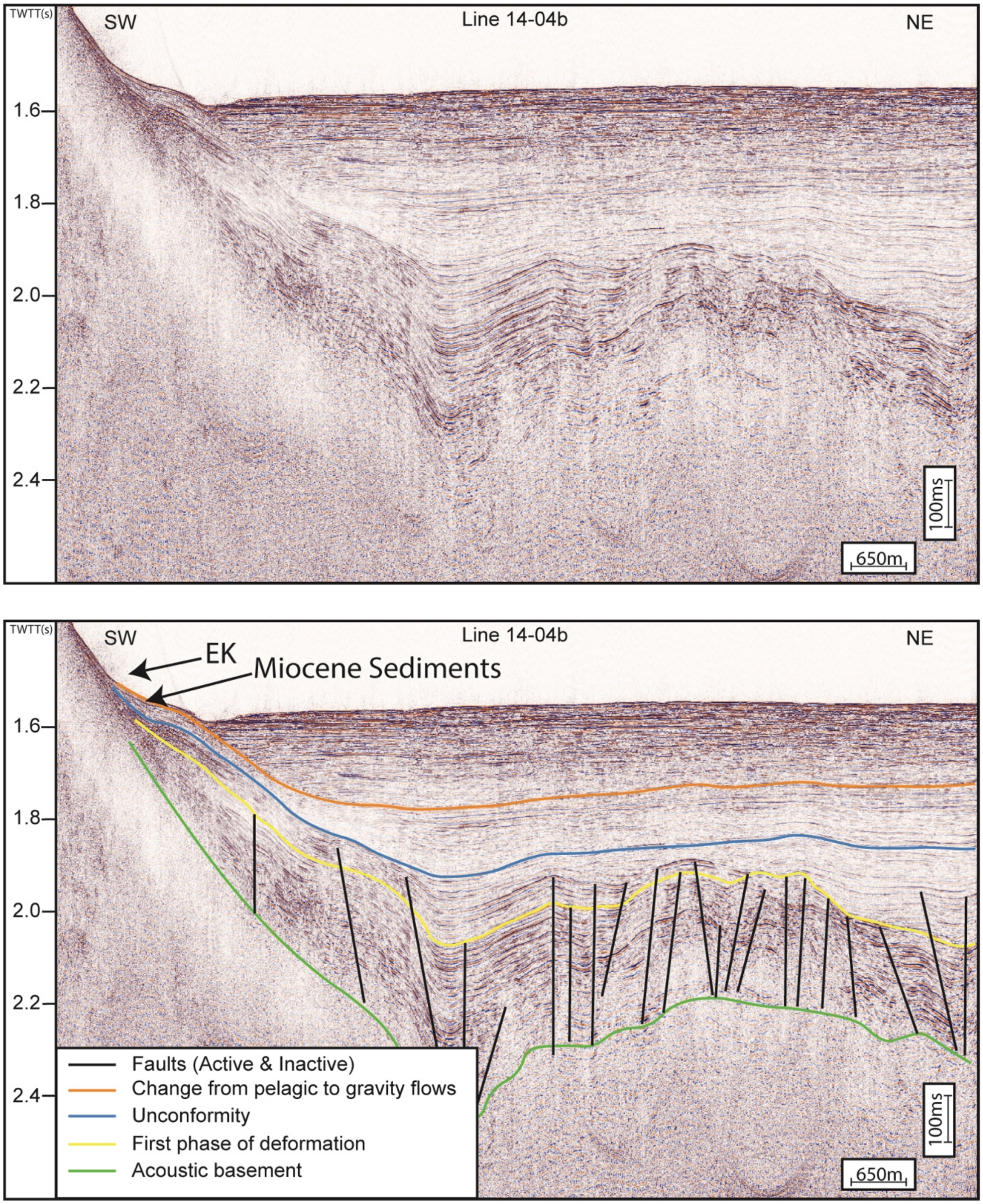

Figure 3.9 Uninterpreted Multi-Channel Seismic (MCS) Profile (14-04b) above.

Interpreted profile below. See Figure 3.2 for location. Emory Knoll (EK) and the location of the Miocene sediments (Vedder, 1990) are highlighted for reference.

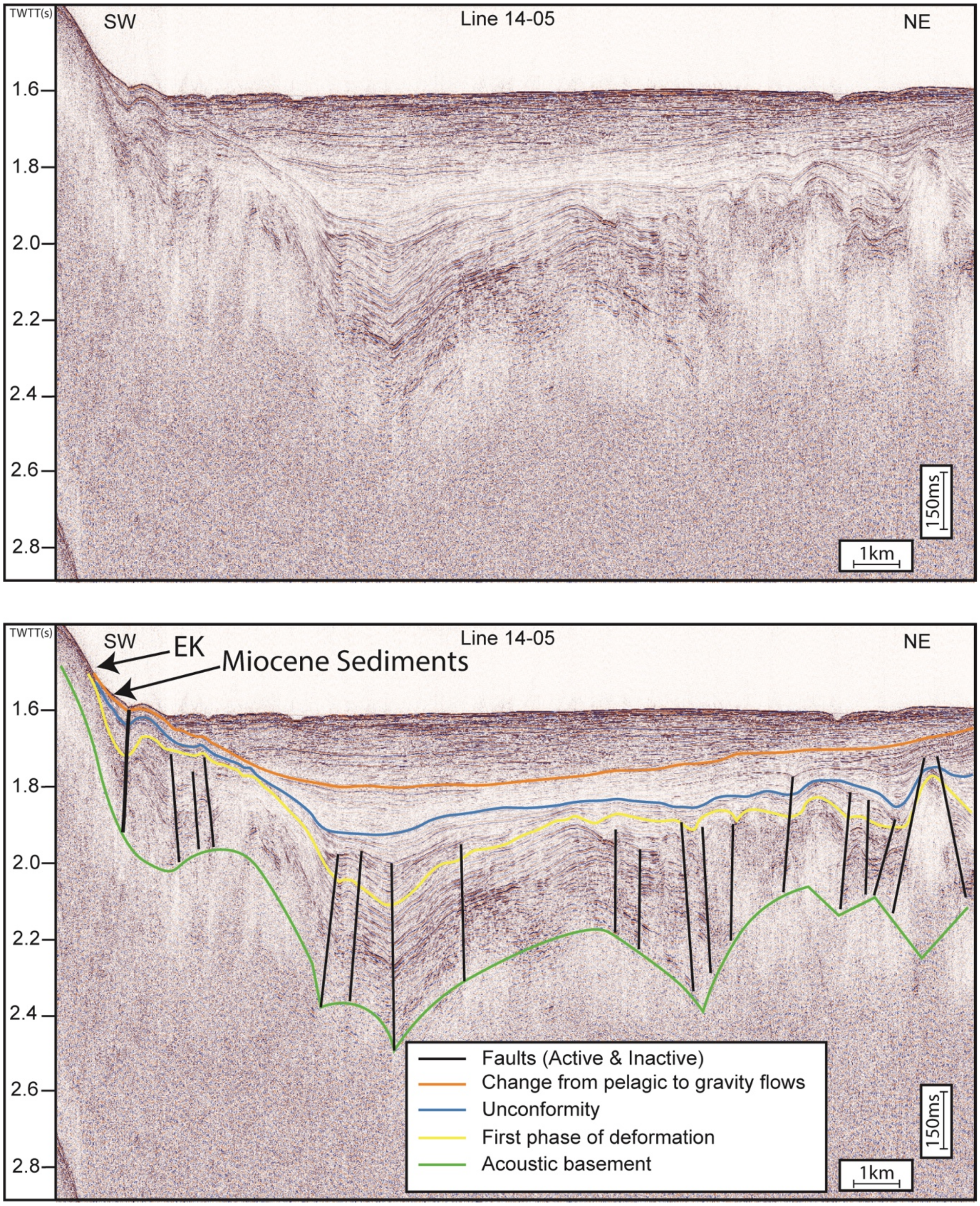

Figure 3.10 Uninterpreted Multi-Channel Seismic (MCS) Profile (14-05) above.

Interpreted profile below. See Figure 3.2 for location. Emory Knoll (EK) and the location of the Miocene sediments (Vedder, 1990) are highlighted for reference.

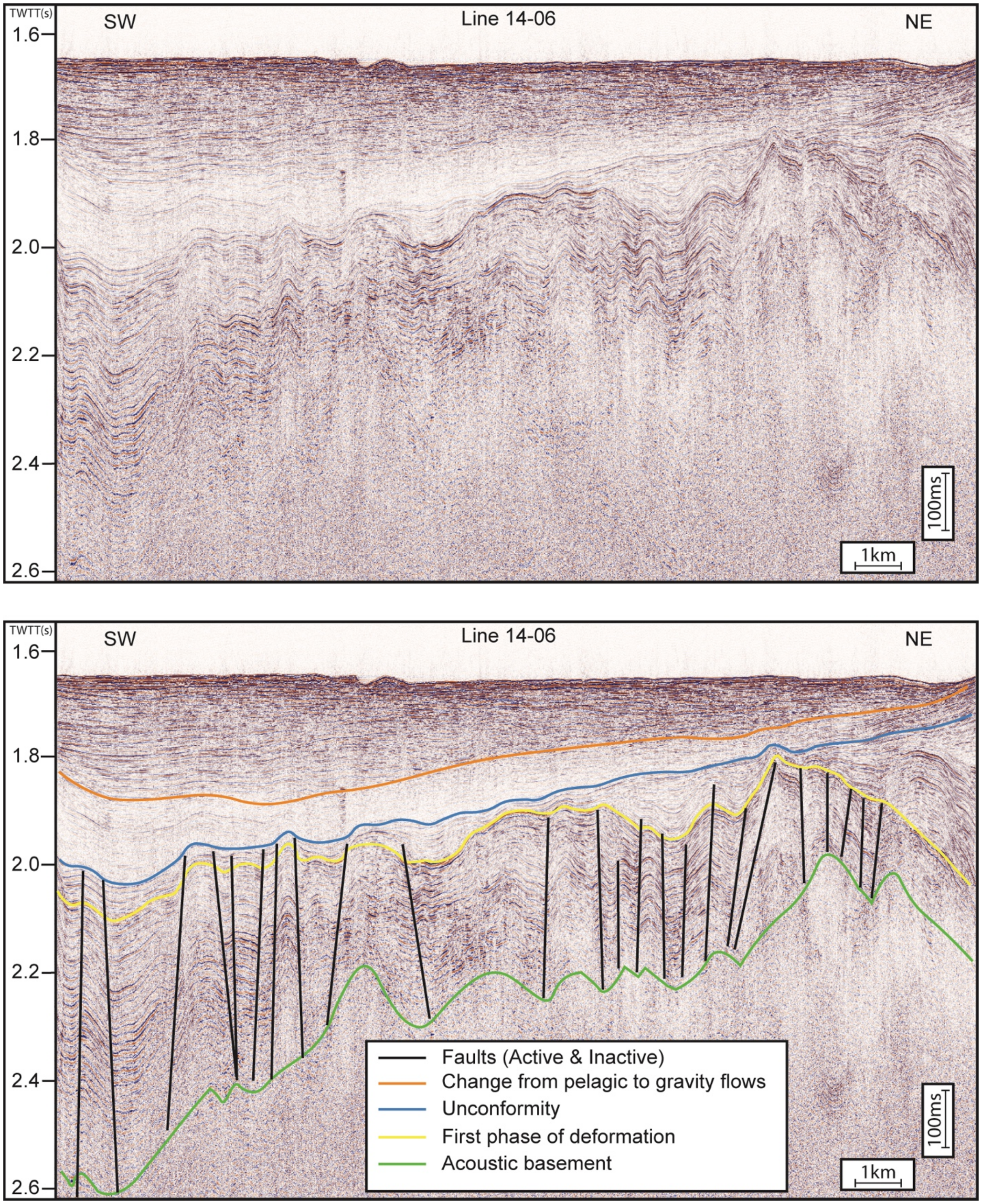

Figure 3.11 Uninterpreted Multi-Channel Seismic (MCS) Profile (14-06) above.

Interpreted profile below. See Figure 3.2 for location. Emory Knoll (EK) and the location of the Miocene sediments (Vedder, 1990) are highlighted for reference.

The blue horizon highlights a basin-wide unconformity that has down cut and through the yellow reflector and the highly faulted layer into the acoustic basement. Above the blue layer, coherent laminar sediments mantle the topography of the blue reflector and have lower amplitude reflectors that distinguish it from other units within the Catalina Basin. This low amplitude unit is noticeably less faulted than the layers below and outcrops at the seafloor around Emory Knoll (Figures 3.7, 3.8, 3.9, 3.10 & 3.11) . Finally, these laminar sediments are capped with another basin-wide unconformity identified by the orange horizon. Above the orange surface overlying sediments onlap and downlap upon the orange surface (Figure 3.5 & 3.6) as the depocenter shifts from the northwest to the southeast. Above the orange horizon, other unconformable surfaces within the stratigraphy cannot be identified with confidence. For this reason, further interpretation within the package above the orange surface is withheld, pending additional seismic data scheduled to be collected in summer 2022 onboard the R/V Sally Ride.

### 3.6.2 Sediment Ages and Compositions

There have been no modern sediment coring campaigns within the Catalina Basin; however, a compilation map of the California Borderland exists, which details the ages and sediment types of seafloor samples collected between 1969 and 1979 (Figure 3.2. B) (Vedder, 1990). These samples have been characterized by sediment type and age; reported ages are based on the last known occurrence of the fossil assemblages within the collected samples. Little is known about the stratigraphy of these samples, a probable consequence of the sample types, which are mostly dredge, box, Van-Veen, and dart cores, with few gravity and piston cores. Given the shallow nature of these coring systems, most of the locations identified by the Vedder

(1990) maps have one or two ages attributable to the sample site. Most sampled sites  the Vedder (1990) maps have one or two ages attributable to the sample site. Most sampled sites within the Catalina Basin record Quaternary age sediments, and are denoted by the letter Q. However, along the ridges that bound the Catalina Basin and the perimeters of the volcanic domes (i.e., Emory Knoll), outcrops of Miocene and Pliocene sediments have been sampled, and are denoted by M and Pl, respectively (Figure 3.2.B). These observations will provide important context in the following discussion.

## 3.7.0 Discussion

In the following discussion, we will evaluate the MCS and sediment data to establish a chronostratigraphic framework for the evolution of Catalina Basin. We will compare how seemingly minor differences in seismic interpretations can result in contradictory models to explain the observed sequence stratigraphic architecture, which have implications for the basin evolution, recency of deformation and the seismic hazard of Southern California.

Acoustic basement describes a surface that delineates identifiable seismic reflectors above, from incoherent noise below, and may or may not define a change in lithology. The acoustic basement in CB most likely represents a transition from marine sediments to the Catalina Schist, the basement rock theorized to underlie the ICB (Bohannon and Geist, 1998).

Mantling the acoustic basement are pre-tectonic sediments, which exhibit little to no identifiable growth strata or divergence of the reflectors (i.e., thickness variations are not fault-controlled). This package is heavily faulted and has experienced varying amounts of post-depositional deformation, which is evident from the pervasive reverse faulting imaged in the seismic data.

The yellow horizon records the onset of deformation as it separates pre-tectonic sediments below from syn-tectonic sediments above. The facies of the syn-tectonic deposits thicken and thin above the yellow horizon, a process controlled by accommodation being created and destroyed during the early stage of deformation. As a result, there are noticeably fewer faults that offset the syn-tectonic sediments than the pre-tectonic sediments. and even less faulting persists through the blue horizon.

The blue horizon highlights a basin-wide unconformity. It is difficult to explain this basin-wide unconformity, which has eroded and down cut the pre and syn-tectonic sediments by any other process than a base-level fall. Base-level defines a surface above which sediments are eroded and below sediments are deposited (Figures 3.3 & 3.4). Base-level is generally synonymous with RSL, which is the combination of eustatic sea level and local tectonic processes. Based on the erosional truncation observed in the seismic data (Blue horizon), RSL was around 1500m lower than present-day sea level (Figures 3.5 & 3.6).

The sediments above this blue unconformity outcrop around Emory Knoll (Figures 3.7, 3.8, 3.9 & 3.10). It is important to note that the sediments in the unit above the blue horizon mimic the topography of the blue unconformity and are in large part acoustically transparent. Note the onlapping and downlapping reflectors on the orange horizon, suggests the tectonic deformation occurred prior to sediment infilling above the orange horizon.

The orange horizon marks an important surface which the overlying sediments onlap and downlap upon (Figures 3.3 & 3.4) and separates two different styles of deposition within the Catalina Bains. The timing of the orange surface most likely coinciding with the middle Miocene submarine exposure of Emory Knoll, San Clemente Island, and Santa Catalina Island, setting the stratal geometry of the blue and orange horizons into their present-

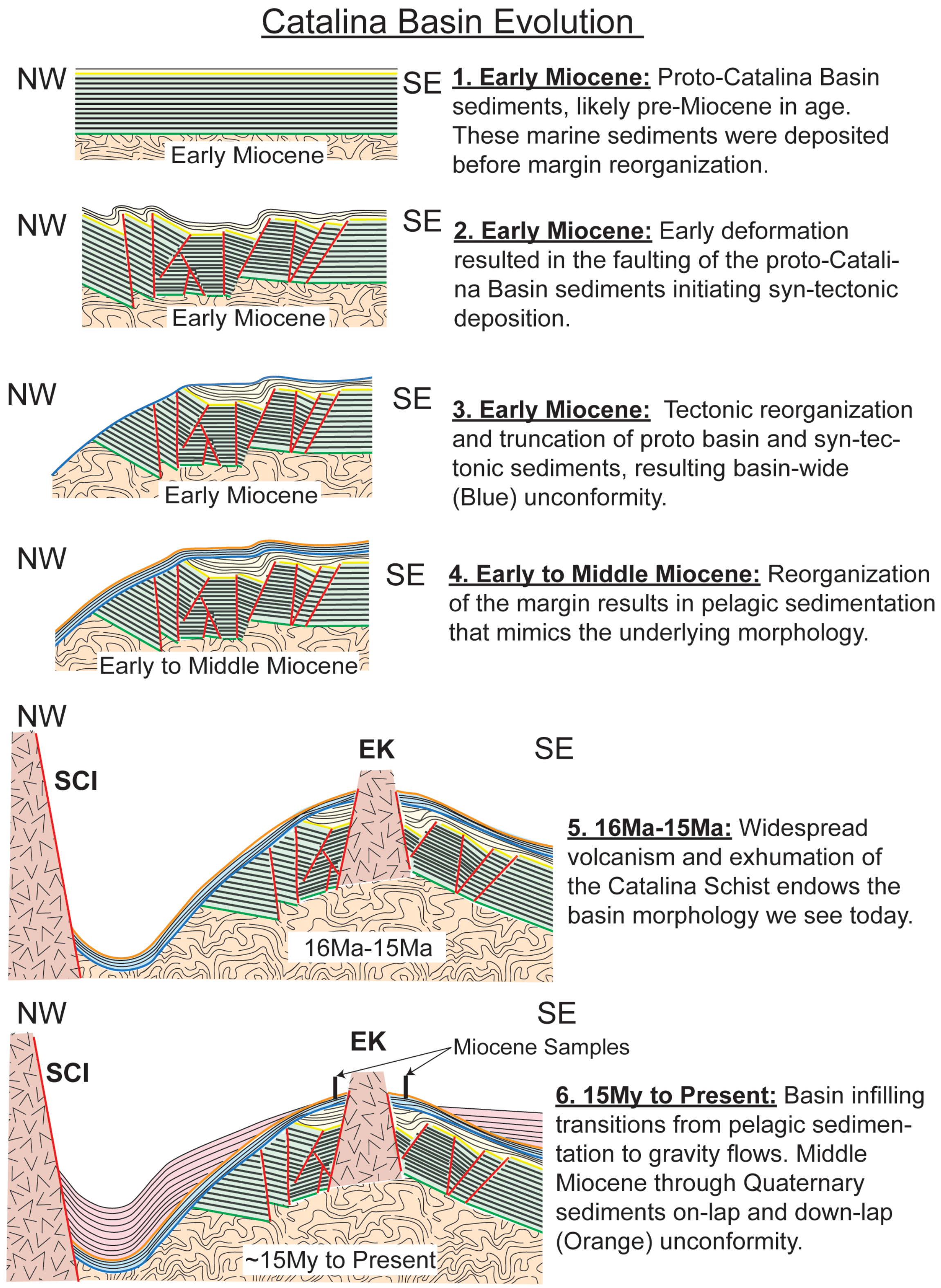

Catalina Basin Evolution

**1. Early Miocene:** Proto-Catalina Basin sediments, likely pre-Miocene in age. These marine sediments were deposited before margin reorganization.

**2. Early Miocene:** Early deformation resulted in the faulting of the proto-Catalina Basin sediments initiating syn-tectonic deposition.

**3. Early Miocene:** Tectonic reorganization and truncation of proto basin and syn-tectonic sediments, resulting basin-wide (Blue) unconformity.

**4. Early to Middle Miocene:** Reorganization of the margin results in pelagic sedimentation that mimics the underlying morphology.

**5. 16Ma-15Ma:** Widespread volcanism and exhumation of the Catalina Schist endows the basin morphology we see today.

**6. 15My to Present:** Basin infilling transitions from pelagic sedimentation to gravity flows. Middle Miocene through Quaternary sediments on-lap and down-lap (Orange) unconformity.

Figure 3.12 Schematic illustrating the evolution of the Catalina Basin.

Emory Knoll (EK), San Clemente Island, and the location of the Miocene sediments of Vedder (1990) are highlighted for context. See previous seismic profiles for an explanation of the color-coded surfaces.

day configurations. Post orange horizon sediments within the basin, first fill the smaller sub-basin along the San Clemente Fault, back-stepping southeast, onlapping, and downlapping the uplifted orange surface around Emory Knoll, San Clemente Island, and Catalina Island (Figures 3.5, 3.6, 3.7, 3.8, 3.9 & 3.10).

### 3.7.1 Catalina Basin Evolution

Analysis of the seismic reflection data reveals a two-phase evolution of the Catalina Basin, where pre-deformational marine sediments were deposited and subsequently deformed. During this first phase of deformation, varying amounts of tectonic shortening faulted and translated the pre-deformational sediments, while syn-tectonic deposition continued through this first phase (yellow horizon) (Figure 13.12.1 & .2). Near the end of the first deformation phase, base-level fell, eroding and scouring the marine sediments and basement lithology, marked by a basin-wide angular truncation (blue) (Figure 13.12.3). Mantling this lower unconformity are marine sediments that drape over the blue unconformity recording pelagic sedimentation. The lower amplitude reflector in this section means a lower degree of variation in the acoustic impedance within the observed layers, a seismic character influenced by grain size, sediment type, porosity, as well as many other factors (Figure 13.12.4).

The boundary between the first and second phases of Catalina Basin deformation (orange horizon) is marked by exhumation and uplift of Emory Knoll, San Clemente Island, and Catalina Island, processes that resulted in the deformation of the Catalina Basin stratigraphy into its present-day morphology(Figure 13.12.5). Following the orange unconformity, Basin infilling transitions from pelagic sedimentation to gravity flows recorded by the backstepping sediments that onlap and downlap upon the orange unconformity, as the depocenter migrated from northwest parts of the Catalina Basin to the southeast (Figure 13.12.6).

As stated before, the Catalina Basin has recorded ~30 My of deformation–the specific timing of the various phases of this deformation is presented in our conceptual model of CB evolution (Figure 3.12). The following age model for our seismic facies analysis applies ages of collected seafloor samples and honors regional geologic data.

### 3.7.2 Age Model

The outcropping of the Miocene sediments identified by the Vedder (1990) are possibly the most substantial evidence available to constrain the evolution of the Catalina Basin (Figure 3.2. B). The Miocene age determination by Vedder (1990) is too broad to use alone; however, the character of the package, its relationship with the unconformities that bound it, and the morphology of the boundaries themselves (Figure 3.7, 3.8, 3.9, & 3.10), suggest that these low amplitude pelagic sediments were deposited before the last phase of ICB deformation at the Early to Middle Miocene boundary (16.5 Ma-14.8 Ma) (Olmsted, 1958; Lamar et al., 1968; Merifield et al., 1971). This timing coincides with the exhumation of the Catalina Schist basement (Wright, 1991; Crouch and Suppe, 1993), the volcanism that formed SCI (Olmsted, 1958; Lamar et al., 1968; Merifield et al., 1971), and the middle Miocene volcanism throughout the American Southwest (Cole and Basu, 1995; Dickinson, 1997).

If the interpretation of the orange unconformity having occurred at or around the middle Miocene is correct. In this scenario, the pre-tectonic sediments would pre-date the Miocene and be equivalent to the forearc sediments discussed by Bohannon and Geist (1998). Bohannon and Geist (1998). Tang and Gorsline (1989) purported that pre-Miocene sediments are not observed in the ICB, a likely consequence of the low-quality seismic reflection data available at the time and minimal core data. The seismic data they employed failed to image the stratal architecture characteristics of the pre-tectonic sediments above the acoustic basement that are imaged in the recently released MCS data (Balster-Gee et al., 2017, 2020).

Given the orange unconformity is middle Miocene in age (15 My), the observed sequence stratigraphic architecture is consistent with a two-stage deformational model of the California Continental Borderland evolution proposed by Bohannon and Geist (1998). Our conceptual model describes the styles of deposition and deformation that have occurred in the Catalina Basin from the late Oligocene to the present (Figure 3.12).

1. **Pre-Miocene**: Proto-Catalina Basin sediments are likely pre-Miocene in age and based on their conformable nature were deposited in a tectonically quiescent period. The shape of this proto-basin is unknown, however, the sediments are likely equivalent to the forearc sediments of Bohannon and Geist (1998).
2. **Early Miocene**: The first stage of deformation of the ICB resulted in deformaiton of the proto-Catalina Basin sediments. The sediment deposited during this deformation stage exhibt fault controlled charicteristics consistent with syn-tectonic deposition (yellow horizon) (Driscoll and Hogg, 1995).
3. **Early Miocene:** Towards the end of the first deformation phase, base-level fell, truncating and eroding the pre-tectonic and syn-tectonic sediments, downcutting into the acoustic basement (blue horizon).
4. **Early to Middle Miocene:** Reorginization of the marin results in pelagic sedimentaion being the dominant depositonal style, mantleing the underlying Early Miocene regional unconformity (blue to orange).

5. **16Ma-15Ma:** The first phase of California Borderland deformation concludes with the exhumation of the Catalina Schist and regional volcanism. The 16Ma-15Ma timing coincides with the emplacement of SCI, Catalina Island, and Emory Knoll, setting the present-day basin morphology and uptilting the early to middle Miocene sediments around the flanks and volcanics of the Catalana Basin.
6. **15Ma to Present:** Basin infilling transitons from pelagic sedimentation to gravity and current controlloed, documented by the on-lapping and down-lapping of the Middle to Late Miocene through Quaternary sediments on the (orange) Middle Miocene unconformity. The infilling stratal geometry above orange suggests the early phase of deformation is not loger influancing the depositonal system.

Eventhough I interpreted the same MCS seismic data used by Walton et al. (2020) and constrained the subbottom data with the same seafloor sample map (Vedder, 1990), the derived conceptual models are markedly different. The underlying reason our models do not agree is the proposed timing of the blue and orange unconformities. The conceptual model of Walton et al. (2020) is based largely on the seismic facies analysis of Teng and Gorsline (1989), interpreting these two unconformities as Late Miocene and Pliocene surfaces. If the observed unconformities within the Catalina Basin record Late Miocene and Pliocene base-level fall as reported by Walton et al. (2020), how do we explain the occurrence and distribution of Monterey Group marine sedimentary rocks? The Monterey Group marine sedimentary rocks were deposited during this time and observed as far inland as the Basin and Range (Behl, 1999). During the Late Miocene, the Southern California region experienced a broad marine incursion with RSL hundreds of meters higher than present-day levels (Arnal and Vedder, 1974; Vedder and Moore, 1976; Vedder and Howell, 1980; Teng and Gorsline, 1989). Furthermore, the timing of their Late Miocene and Pliocene surfaces is inconsistent with the numerous mapped subaerial marine terraces observed along the Southern California coast and the offshore islands. The well-documented subaerial marine terraces are strong evidence that during the Pliocene and Early Quaternary period, RSL was >380 m above present-day sea level (Haaker et al., 2016), a disagreement of almost 2,000m. In our concepual model, the two unconformities are substantially older than purported by Walton et al. (2020), and are more consistent with mapped stratal geometry throughout the Catalina Basin.

## 3.8.0 Conclusions

Recently published seismic facies analysis of the Catalina Basin interprets two basin-wide unconformities attributed to Late Miocene and Pliocene tim periods. The timing of these surfaces has implications for the tectonic evolution of the Catalina Basin and the California Continential Borderland. In addition, these surfaces have implications on the timing and recency of faulting offshore Southern California, home to ~20 million people. We tested the Walton et al. (2020) conceptual model using a sequence stratigraphic approach and attribute these same unconformities to the Early and Middle Miocene, an interpritaion supported by the ages of the sediments found outcropping within the Catalina Basin and the distribution of Late Miocene marine sediments. Our our interpritaions are aloso consistant with the Pliocene through Quaternary marine terraces scoured into the Southern California coast and offshore islands. Further evidence is needed to corroborate our conclusions in the form of sediment cores that sample deeper into the stratigraphy of the Catalina Basin, as well as high-resolution sub-bottom data, scheduled to be collected during the summer of 2022.

## 3.9.0 Acknowledgments

Chapter 3 Derosier, B.J., Driscoll, N.W., Seismic facies analysis of the Catalina Basin; Implications of the Evolution of The Inner California Borderland. The author of the dissertation was the primary researcher and author of this manuscript. This manuscript is not currently ready for publication as further data is needed. Additional ship-time is necessary to collect high-resolution sub-bottom data scheduled for August 2022 onboard the R/V Sally Ride.

# Chapter 4

# New High Resolution Sub-bottom Profiler Images Active Deformation Within the Outer California Borderland

## 4.1.0 Abstract

New high-resolution seismic reflection dataset collected along the Ferrelo Fault Zone offshore Southern California reveals active deformation within the Outer California Borderland (OCB). In June 2021, the R/V *Sally Ride* was outfitted with a state-of-the-art sub-bottom profiler capable of collecting data of decimeter resolution at full ocean depths >2000 Meters Below Sea Level (mbsl). During the sonar commissioning cruise, the South Tanner Basin (STB), one of the many basins within the OCB was surveyed. Approximately 135 km of Kongsberg SBP 29 sub-bottom data were collected, along with 9.5 km of Knudsen 4 kHz sub-bottom data for direct comparison. Styles of deformation observed along this active strike-slip fault include pressure ridges, transtensional relay ramps, and anticlinal folds. The data support the Ferrelo Fault as being active within the last 1,000 years, an important observation that will influence future seismic hazard assessments.

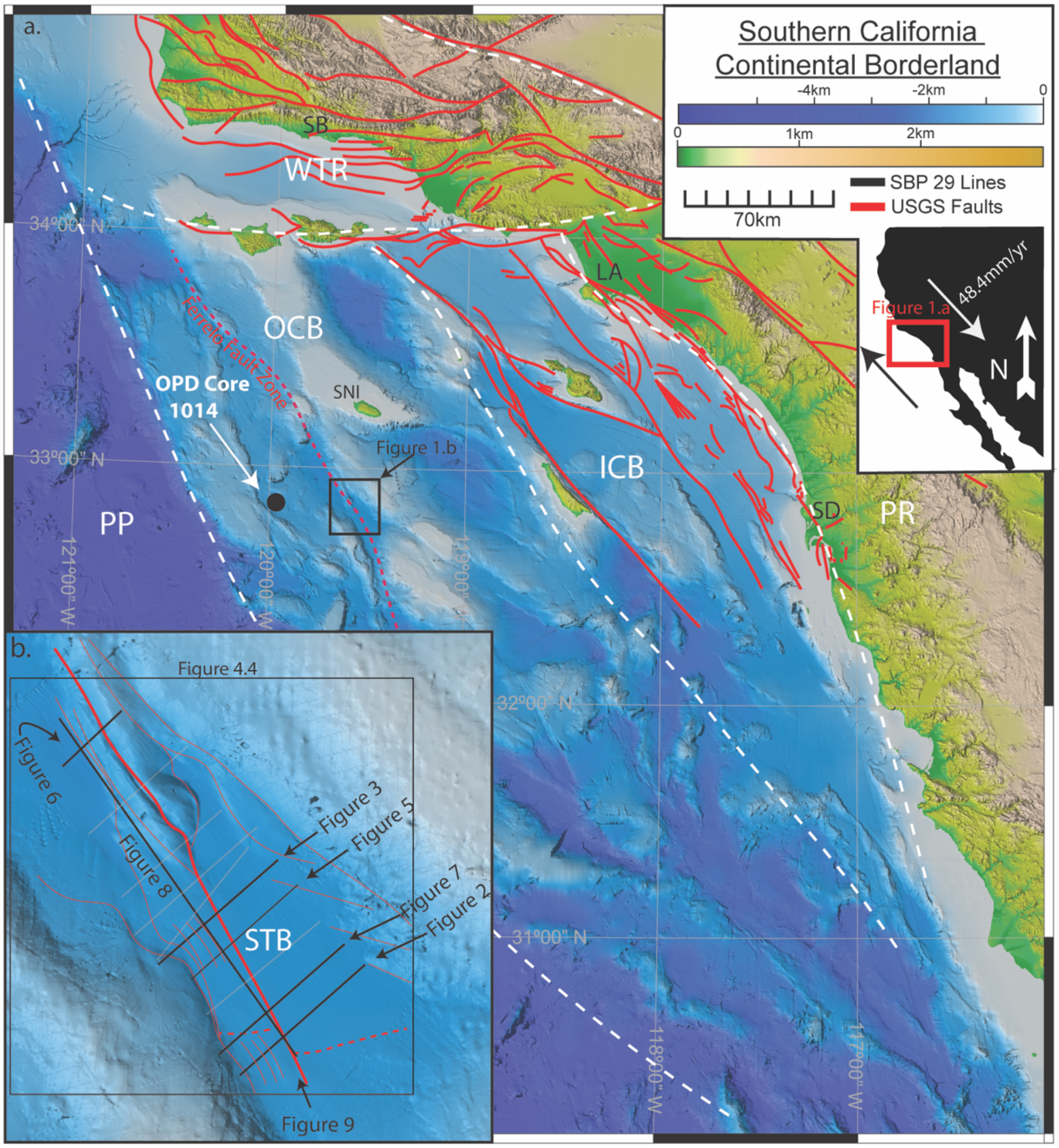

Figure 4.1 Topobathymetric map of the California Continental Borderland (CCB).

The active USGS Quaternary faults (solid red lines), San Diego (SD) Los Angeles (LA) and Santa Barbra (SB) are highlighted for reference with black text. Dashed white lines separate the Western Transverse Range (WTR), the Pacific Plate (PP), The Peninsular Range (PR), The Inner California Borderland (ICB), and the Outer California Borderland (OCB), the significant tectonic regions of the CCB. Location of ODP core 1014 is denoted by a solid black circle, southwest of San Nicholas Island (SNI). Figure 4.1.b Active deformation (solid red lines, the heavy red line is the "Ferrelo Fault") and inactive deformation (dashed red lines) identified from this survey, black lines are SBP 29 profiles shown herein, and grey are lines profiles collected during this survey.

## 4.2.0 Introduction

Together onshore Southern California and its offshore component the California Continental Borderland (CCB), accommodate much of the 48.4 mm/yr of active dextral strain between the Pacific and North American (PNA) Plates (Figure 4.1) (Platt and Becker, 2010). How and where these 48.4 mm/yr of strain are accommodated across this diffuse boundary is an active field of research. Active faults within the Inner California Borderland (ICB) and onshore Southern California through the southern Basin and Range geodetically account for ~42 mm/yr of the total plate motion (Platt and Becker, 2010; Walton et al., 2020). Strain accommodated east of the basin and range accounts for ~5% (~2.5 mm/yr) of the total PNA strain (Kreemer et al., 2010). Therefore, ~4 mm/yr of strain is still unaccounted for and is likely accommodated within Outer California Borderland (OCB), a relatively under surveyed region in this diffuse plate boundary.

Transpressional features associated with active deformation have been observed within the OCB (Gorsline et al., 1968; Legg et al., 2015). The Ferrelo Fault Zone (FFZ), formerly referred to as the Santa Rosa-Cortez Ridge Fault Zone (Hornafius et al., 1986; Crouch and Suppe, 1993), being one such feature, has been identified as an active fault zone by Legg et al.(2015) using multibeam and legacy multichannel seismic data. Despite the observations of

Figure 4.2 Comparison lines 2.A. Kongsberg SBP 29 and 2.B. Knudsen SBP 4 kHz.

(See Figure 1.b for location). Both systems image the same faulting and folded features as they were collected consecutively along the same transect. Insets 2.1 and 2.2 are of the Kongsberg and Knudsen (flipped vertically) systems, respectively, for direct quality comparison of sub-bottom reflectors. Insets 2.a, b, c & d further illustrate the resolvability difference between the two systems, dashed grey lines are 1-meter spacing. Line drawing on top of 1A shows the location of interpreted deformation, the Western Basin Bounding Fault (WBBF), the Ferrelo Fault (FF), the green False Fault Artifact (FFA), and the Eastern Basin Bounding Fault (EBBF), as well as Antithetic and Synthetic Faulting (AF & SF).

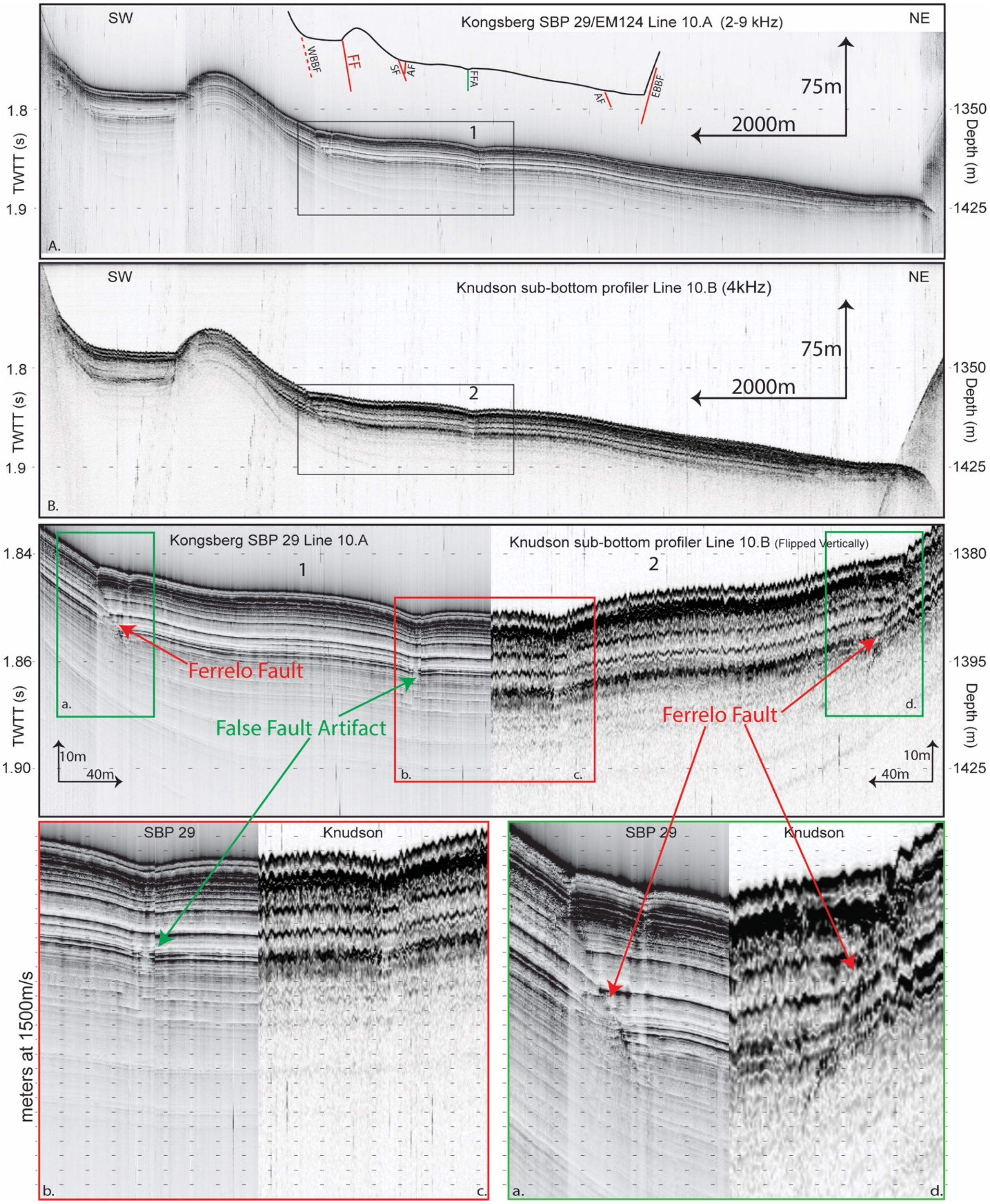
SW
Kongsberg SBP 29/EM124 Line 10.A (2-9 kHz)
NE
WBBF
FF
SF
AF
FFA
AF
EBBF
75m
2000m
1
1.8
1.9
TWTT (s)
1350
1425
Depth (m)
A.
SW
Knudson sub-bottom profiler Line 10.B (4kHz)
NE
75m
2000m
2
1.8
1.9
TWTT (s)
1350
1425
Depth (m)
B.
Kongsberg SBP 29 Line 10.A
Knudson sub-bottom profiler Line 10.B (Flipped Vertically)
1
2
1.84
1.86
1.90
TWTT (s)
1380
1395
1425
Depth (m)
Ferrelo Fault
False Fault Artifact
Ferrelo Fault
a.
b.
c.
d.
10m
40m
10m
40m
SBP 29
Knudson
meters at 1500m/s
b.
c.
SBP 29
Knudson
a.
d.

Legg et al. (2015), the FFZ is not in the USGS Quaternary fault database (U.S. Geological Survey). Updates in 2010 to the Uniform California Earthquake Rupture Forecast (UCERF) -3 model, specifically the addition of the offshore ICB faults (Figure 4.1), resulted in San Diego having the most significant hazard factor increase for all National Earthquake Hazard Reduction Program locations used in the updated model (Field et al., 2014). Future updates to the UCERF model that consider an active FFZ could similarly impact the hazard factor for San Diego and the greater Southern California region.

In June 2021, the R/V *Sally Ride* was fitted with Kongsberg's Sub-Bottom Profiler (SBP) 29 and an upgraded EM 124 multibeam system. During the R/V *Sally Ride's* 2021 sonar commissioning cruise (SR2104), while transiting from San Francisco to San Diego, the science objective was to operationally test and calibrate these new systems and survey opportunistic sites of interest to highlight the new system's capabilities. Here we present novel, high-resolution sub-bottom data from the OCB within the South Tanner Basin (STB), providing strong evidence of active faulting along the FFZ that highlights the increase in data quality of the Kongsberg SBP 29 system (Figures 4.1, 4.2 & 4.3).

## 4.3.0 Background

The CCB represents an extended and translated margin that has recorded ~30 My of deformation, as the margin transitioned from that of subduction to one of dextral transtension (Atwater, 1970; Hornafius et al., 1986; Crouch and Suppe, 1993; Nicholson et al., 1994; Bohannon and Parsons, 1995; Bohannon and Geist, 1998). This transition resulted from the Pacific-Farallon spreading ridge contacting the North American Plate, halting subduction, and ridge activity. Without active subduction or active spreading, far-field forces from Pacific Plate

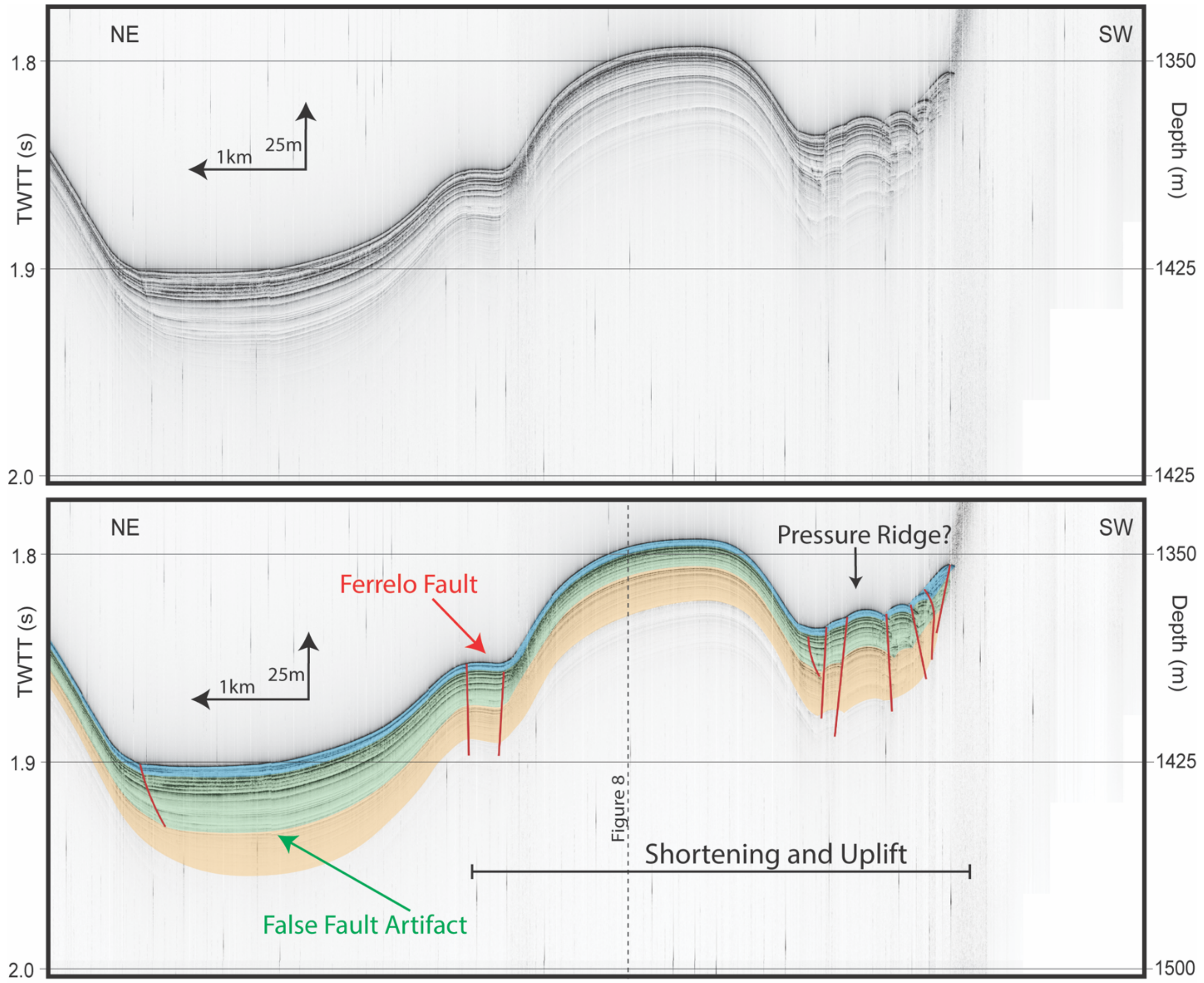

Figure 4.3 Uninterpreted (top) and interpreted (bottom) SBP 29 profile.

SBP 29 profile (see Figure 4.1.b for location) image a large anticline in the center of the profile, which separates deformation and offset of the seafloor to the west from the less active portion of the basin to the east. The vertical dashed line is the location of the cross line presented in Figure 4.8. Colored units represent the three packages mapped throughout the survey area; red lines represent interpreted faults.

subduction to the NW extended and translated the relic subduction forearc through basal shear. This initial extension marks the first phase of CCB deformation, which resulted in the >90º clockwise rotation of the Western Transverse Range (WTR). The rotation of the WTR resulted in the large-scale unroofing and exhumation of the subduction-related metamorphic complex known as the Catalina Schist Belt, which defines the basement rock of the ICB. In contrast, the

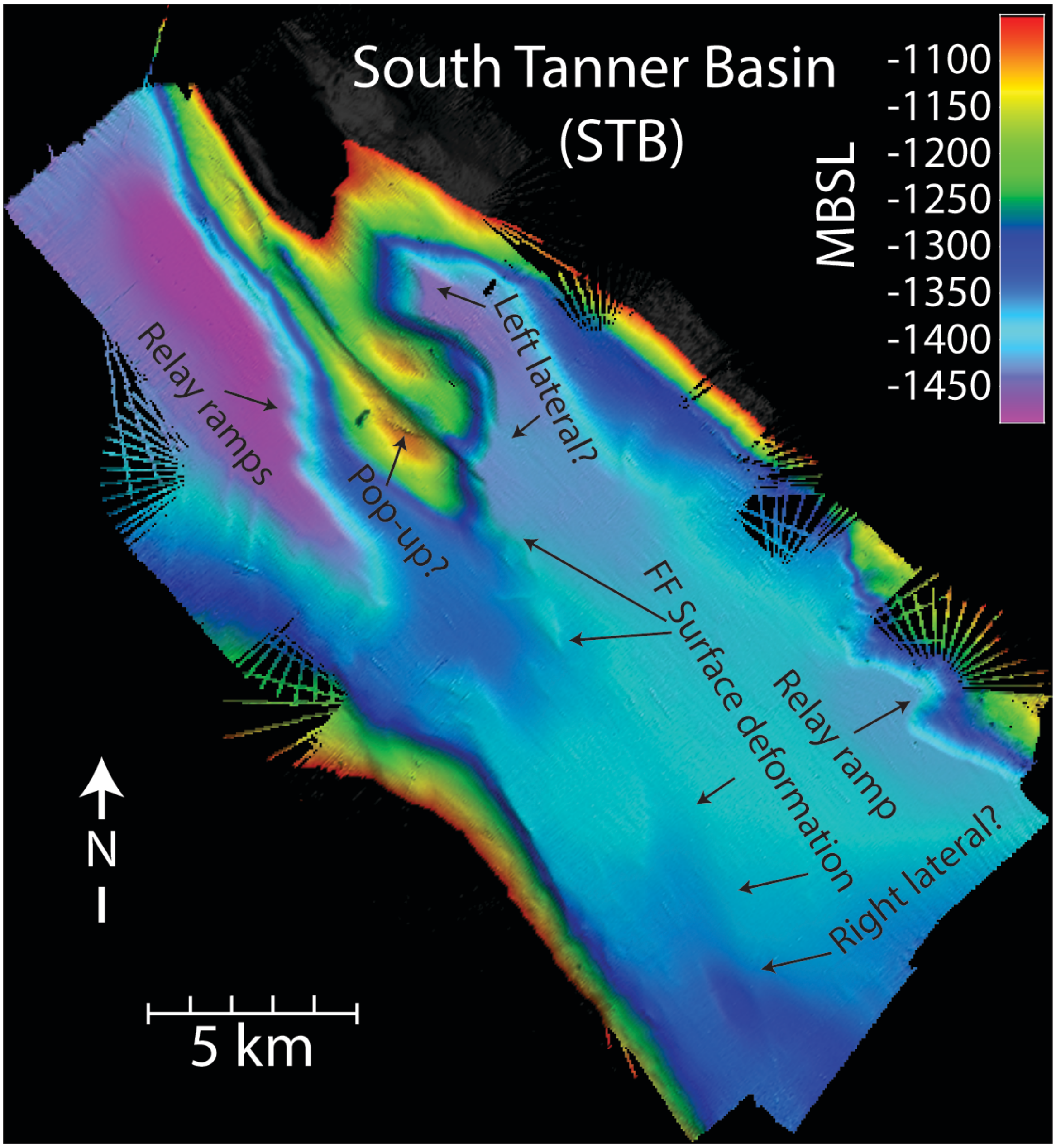

Figure 4.4 Gridded (50m cell) multibeam data collected during SR2104. See Figure 4.1.b for location

OCB, which is analogues to the Great Valley Sequence of Central California (Bohannon and Geist, 1998) is thought to have not been subjected to the same rotational forces as the WTR, because there was no hinge point to rotate around, as tectonic blocks outboard of the WTR/ICB were already moving NW (Nicholson et al., 1994).

Inherited structures from the first phases of CCB extension make up much of the observed morphology, which is has been characterized by numerous NW-SE trending basins bounded by ridges and faults (Figure 4.1). During the second deformation phase, starting ~15 Ma (Bohannon and Geist, 1998), and still active today, dextral PNA plate strain is accommodated along the many through-going ICB faults. (Platt and Becker, 2010; Walton et al., 2020). Geologic and geodetic observations suggest the ICB is currently accommodating ~8mm/y of right-lateral slip, ~15% of the total PNA plate strain. Nevertheless, to date, there are no measured slip rates for the OCB, despite observations of NW-SE trending active transpressional fault lineations such as the FFZ (Legg et al., 2015).

**The Kongsberg SBP 29 integrated EM 124 system** (https://www.kongsberg.com/maritime/products/ocean-science/mapping-systems/sub-bottom-profilers2/sub-bottom-profiler-sbp29/) marks a significant advancement for the marine geoscience community, as it is a sub-bottom profiler that can direct a narrow 3° transmit beam forward and aft ~10° as well as ~15° port and starboard. This variability in the SBP 29's transmit and receive angles allows the system operator to record a more accurate specular return signal by facilitating a more orthogonal ray path to the sediment-water interface and or targeted sub-surface reflector. In addition, the wide bandwidth 2-9 kHz narrow beam system offers improved penetration, signal to noise, and resolution over other systems. The user can select the desired bandwidth between 2 kHz and 9 kHz, as well as the preferred pulse form, CHIRP (up or down), continuous wave pulse, or Ricker. The upgraded burst mode of the Kongsberg SBP-29, transmits several pulses before the first pulse is returned, enables high sample rates even while surveying in full ocean depths.

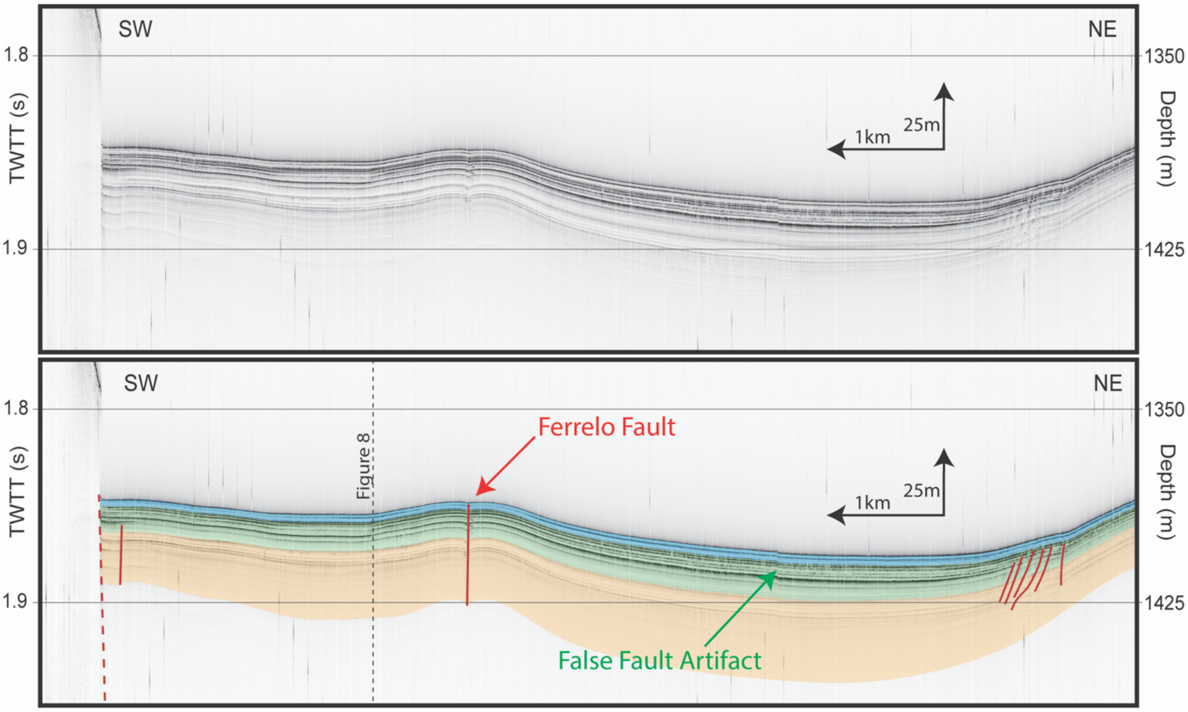

Figure 4.5 Uninterpreted (top) and interpreted (bottom) SBP 29 profile.

SBP 29 profile (see figure 4.1.b for location). Colored units represent the three packages mapped throughout our survey area; red lines represent interpreted faults.

## 4.4.0 Methods

In July 2021, ~135 km of CHIRP sub-bottom and multibeam data were collected along the FFZ within the STB (Figure 4.1) using the R/V *Sally Ride's* new Kongsberg SBP 29 and EM124 systems (Figure 4.4); our aim was to test and characterize the newly installed sonar complement. An additional 9.5 km of Knudsen 4 kHz sub-bottom profiling data were collected over an already surveyed SBP 29 line for direct comparison (Figure 4.2). SBP 29 survey parameters during data collection were as follows, linear CHIRP up 2 to 9 kHz, pulse length 80 ms, and burst mode enabled. Automatic slope correction was also enabled, meaning the SBP 29 system automatically adjusted the direction of the transmit and receive beams, providing an increase in the specular return to scatter ratio over other “broader” beam, non-steerable sub-bottom systems (Figure 4.2). Data were collected while surveying at ~8 knots, and were de-heaved, match filtered, and recorded in Raw (topas), and SEG formats. SGY data from the Knudsen 4 kHz SBP were recorded after being de-heaved by the Knudsen operator system, though it was not as effective as the Kongsberg SBP 29 (Figure 4.2). Both SEG and SGY data were processed using Sioseis (Henkart, 2003) and interpreted using IHS Kingdom Suite and QPS Fledermaus software packages. No post-processing steps such as bandpass filters, time varying gain, etc., were applied to any sub-bottom data. Knudsen and Kongsberg data presented (Figure 4.2) were processed using the same data amplification variables within the post-processing workflow. Further post-processing steps may improve the Knudsen data quality; however, we wished to directly compare the respective systems’ data quality, unbiased by ancillary post-processing. Multibeam data were processed using QPS Qimera and interpreted in Fledermaus. Bathymetric data gridded at (50 m) and nested with existing topobathymetric surfaces (National Geophysical Data Center, 2012) using Oasis Montaj (Figure 4.1. b & 4.1.c). All sub-bottom conversions between time and depth use a nominal water velocity of 1500m/s.

## 4.5.0 Results

Both sub-bottom systems image deformation; however, the Kongsberg SBP 29 system resolves decimeter subsurface density contrasts not resolved with the Knudsen system (Figures 4.2). Figures 4.2. A and 4. 2. B, are direct comparison line(s) between the two sub-bottom

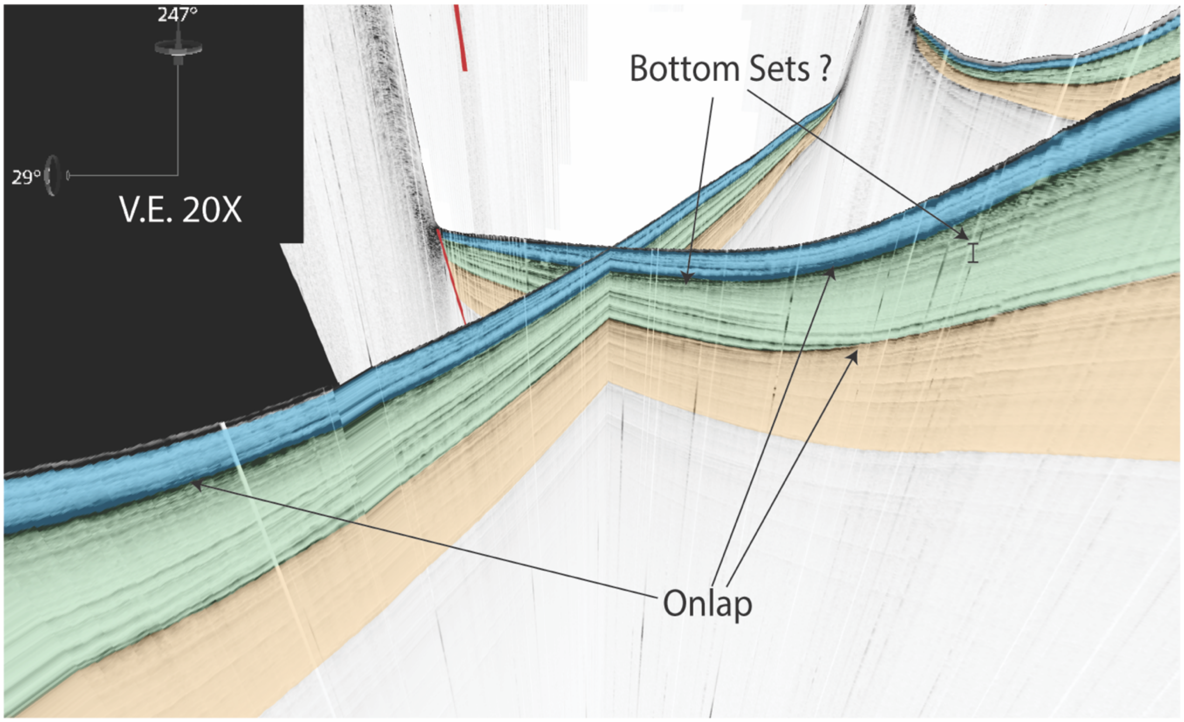

Figure 4.6 Oblique view of a fence diagram.

Looking E 23°S (see figure 4.1.b for location) with a Vertical Exaggeration (VE) of 20X images in 2.5D, three units separated by two packages exhibiting a marked downward shift in onlap.

systems transecting the STB, and were collected consecutively, each system respectively optimized for data quality. The striking increase in data quality can be observed in comparison Figures 4. 2. A. 1. a / 4. 2. B. 2. c and 4. 2. A. 1. b/ 4. 2. B. 2. d, as up to ten distinguishable reflectors per meter are observed within the SBP 29 profile, compared to the two to three reflectors per meter within the Knudsen profile. Both systems applied a de-heave filter before recording SGY/SEG data. Despite the swell direction being orthogonal to ship track for the collection of both 4. 2. A and 4. 2. B, there is a noticeable difference in the effectiveness of the respective systems de-heave filter, which ultimately influences data quality. Seven of the 13 seismic profiles collected along the FFZ are presented and described using a combination of structural and sequence stratigraphic terminologies.

Three separate sediment packages are imaged and are separated by two basin-wide reflectors that are onlapped upon (Figures 4.6, & 4.8). The blue package has an average thickness of 3-5m, including the basal package that onlaps the underlying reflector (Figure 4.6). The green package is separated from the blue package by a strong, high amplitude reflector. The bottom sets of the green package upslope of the tie line are not imaged (Figure 4.6), and it is unclear if they follow conformable association with the high amplitude reflector above it, separating the blue and green packages (Figure 4.6). Like the blue package, the base of the green

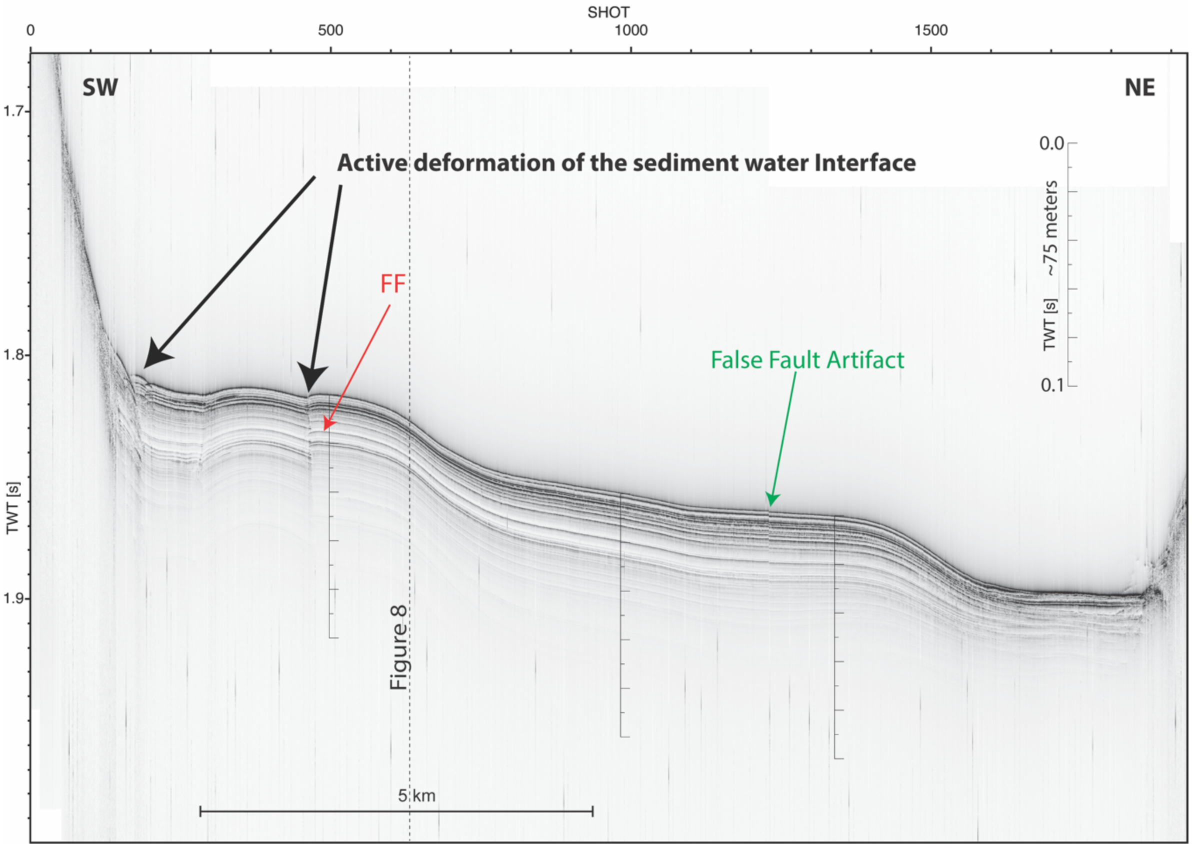

Figure 4.7 Active deformation across the South Tanner Basin.

See Figure 4.1.b for location

package is marked by a downward shift in onlap on the lower basin-wide reflector (Figure 4.6). The thickness of the green package ranges between 10m and 21m (Figures 4.3, 4.5, 4.6, 4.7 & 4.8). The base of the orange unit shows the maximum depth of acoustic penetration imaged within the STB. Sub-bottom reflectors within the main morphologic high, separating the STB from the north Tanner Basin (Figures 4.1, 4.4 & 4.8) were not imaged; however, the sediments are imaged onlapping this structure.

Within the survey area, features associated with deformation are observed along the seafloor (Figure 4.2, 4.3, 4.4, 4.5, 4.6, 4.7 & 4.8) and within the top 100 m of sediment. The primary fault trace (heavy red line in figure 4.1.b) herein referred to as the Ferrelo Fault (FF) (Figures 4.4) has observably offset seafloor structures in the 50m bathymetric grid, as well as the sub-bottom data (Figures 4.2, 4.3, 4.4, 4.5, 4.6, 4.7 & 4.8). The FF within the STB generally trends N20°W and dips ~20° to the NE (Figures 4.8 & 4.9). Additional data are required to tease out the sense of motion along the FF and image splays that might accommodate some of the strain (Figure 4.4). Despite there being no definitive sense of motion based on the morphology along the FF, the varying thicknesses of the blue, green, and orange packages on either side of the FF (Figures 4.6 & 4.8) could indicate a strike-slip component to the FF. The dip-slip component of the FF appears to vary along its trace. In the southern part of the STB, an overthrust anticlinal fold is observed along the FF, with almost ~20m of throw (Figure 4.2). Following the trace of the FF north, the thrusting component diminishes and appears to invert to a normal component closer to the large morphologic high (Figure 4.2, 4.3, 4.5, 4.6, 4.7 & 4.8).

Antithetic and synthetic deformation associated with the FF is also observed throughout the data. Due to the high vertical resolution of the data, the sediment-water interface is clearly deformed and, in some cases, offset (Figure 4.1, 4.2.A, 4.3, 4.4, 4.5, 4.6, 4.7 & 4.8). The deformation west of the FF within the STB has undergone significant NE-SW shortening (Figure 4.3 &4.7), which has resulted in a hummocky sediment-water interface. Within the STB bathymetry, east of the FF, there is a 1.5km right stepover that dissects the westward dipping antithetic basin bounding fault (Figure 4.4) Smaller 0.2-0.3km right stepovers are also observed in the bathymetry west of the pop-up structure, along with off-axis faulting west of the FF. Features that look like vertical faults are also observed in the SBP 29 data; however, these features are artifacts (see Figures 4.2.A, 4.3, 4.5, 4.6, 4.7 & 4.8 interpretations for some of the identified false fault artifacts) that will be described in detail in the following discussion.

## 4.6.0 Discussion

The Kongsberg SBP 29 system provides the highest resolution hull-mounted sub-bottom data of any UNOLS Ocean Class survey vessel, all while surveying at twice the usual survey speeds (~9knots). One issue we would like to bring to the attention of future SBP 29 users and interpreters is the false fault artifact (Figure 4.2, 4.3, 4.5, 4.7 & 4.8). The false fault artifact is produced by two operations of the SBP 29 System coinciding. When the SBP 29 system operates in burst mode, the ping rate is determined by water depth. A slight pause in sampling occurs when a change to the ping rate is required. The short hiatus in sampling combined with the updated ping rate causes a vertical artifact, resulting in an artificial discontinuity of reflectors. This vertical artifact separates continuous reflectors; however, the reflectors may have different apparent vertical rates of change because the sample interval has changed. This artifact expresses itself as a false fault. It has the characteristics of divergent layers separated by apparent offset to

Figure 4.8 Uninterpreted (top) and interpreted (bottom) SBP 29 profile.

Profile transecting the survey area (see figure 4.1.b for location). At around shot 450, there is a data gap, and shot 3400, there was a short period when the ping rate was lowered; both features are artifacts not to be interpreted. Figure 4.5 crosses this profile within the time when there was a decreased sample rate, and therefore is not noted within this profile. The colored units represent the three separate packages separated by onlap mapped throughout our survey area, and red lines represent interpreted faults. The southern part of this profile images an anticline bounded to the north by a fault, down to the north orientation, and antithetic and synthetic deformation to the south. Insets 4.5.a and 4.5.b highlight important onlap surfaces.

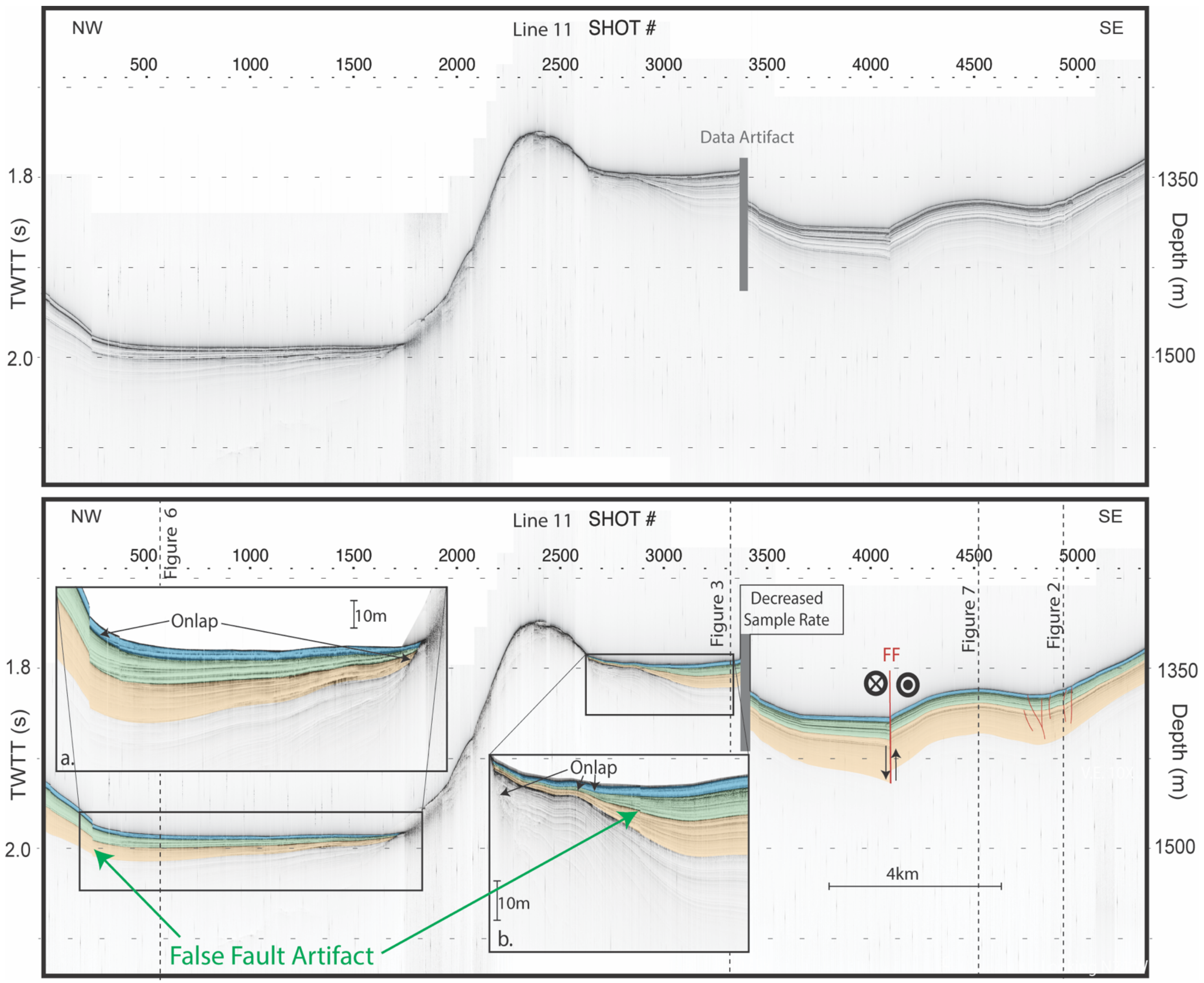
NW
Line 11 SHOT #
SE
500
1000
1500
2000
2500
3000
3500
4000
4500
5000
Data Artifact
1.8
2.0
TWTT (s)
1350
1500
Depth (m)
Figure 6
Figure 3
Figure 7
Figure 2
Decreased Sample Rate
FF
⊗ ⊙
Onlap
10m
a.
b.
4km
False Fault Artifact

functions, users may misinterpret the false fault artifact as active deformation where none exists. We hope the description mentioned above allows the reader to interpret the false fault artifacts for themselves; however, future updates to the Kongsberg SBP-29 acquisition software will document flag false fault artifacts in the meta data, so they are not interpreted.

Stratal architecture observed along continental margins is governed by the interplay of sediment flux and base-level change (Posamentier et al., 1992). Conformable successions of sediment are bounded above and below by unconformities, and their respective correlative conformity together, referred to as sequence boundaries (Christie-Blick, 1991; Christie-Blick and Driscoll, 1995). Downward shifts in onlap below the former rollover are distinctive features in seismic reflection profiles (Figures 4.6 & 4.8) and are typically interpreted as the landward termination of a sequence boundary following a base-level fall (Figures 4.6 & 4.8).

Turbidites represent a secondary sediment transport and depositional process, where unstable shelf and slope sediments are liberated and transported downslope through turbulent flow. During this downslope, fluid-supported transport, sediments are sorted and deposited, filling bathymetric lows and onlapping preexisting surfaces (Figures 4.6 & 4.8). Turbidites deposited within marine and lacustrine basins result from slope instability; in most cases, triggered by base-level change (Shanmugam and Moiola, 1982; Zavala and Arcuri, 2016). Exposing continental shelves to wave base erosion and currents within the mixed zone, as well as clathrate destabilization, are several of the many ways base-level change can trigger turbidites.

Within the CCB, seismicity is not uncommon. Many magnitudes 5 and 6 earthquakes have been recorded (Legg et al., 2015) within this seismically active region. Seismically induced turbidites and turbidites triggered by over-steepening are depositional processes that fall outside

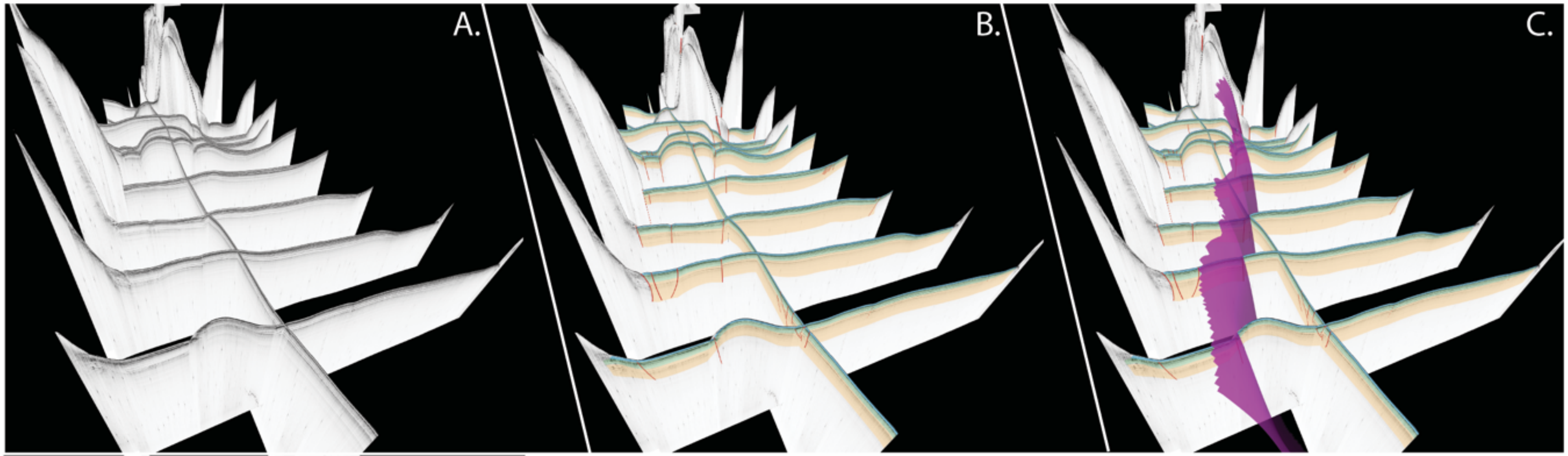

Figure 4.9 Fence diagram of the Ferrelo Fault.

Oblique view looking N 24°W with a Vertical Exaggeration (VE) of 10X. 6.A, uninterpreted SBP 29 Data. 6.B interpreted SBP 29 Data with Identified faulting highlighted in red and identified sediment units, respectively color-coded. 6.C interpreted SBP 29 Data with Identified deformation highlighted in red and identified sediment units color-coded. The purple surface represents Ferrelo Fault, which generally trends N20°W and has a dip of ~20° to the NE.

the generally agreed upon base-level controlled stratal architecture and are important indicators of regional seismic hazard (St.-Onge et al., 2004; Goldfinger et al., 2012; Maloney et al., 2013). For brevity, we will refer to both seismically induced turbidites and turbidites generated from tectonically over steepened slopes as seismically induced turbidites as they are both the product of active tectonic processes. It must be noted that changes to base level and or sediment supply may prime the source zone for failure; however, they are not the ultimate cause of seismically induced turbidites. It is difficult to distinguish seismically induced turbidites from non-seismically induced turbidites using seismic reflection profiles alone, as there are no distinguishable characteristics for either case recorded in a seismic profile of the resultant deposit. Other contextual evidence is required to support such an interpretation, such as proximity to "active" deformation, Relative Sea Level (RSL) changes, sediment rates and sediment cores.

Quaternary sediment accumulation rates for the Tanner Basin (Figure 4.1.A) are between 7.9 - 12 cm/ky, derived from Ocean Drilling Program core 1014 Leg 167 (Lyle et al., 1996; Heider et al., 2001), which would place the timing of the observed downward shifts in onlap (Figures 4.6 & 4.8) to Marine Isotope Stage (MIS) 5. A to MIS 2 base-level change. When considering regional RSL fluctuations (Muhs et al., 2012), distance to respective exposed shelves (Figure 4.1), and local tectonics (Legg et al., 2015), it is much more likely these downward shifts in onlap are seismically induced turbidites and are paleoseismic proxies of strong ground motion that has occurred within the OCB. Ultimately sediment cores will be required to sample these sediments and contextualize what processes these downward shifts in onlap have recorded.

Interpretations of active faults typically imply that surface displacement has occurred within the last 11,000 years, following the Alquist-Priolo Earthquake Fault Zoning Act of 1972.

Given the sediment accumulation rates with thin the Tanner Basin (~10 ± 2 cm/ky, Lyle et al., 1996; Heider et al., 2001) and the true decimeter resolution of the SBP 29 data, we can confidently report that the FF has experienced surface rupture within the last 1,000 years (Figures 4.1, 4.2.A.1.a, 4.3, 4.5, 4.6, 4.7, 4.8 & 4.9) and is likely accommodating some component of aseismic creep. Because 1,000 years of sedimentation would be resolvable with the SBP 29 system, the absence of post rupture sedimentation drape provides a high degree of confidence in our interpretation of FF being active within the last 1,000yr. These observations are consistent with those of Legg et al. (2015) and together should provide more than enough evidence to include the FF in the Qfault (USGS) database, and consequently, future probabilistic seismic hazard assessments for the Southern California region (Field et al., 2014).

Evidence of active deformation is observed throughout the STB and is most apparent where the sediment-water interface is deformed and or offset. A critical observation is a change in the mode of deformation with respect to the FF's dip-slip component along strike. In the southern area of the STB, the FF is experiencing transpression (Figures 4.2, 4.7 & 4.8), with what appears to be a dextral component (Figure 4.4). Following the FF north, we see the transpressional dip-slip component diminish and transition to transtension (Figures 4.3 & 4.5). Within the bathymetry of the STB (Figure 4.4), we observe multiple right stepovers along the basin-bounding faults, which are morphologically consistent with relay ramps. Relay ramps are essentially transfer zones along a segmented normal fault, where lateral strain is transferred and accommodated by ramp/block rotation and extension, explained by Peacock and Sanderson (1994). West of the FF, we also observe off-axis deformation that has resulted in a hummocky sediment-water interface. This deformation has the structure of a pressure ridge, which is illustrated in Figure 1 of Donnelly and Melton (1995). The pressure ridge west of the main FF offsets of the sediment-water interface in multiple locations, as it accommodates off-axis strain from the FF (Figures 4.3 & 4.7).

## 4.7.0 Conclusions

Observations from the new SBP 29/EM124 data, collected and presented herein, suggest the Ferrelo Fault has been active within the last 1,000 yrs and is accommodating some component of the Pacific North American Plate strain. In addition, we have identified three sediment packages that are separated by downward shifts in onlap, which are likely proxies for strong ground motion that has occurred within the OCB. Future investigations into the historic ground motion within the California Continental Borderland should target and sample these onlapping sediments as they may provide context into the regions paleoseismic history as well as the regions seismic hazard. Further investigation is needed to understand better the complex kinematics of the South Tanner Basin, the active Ferrelo Fault Zone, and Outer California Borderland as a whole.

## 4.8.0 Acknowledgements

Data used for this research was collected during Chief Scientist Lee Ellett’s R/V Sally Ride Sonar commissioning cruise (SR2104), and the authors are grateful for the opportunity to have gained experience with this next generation sub-bottom profiler. National Science Foundation Grants (1827415, 1823600) and Office of Naval Research Grants (N00014-16-1-2745, N00014-19-1-2652, N00014-19-1-2754) funded the new sonar suite, its installation, and the sonar commissioning cruise on the R/V Sally Ride.

The authors would like to thank the R/V Sally Rides crew and the shipboard science party, Mary Huey, Dan Orange, Charles Holland, Anand Hiroji, Olaoluwa Oderinde, Cody Henderson, Kevin Jerram, Michael Smith, Andrew Naslund, Keith Schadle and Kolby Pedrie. We would also like to thank Kongsberg Maritime representatives Aaron Berry and Jacquelyn Mart for their support and training while underway. Lastly, the authors would like to acknowledge the thoughtful discussion and valuable comments from Jillian Maloney which greatly improved this manuscript.

Chapter 4 is being prepared for publication in: Derosier, B.J., Driscoll, N.W., In Prep. New High-Resolution Sub-bottom Profiler Resolves Active Deformation Within the Outer California Borderland. *Geophysical Research Letters.* The author of the dissertation was the primary researcher and author of this publication. Co-authors contributed to data collection and multibeam processing presented within this chapter; however, they have not reviewed and or approved of the manuscript in its present form.

# Chapter 5

# Shallow Distributed Faulting in the Imperial Valley

## 5.1.0 Abstract

In the tectonically complex Imperial Valley, California, the Imperial Fault (IF) is often considered the region's primary fault; however, its strain partitioning and interactions with other faults are not well-understood. Despite inferred evidence of other major faults (e.g., seismicity), it is difficult to obtain a holistic view of this system due to anthropogenic surface modifications. To better define the structural configuration of the plate boundary strain in this region, we collected high-resolution shallow seismic imaging data in the All-American Canal, crossing the Imperial, Dixieland, and Michoacán Faults (MF). These data image shallow (<25m) structures on and near the mapped trace of the IF, as well as the Michoacán Fault and adjacent stepover; integrating our data with nearby terrestrial cores provides age constraints on IF deformation. These data suggest that the MF, unmapped in the United States, is active, and likely produces dynamic or off-fault deformation within its stepover to the Dixieland Fault. Together, these data support more strain partitioning than previously documented in this region.

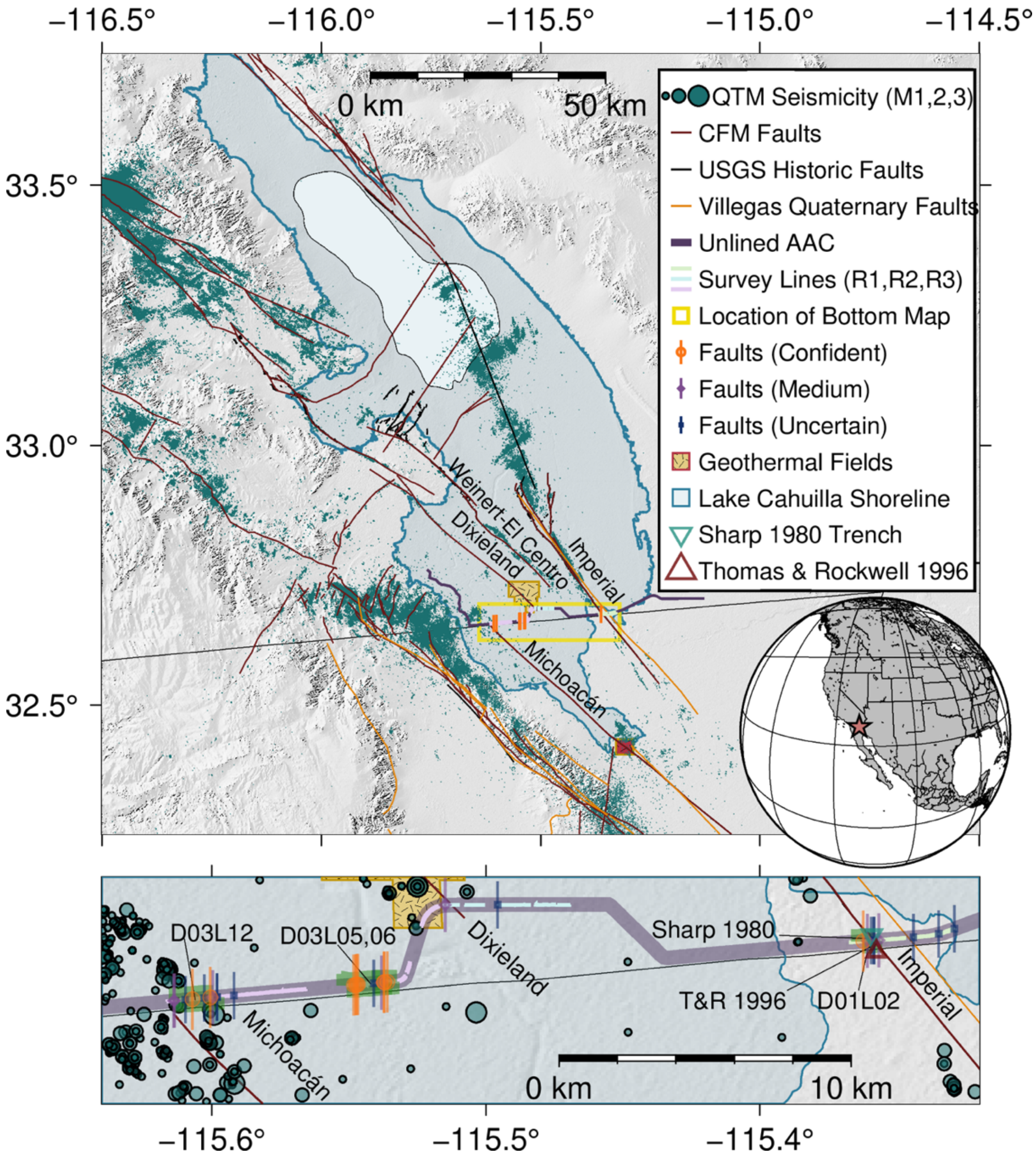

Figure 5.1 Imperial Valley region.

Top: Red star on globe indicates map location. Southern California Earthquake Center community fault model (SCEC CFM 5.3) faults (Plesch et al., 2020), US Geological Survey (USGS) historic faults (USGS, 2017), Mexico quaternary faults (Gonzalo et al., 2017), "Confident" mapped faults from this study, quake template matching (QTM) 9.5 standard deviation database seismicity (Ross et al., 2019), select geothermal fields (Heber, yellow; Cerro Prieto, red), unlined All American Canal (AAC), trenches of Sharp (1980) and Thomas & Rockwell (1996)( TR 1996) and the ancient Lake Cahuilla footprint (Buckles et al., 2002) are described in legend. Yellow box indicates the location of the bottom map. Bottom: Survey region. In addition to main map features, this study's survey lines are shown, as well as "medium" and "uncertain" mapped faults in this study. Earthquakes scaled by magnitude (legend). Seismic lines presented are highlighted in green with labels.

## 5.2.0 Introduction

North of the coalescence between the transtensional Gulf of California and the Pacific-North American plate boundary, the Imperial Valley is a tectonically complex region (Larsen and Reilinger, 1991; Han et al., 2016). Strain is partitioned eastward into the Eastern California Shear Zone and subsequently north to the Walker Lane, an incipient Pacific/North American plate transform boundary (Dokka and Travis, 1990; Wesnousky, 2005). This leads to active fault evolution, interaction, and strain partitioning in the region (Crowell et al., 2013), important to

Figure 5.2 Photos of deployment.

A: The transducers on the chirp bottom. B: CHIRP frame. C: Buoyant pontoons to float the frame. D: Deploying the chirp from the northern canal bed. E: Towing the chirp from the southern bank with a towline; umbilical and second towline (right) towards northern bank and topside. GNSS receiver on frame mount, (red circle and arrow). F: Topside system setup.

understand for present-day fault interactions and seismic hazard, and to elucidate the history of this complex, segmented margin.

At the latitude of the US-Mexico border, the Imperial Fault (IF) is considered the major structure in the Pacific-North American plate boundary system (Figure 5.1), hosting two large recent earthquakes (1940 **M**7.0, 1979 **M**6.5, Trifunac and Brune, 1970; Archuleta, 1984). The Uniform California Earthquake Rupture Forecast version 3 (UCERF3, Field et al., 2014) hazard model attributes 30–40mm/yr of plate boundary slip to this fault. Geologic slip rates are much lower (15–20mm/yr, Thomas and Rockwell, 1996). Patterns of seismicity in the Imperial Valley suggest that several other inferred faults share the plate boundary strain with the IF, the Weinert-El Centro (WECF), Dixieland (DF), and Michoacán (MF) faults (Magistrale, 2002; González-Escobar et al., 2020). Seismicity lineaments indicate that the MF extends north of the border, accommodating some plate boundary slip, as do joint InSAR and GNSS studies which place slip on a structure 10-20km to the west of the IF (Lindsey and Fialko, 2016). Similarly, south of the border, geodetic data supports shared slip between the IF, MF, and faults of the Sierra Cucapah (Sandwell et al., 2016). Likewise, mechanical models (Dorsett et al., 2019a) found that the MF/Cerro Prieto (CP) fault is likely linked to the IF system, and faults such as the DF accommodate some of the IF’s strain, changing our understanding of fault interaction in the Imperial Valley.

Geomorphic evidence of faulting is, however, almost entirely obscured in the Imperial Valley due to anthropogenic activity and ancient Lake Cahuilla sediments, posing challenges in identifying suitable sites for geologic studies and paleoseismic trench campaigns. Although several trenches exist in the region (e.g., McNeilan et al., 1996; Jerrett, 2016; Wessel, 2016), the IF’s slip rate is not as well-constrained as other faults in Southern California. Without direct observations of shallow faulting, it is challenging to fully characterize these structures geologically.

## 5.3.0 Data

We address this insufficiency of observations with a novel study to constrain young (<5ka) deformation in the shallow subsurface. We used a traditionally marine subsurface imaging instrument in the All-American Canal (AAC, Figure 5.1), a large aqueduct that transports water from the Colorado River to the Imperial Valley. The AAC parallels the California/Mexico border near Calexico, CA, and directly crosses the IF, DF, and a proposed region of strain accommodation. With an acoustic compressed high-intensity radar pulse (CHIRP) instrument, we attribute shallow deformation to these structures, and further our understanding of the interaction of fault structures in the region. We towed the CHIRP from West to East through the AAC in a floating cage (Figure 5.2). We collected 27 seismic lines in three main regions: near the IF (5.1), DF (2), and the inferred trace of the MF (3, Figure 5.1). Lines are abbreviated as ACDXXLYY, with XX as the day and YY the line number. We approximate ages of the sediments with a sedimentation rate with calibrated $^{14}C$ dates from a nearby core (Rockwell and Klinger, 2013; S-Text).

## 5.4.0 Results

We characterize our interpretations as “confident”, “medium confident”, and “uncertain”. Intermittent striping from gas throughout the dataset prevents local data interpretation (Sahakian et al., 2016).

In Region 1 (IF), only line ACD01L02 shows clear data. We observe deformation of thick, strong reflectors at 15–25m depth assuming 1500m/s water velocity (Horizon 2, 5.4° dip), and less prominent reflectors beneath the canal bedforms, such as "Shallow IF" (Figure 5.3), with an apparent 3.4° dip to the west, intersected by the mapped traces of the IF (Rockwell and Klinger, 2013; Nicholson et al., 2020; Plesch et al., 2020). At ~0.4km distance, there are small discontinuities in this reflector ("uncertain"), with gas obfuscation to the east. At ~0.17km distance, we observe small offsets in reflectors (0.018–0.302s) such as Horizon 1, and at ~0.04km. Underlying strata fold in towards an inferred structure ("confident", Figure 5.3). Other lines in region 1 exhibit thick, bright, flat-lying reflectors at the same depth.

In region 2 (DF), we observe some shallow deformation and folding of reflectors above 10m depth; however, the reflectors are thinner and less continuous compared to region 1. Identifying surface offsets here is challenging due to high canal floor reflectivity. Multiples dominate >15m, obscuring deformation below ~10m. Most observable reflectors in this region are flat lying. The mapped trace of the DF intersects Day 2 Line 1 (ACD02L01, Figure S5, S6), but interpretations are not possible due to the strong prevalence of gas.

Clear offsets and deformed reflectors are observed in region 3 (MF) on lines ACD03L05, ACD03L06, ACD03L12 (Figure 5.4, S7), and ACD03L13 (Figures S8, S9). North of the mapped MF trace (ACD03L12), we observe clear offsets in reflectors (Horizon 1) with down-to-the-west vertical separation of ~4.5m. At ~1.1km distance, there is an abrupt transition between continuous and chaotic reflectors ("confident"). There is a prominent region of gas in the middle of this line, separating flat lying from dipping reflectors, likely due to a fault ("uncertain", ~0.9km distance). The "confident" fault interpreted at ~0.2km distance on ACD03L05 demonstrates reflector offset >1m. An adjacent fault warps reflectors, but their continuity is not sufficient to confidently describe an offset. The eastern portion of ACD03L05 shows folded reflectors, and the adjoining ACD03L06 shows divergence of reflectors, small offsets, and a

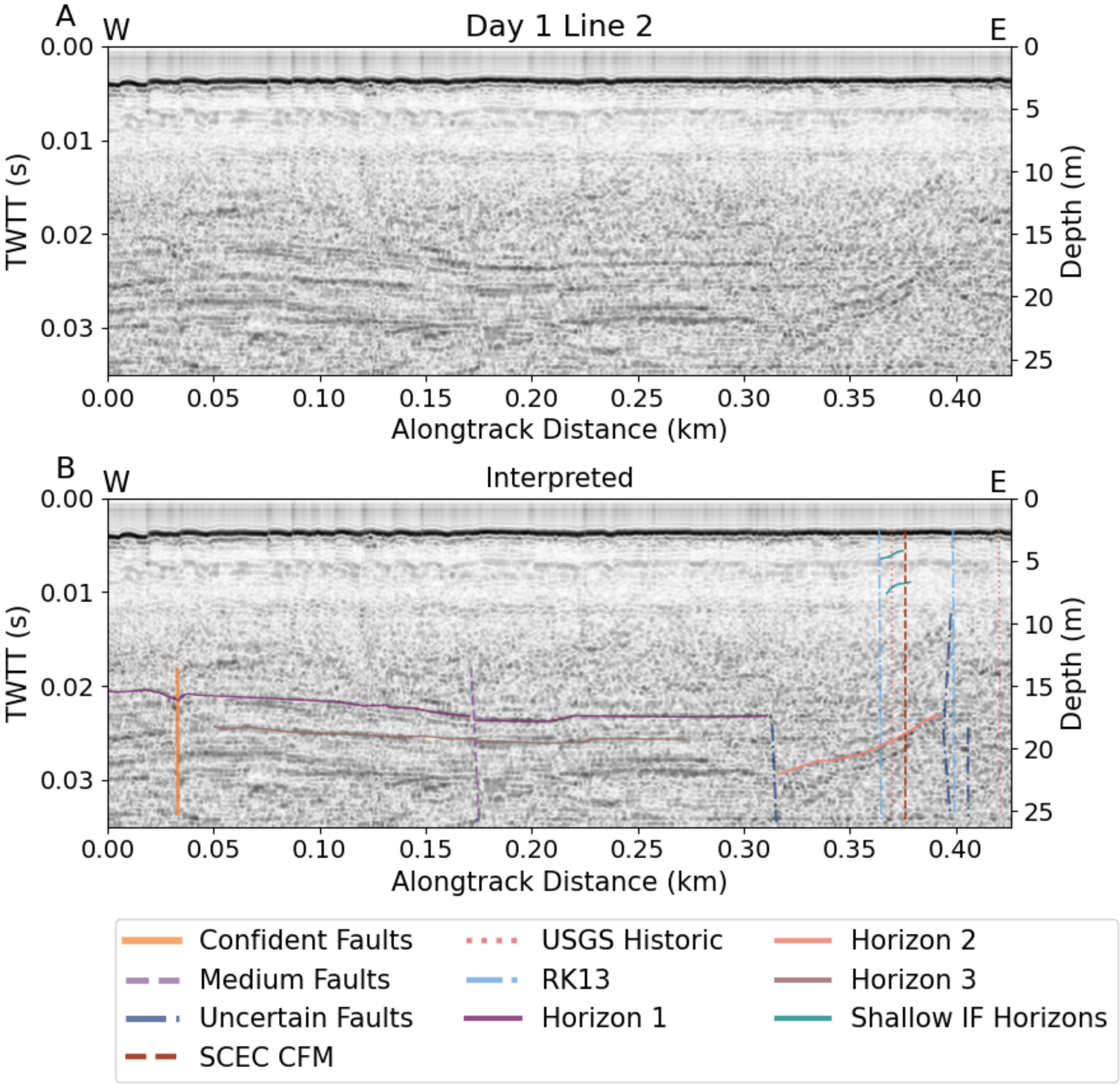

Figure 5.3 Data crossing the Imperial Fault (IF).

Day 1 Line 2 seismic line, showing deformation near the mapped trace of the IF. Two-way travel time (TWTT) on the left axis, and depth below instrument on the right axis. A: Uninterpreted seismic profile. B: Interpreted seismic profile. Faults from the Southern California Earthquake Center (SCEC) community fault model (CFM 5.3), U.S. Geological Survey (USGS) Historic faults, and Rockwell & Klinger (2013) (RK13) are shown, as well as interpretations from this study. Select horizons and their names are indicated in legend.

westward dip between two confidently mapped faults. Gas on line ACD03L13 occurs in the middle of the line, with reflectors dipping and thickening towards the center region of gas, potentially obscuring a structure responsible for this deformation ("uncertain").

## 5.5.0 Discussion

The deformation in region 1 coincides with the mapped IF trace, likely representing IF deformation from the 1940 and previous earthquakes. Both the deep and shallow strata surrounding the mapped fault trace exhibit an apparent southwestward dip, which increases slightly with depth. Consistent with syn-depositional faulting, this suggests a local, consistent sense of motion on the IF.

Obtaining a sedimentation rate here is fraught with uncertainties, but we aim to place highly approximate temporal constraints on subsurface deformation. The AAC is 1km south of a cone penetrometer (CPT) profile by Rockwell and Klinger (2019) yielding stratal relationships, with two cores within and adjacent to the IF. Both cores, located on a berm at 9m above sea level (1 m above the surrounding agricultural fields averaging 8 m elevation), sample several Holocene clay layers beneath interpreted ancient Lake Cahuilla Lake G deposits, with age control based on radiocarbon dating of mollusk shells, charcoal, and ostracods. The oldest sampled layer is ~16m below sea level. In our data just 1km to the south, the local canal water level from CHIRP-mounted GNSS is 8m above sea level and 3m below average land surface, suggesting that sedimentation should be consistent across this flat region.

With the cores, we estimate a rate of 4.6–19m/kyr (>10m depth), and an earlier rate of 3.6–5.7m/kyr (5-10m). We thus estimate Horizon 2-line ACD01L02 at ~0.03s TWTT (~17.5-22.5m beneath instrument, ~9.5-14.5m below sea level) to be ~1.9-3.6ka. See supplement for additional information. Most deformation we observe in ACD01L02 is likely occurring in Holocene sediments, and the deepest antiformal deformation at approximately 2km along track distance is older, likely Pleistocene in age. The apparent southwestward tilt on the eastern portion of the line at ~4-6m depth is likely <1.1ka in age and is similar to the southwestward tilted strata noted in nearby trench by Sharp (1980) but not by Thomas & Rockwell (1996) 75m to the south (Figure S10). This suggests that these structures may be produced by a local structural pressure ridge or pull-apart associated with a fault stepover. The fault we observe at ~0.17km distance does not deform reflectors above ~0.0125s TWTT, corresponding to <2.5ka,

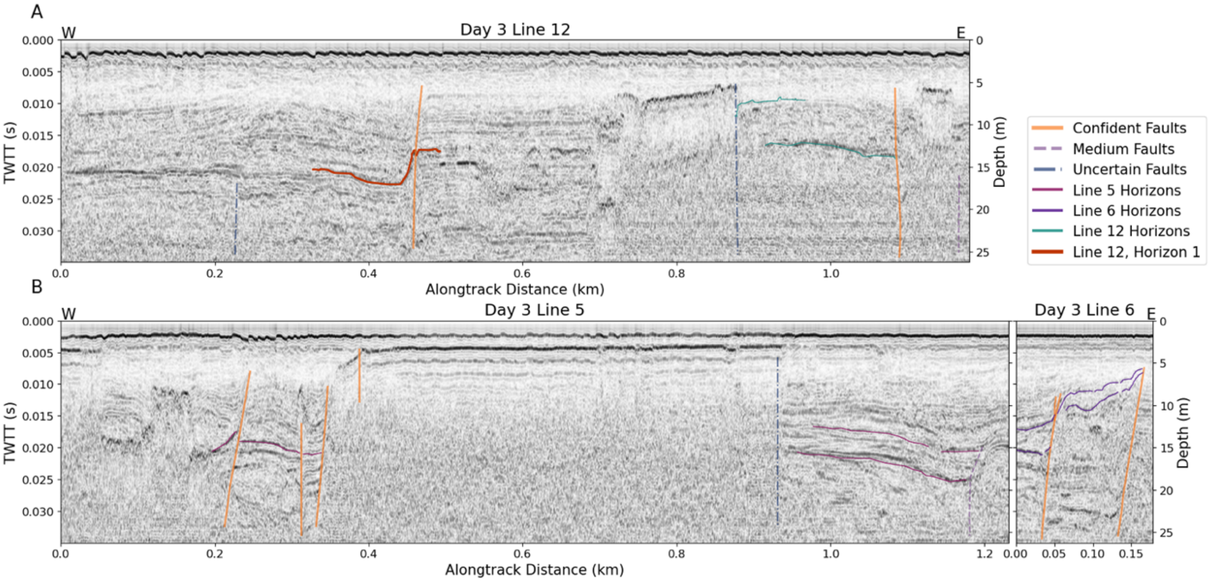

Figure 5.4 A: Profile Day 3 Line 12

Profile showing deformation and offset near the proposed Michoacán fault. Two-way travel time (TWTT) on the left axis, depth below instrument on the right axis. Line 12, Horizon 1 reflector shows ~4.5m of vertical offset next to a mapped fault. B: Day 3 Lines 5 and 6 (~15m apart) showing deformation between the Michoacán and Dixieland faults.

or lakes below Lake G (~2ka, Rockwell et al., 2011), which implies that there have been no coseismic offsets on this structure for at least the last 3-4 IF events. This agrees with an analysis of aerial imagery of the 1940 Imperial Valley earthquake (Rockwell and Klinger, 2013), where we also see no evidence of surface offsets near this structure along its strike to the northwest and southeast in agricultural fields with closely spaced crop rows.

Region 3 shows the most compelling evidence of shallow deformation and provides the first ever evidence of shallow faulting in this region to the west of the IF. We see two distinct locations with faulting. The first is within the postulated location of the northern extension of the MF. The offsets on reflectors here are comparable if not larger than those observed across the IF in region 1 (Figures 5.3, 5.4). The second evidence of faulting is farther east, on lines ACD03L05 and 6. We interpret transtensional faulting features here, both at greater depths and in the shallow subsurface, though we cannot resolve surface faulting of these strata.

Our observations of shallow faulting in the westernmost section of Region 3 is not unexpected, as others have proposed that the MF likely extends to the north, and that the DF accommodates some plate boundary strain here (Magistrale, 2002; Lin, 2013). (Dorsett et al., 2019b) find that the MF and Cerro Prieto fault are likely linked to the IF system, and that the adjacent DF accommodates approximately 3-8 mm/yr of slip, re-partitioning some of the UCERF3 IF slip rate onto the DF and MF. Furthermore, Lindsey and Fialko (2016) place 10-15 mm/yr of slip on an unnamed structure(s) at this latitude, which may be in part accommodated by the MF. We thus propose that the deformation on lines ACD03L12 is the shallow manifestation of slip associated with the northern extension of the MF, which is also observable in seismicity. This structure is yet to be geologically investigated north of the US-Mexico border and is not included in current fault models.

The transtensional structures on lines ACD03L05/06 may be associated with a small basin postulated by previous workers in the area (Okubo et al., 2020). However, there is no observed seismicity in comprehensive seismic catalogs (Figure 5.1) within the wide (~10km) stepover between the MF and DF (Ross et al., 2019). Other similar regional young and active basins, such as the Mesquite basin, exhibit shallow faulting and deformation and host active seismicity (Rockwell and Meltzner, 2008; Brothers et al., 2009a). We propose four possible hypotheses for the presence of shallow faulting in this region: (H1) A mature, strain-accommodating fault exists at depth, but is in the stress shadow of the 2010 El Mayor-Cucapah or 1979 Imperial Valley earthquakes; (H2) There is no main structure in this region; rather, these shallow features represent coseismic offsets from through-going rupture within the stepover; (H3) The faulting is due to coseismic offsets from rupture on either the MF of DF, that dynamically propagated into but not through the stepover, and are associated with the formation of a small local basin; (H4) The transtensional structures we observe are from a relic fault system (the MF or DF), whose activity moved to the west or east over time.

Simple models of coulomb stress change (Figures S11, S12) in the region from the 1979 Imperial Valley and 2010 El Mayor-Cucapah earthquakes test H1. The stepover does not preferentially experience an increase or decrease in stress compared to the observed seismicity lineaments, which implies that the absence of seismicity is not likely due to static stress changes. It is not possible for us to propose any further constraints on the possibility of through-going rupture (H2) with our dataset, however, we posit that this is improbable – a stepover of 10km width is highly unlikely to allow for through-going rupture (Biasi and Wesnousky, 2016). We cannot distinguish between H3 and H4 with our dataset, however both seem plausible, given the documented possibility for propagating ruptures to trigger slip on pre-existing or new structures within a radius near the rupture front (Wesnousky, 2008), for off-fault deformation to occur statically or dynamically near a large rupture or mature fault (Milliner et al., 2015; Okubo et al., 2020). Further work would be necessary to characterize the three-dimensional nature of these offsets and their timing, and to understand if they represent active fault evolution and interaction, or if they represent dynamically triggered offsets within this stepover.

## 5.6.0 Conclusions

Our novel terrestrial application of CHIRP provides the first images of subsurface deformation across structures in the Imperial Valley, including the IF and MF. It confirms that the MF/Cerro Prieto fault extends northwards into the US. We observe transtensional structures in the region between the MF and DF, potentially coseismic displacements in the stepover between these faults, or a relic fault system. We cannot place slip rates on these faults based solely on 2D imagery and lack direct dating of the imaged strata. Nevertheless, this work provides valuable constraints on the locations of future studies to understand regional strain distribution, slip rates and fault interactions in the Imperial Valley.

## 5.7.0 Acknowledgments

This work was funded on SCEC grant #18119. We thank Neal Driscoll for the use of his CHIRP; Alistair Harding for discussions regarding the seismic data; Ray Weldon and Becky Dorsey for feedback; Brian Oller and Alexis Klimasewski for help with data collection; Socrates Gonzalez and Robert Pacheco (IID) for their support of the study; and many other IID employees who gave their time to aid in data collection.

Chapter 5 has been accepted for publication in: Sahakian, V.J., Derosier, B.J., Rockwell, T.K., Stock, J.M., Accepted. Shallow Distributed Faulting in the Imperial Valley. *Geology*. The dissertation author was involved in the acquisition, interpretation, and manuscript preparation that forms the basis of this chapter. The author of the dissertation is the secondary author of this publication.

# 5.8.0 Supplemental Material

## **Supplemental Information Text 1: Methods**

### Seismic Data

Acoustic compressed high-intensity radar pulse (CHIRP) images sub-surface sediments with decimeter resolution, by coupling acoustic energy in a swept frequency pulse with water. Using two trucks on the opposite levees of the AAC (Figure 2), we towed an Edgetech SubScan JSTAR CHIRP 512 with a dual transducer XStar sonar West to East through the canal in a floating cage. We used a 50ms 0.7–3.0kHz pulse and placed a Septentrio Altus NR3 GNSS instrument on top of the CHIRP with a 1Hz sample rate to obtain real-time, sub-meter positioning on the seismic data.

We applied a time-varying gain to increase the clarity and coherency of deeper reflectors. We convert two-way travel time (TWTT) to depth assuming a water velocity of 1350-1500m/s, but only show conversions with 1500 m/s here, as they demonstrate the best correlative relationship with strata observed in nearby terrestrial cores. Depth penetration varied between survey regions, between 10 and 25m beneath the subsurface.

### $^{14}$C Dating and Sedimentation Rate

We approximate ages of the sediments by estimating two average regional sedimentation rates, as sedimentation here is episodic. This is a highly approximate endeavor, and we do not aim to use our findings here with any certainty but rather, to provide very approximate temporal constraints on our seismic images.

For age constraints, we use the most reliable $^{14}$C dates on samples recovered from nearby cores from Rockwell & Klinger (2019), and apply it to deep sediments below Lake G. This study produced two deep cores along a CPT profile, an eastern and a western core with $^{14}$C dates recovered from samples within, calibrated using OxCal (Ramsey, 2008). Calibrations were performed with an R value of 0, which is not well-constrained and partially arbitrary.

We cannot directly corroborate reflectors with units from these cores. Instead, we estimate the ages of sediments in three main steps:

1. Assume sediments <5m depth are likely younger than Lake F (the base of Lake F is ~5m depth when accounting for the 1m high berm through which the core was drilled), and obtain an age estimate from Philibosian et al. (2011) of about 1100 years BP.
2. Compute an approximate sedimentation rate for sediments between ~5m and 8m depth to the base of Lake G, dated at the Dogwood paleoseismic site (Rockwell et al., 2011), and 9m depth, corresponding roughly to the sediments below Lake G that are dated by sample

E7 from Rockwell & Klinger (2019). *For reflectors in this depth range, we add the age of Lake F to the corresponding age assuming this intermediate sedimentation rate.*

3. Compute an approximate sedimentation rate for sediments at 11-12m depth, using samples E7 and E4 (recovered from another lake level below Lake G) from Rockwell & Klinger (2019). We add the age of ~10m deep sediments from step 2 to the corresponding age of the additional depth of sediments with this deeper sedimentation rate.

**A note on the samples used in constraining sedimentation rate:** The Rockwell & Klinger (2019) eastern core samples a regional sag but presents the most reliable radiocarbon dates (samples E7 and E4 at 20.9m and 24m depth, respectively, in the eastern core). The western core is most similar to the depositional environment in the regions of our profiles, and where we think we can best correlate units with reflectors in our data. Units can, however, be correlated between the eastern and western cores; sample E7 is derived from unit 850, and E4 corresponds to unit 1000. Both are below (and thus older) than Lake F, and within the western core are at 9.0-9.8m and 11.6m depth, respectively (Table S1).

**Step 2, "Intermediate" Sedimentation Rate:** We compare sedimentation between the Lake F unit (unit 700), and unit 850. We obtain the date for unit 850 from sample E7 from Rockwell & Klinger (2019), and the depth from samples W6 and W5 (corresponding samples for unit 850 in the western core). We obtain a reliable age estimate for the Lake Cahuilla high stand Lake F from Philibosian et al. (2011). Here, Lake F is Layer 6L, and calibrated dates are presented, ~1.1 – 1.2ka (Table 3). Using this calibrated range, we obtain a minimum and maximum sedimentation rate between the appropriate Lake F unit depth of 5m in the western core of

Rockwell & Klinger (2019), and the depths of samples W5 and W6. The minimum sedimentation rate (minimum difference in depth divided by maximum difference in age) yields 4m in 1100 years, or 3.6m/kyr. The maximum sedimentation rate (maximum sedimentation, minimum age difference) yields 4.5m in 836 years, or 5.7m/kyr.

**Step 3, "Deeper" Sedimentation Rate:** We compute a minimum and maximum sedimentation rate between units 850 and 1000, using the calibrated radiocarbon dates for samples E7 and E4 and their corresponding depths in the western core. The minimum sedimentation rate is determined from the minimum depth range between samples W7 and W5, and maximum age difference based on the asymmetric calibrated dates, and yields 1.8m in 392 years, or 4.6m/kyr. The maximum sedimentation rate is determined from the maximum depth range between samples W7 and W6, and minimum age difference, and yields 2.6m in 137 years, or 19m/kyr. These are thus reported as the "average" sedimentation rate range: 4.6 – 19 m/kyr for deeper sediments, below ~10m.

**Determining Ages of Reflectors:** We are interested in the approximate ages of several reflectors. The first is at ~9.5 – 14.5m below sea level. We cannot directly corroborate units and depths between the cores and our profile. Instead, we assume the first ~5m of sediment are younger than Lake F (1.1 – 1.2ka), and the remaining 4.5 were deposited under the younger sedimentation rate (3.6 – 5.7m/kyr). Sediments at 9.5m depth are ~1.9 to 2.5ka. Sediments at ~10m depth are ~2 to 2.6ka. Sedimentation becomes more highly variable after this, so we apply the deeper, "average" sedimentation rate for the remaining 4.5m of sediment, resulting in an approximate age of 2.2 to 3.6ka. For the depth range 9.5 – 14.5m, we thus present a possible age range of ~1.9 to 3.6ka. Reflectors at ~0.0125s two-way travel time (TWTT) are at approximately 9.4m depth, thus corresponding to an age of <2.5ka, as described above.

Lastly, we note that this process is highly uncertain and prone to errors due to the nature of assumptions in the above process, as well as water velocity assumptions in converting our observations of TWTT to depth. The above ages are meant to place very approximate (Holocene or Pleistocene) constraints on our observed strata.

### Interpretations

We qualitatively characterize our faulting and deformation interpretations as “confident” (obvious offset in a reflector, usually with adjacent deformation of reflector(s)) “medium confidence” (moderate clarity, and/or deformation likely controlled by a fault structure, but no clear offsets present) and “uncertain” (low clarity, variability in character of reflectors but no clear warping of adjacent reflectors and no clear offsets). The top ~0-5m of many seismic lines show bright reflectors indicating fluvial bedforms, produced by unidirectional westward flow of the canal current (Southard, 1991).

### Coulomb Stress Models

We test the possibility that seismicity is absent in the Michoacán/Dixieland faults stepover due to a stress shadow from previous large earthquakes with simple models of coulomb stress change (Figures S9, S10) in the region from the 1979 Imperial Valley earthquake, and 2010 El Mayor-Cucapah earthquakes. We use the Coulomb 3.4 package (Lin and Stein, 2004; Toda et al., 2005). With the source models of Archuleta (1984) and Wei et al. (2011), we compute the coulomb stress change on regional receiver faults of strike 324, 317, 313, and 312 (the strike of the IF, WF, DF, and MF, respectively), assuming the strike of the features we observe are similar to the above. The dip is assumed to be 90 degrees for all. We compute the static stress change on these receiver faults at 7.5km depth, and with a Poisson's ratio of 0.25, friction coefficient of 0.4, and Young's Modulus of 80 GPa.

We additionally consider the possibility that the receiver faults may not be entirely vertical. Although the Southern California Earthquake Center Community Fault Model (SCEC CFM, Nicholson et al., 2020; Plesch et al., 2020) presents the dip of all the above faults as 90 degrees, Persaud et al. (2016) show seismicity lineaments of the Weinert-El Centro fault that graphically (not described within the manuscript) feature an approximately 56-degree dip to the northeast. We thus compute the coulomb stress change for the Archuleta et al. (1984) model on receiver faults of strike 324, dip 56 degrees; and 313, dip 56 degrees, as end members. We choose the Archuleta model as opposed to the Wei model to test this hypothesis as it demonstrates the closest difference in positive vs. negative Coulomb stress change near our study of interest. We find no demonstrable differences within our stepover of interest in this case, and thus do not present it here.

Table 1 Table of samples, units, and dates used in constraining sedimentation rate.

*Indicates samples from Rockwell et al., (2019); ** Indicates samples from Philibosian et al., 2011. Calibrated ages are from Philibosian et al. (2011), Figure 15, sample Nb4m13A-c. † Indicates the corresponding unit as described by Rockwell et al., 2019.

| **Sample** | **Depth (m)** | **Unit** | **$^{14}$C (BP)** | ± (years) | **Calibrated Age** | **Equivalent Western Core Sample** | **Equivalent Western Core Depth (m)** |
|---|---|---|---|---|---|---|---|
| **Nb4m13A-c** (Layer 6Lb SW)** | - | 700† | 1080-1185 (1.151 – 1.256 ka) | 15-30 | 795 – 900 AD (1.226 – 1.1121 ka) | - | 5 |
| **E7*** | 20.9 | 850 | 2435 (2.506 ka) | 20 | 195-41 BCE (2.216-2.062 ka) | W6 | 9.0 |
| | | | | | | W5 | 9.8 |
| **E4*** | 24 | 1000 | 2640 (2.711 ka) | 15 | 433-332 BCE (2.454 – 2.353 ka) | W7 | 11.6 |

Table 2 Locations of mapped "confident" faults from this study.

| Longitude (Decimal Degrees) | Latitude (Decimal Degrees) |
|---|---|
| **-115.60702** | 32.6572889 |
| **-115.60049** | 32.6578206 |
| **-115.54814** | 32.6616501 |
| **-115.54744** | 32.6617141 |
| **-115.54708** | 32.6617911 |
| **-115.54664** | 32.6618085 |
| **-115.53713** | 32.6625143 |
| **-115.53706** | 32.6625203 |
| **-115.53591** | 32.6626241 |
| **-115.36228** | 32.675184 |

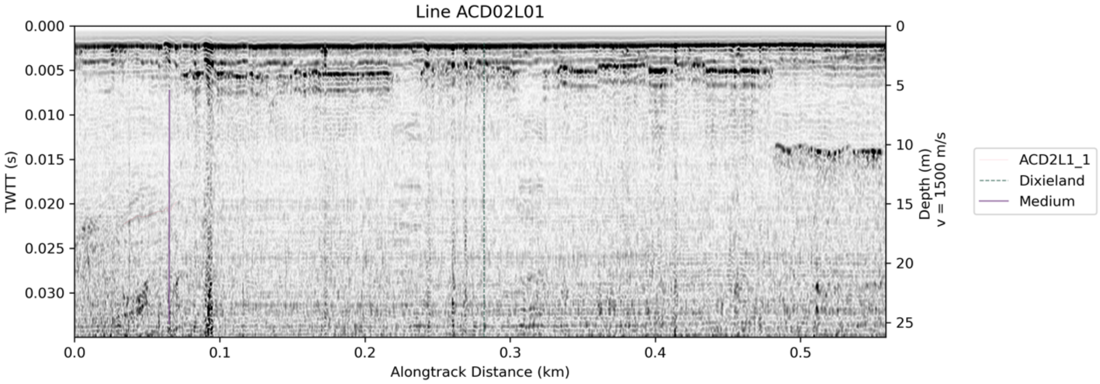

S 5 Interpreted line ACD02L01.

Day 2 Line 1 in region 2, crossing the Dixieland fault. Plotted as TWTT versus along track distance, and depths reported on the right-hand side axis are computed assuming a nominal water velocity of 1500m/s. Interpretations include horizon mapped on this line (ACD2L1_1), the mapped trace of the Dixieland fault from the Southern California Earthquake Center Community Fault Model, and a “medium” certainty mapped fault from this study.

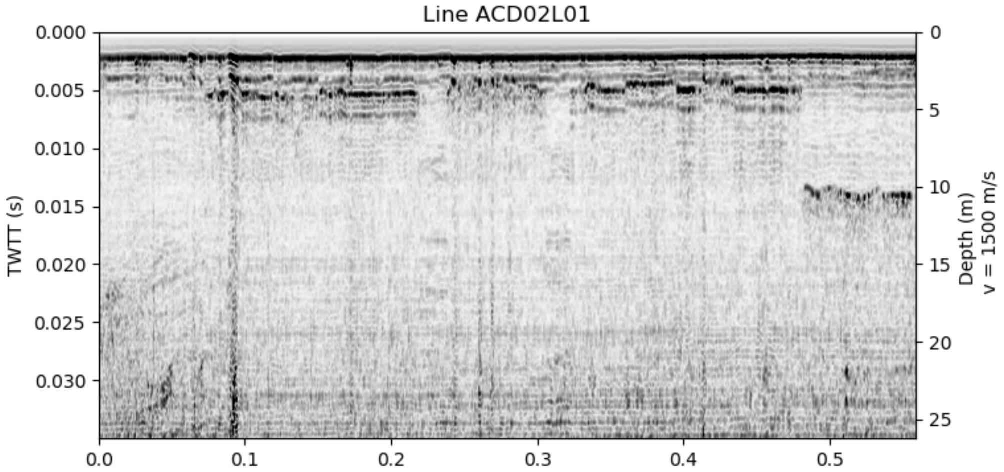

S 6 Uninterpreted line ACD02L01.

Day 2 Line 1 in region 2, crossing the Dixieland fault. Plotted as TWTT versus along track distance, and depths reported on the right-hand side axis are computed assuming a nominal water velocity of 1500m/s.

Table 3 Location of mapped "uncertain" faults from this study.

| **Longitude (Decimal Degrees)** | **Latitude (Decimal Degrees)** |
|---|---|
| -115.60957 | 32.6571436 |
| -115.60269 | 32.6576489 |
| -115.59803 | 32.657942 |
| -115.59805 | 32.6579444 |
| -115.59187 | 32.6584299 |
| -115.54087 | 32.662215 |
| -115.3593 | 32.6753931 |
| -115.35831 | 32.6754253 |
| -115.3584 | 32.6754264 |
| -115.34398 | 32.6764004 |
| -115.33479 | 32.6774489 |
| -115.32907 | 32.679028 |
| -115.49566 | 32.6864354 |

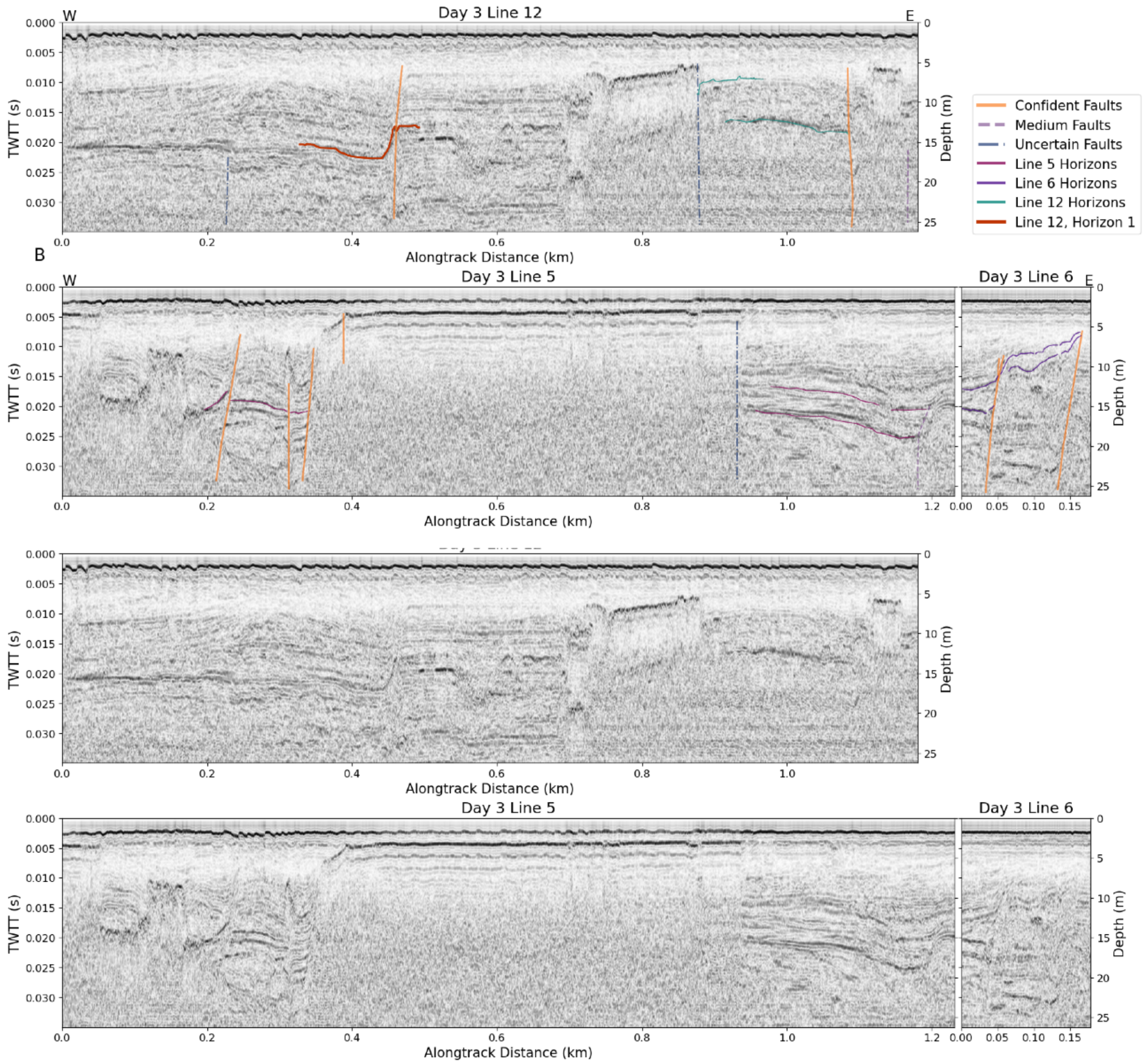

S 7 Interpreted (top two panels) and uninterpreted (bottom two panels) lines.

ACD03L12 (Day 3 Line 12), ACD03L05 (Day 3, Line 5), and ACD03L06 (Day 3, Line 6) in region 3. Plotted as TWTT versus along track distance, and depths reported on the right-hand side axis are computed assuming a nominal water velocity of 1500m/s. Interpretations include Line 5, Line 6, and Line 12 Horizons, as well as notable Horizon 1 on Line 12. Also included are “confident”, “medium”, and “uncertain” mapped structures from this study.

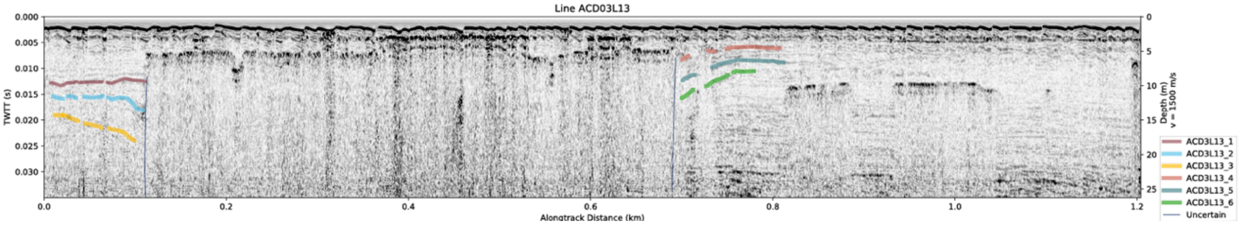

S 8 Interpreted line ACD03L13, Day 3 Line 13 in region 3.

Plotted as TWTT versus along track distance, and depths reported on the right-hand side axis are computed assuming a nominal water velocity of 1500m/s. Interpretations include 6 horizons (“ACD03L13_1” through “_6”), and “uncertain” mapped structures from this study.

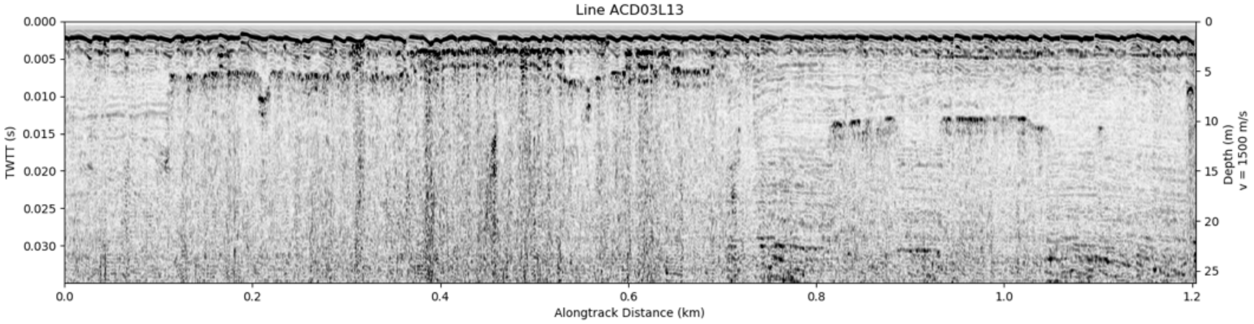

S 9 Uninterpreted line ACD03L13, Day 3 Line 13 in region 3.

Plotted as TWTT versus along track distance, and depths reported on the right-hand side axis are computed assuming a nominal water velocity of 1500m/s.

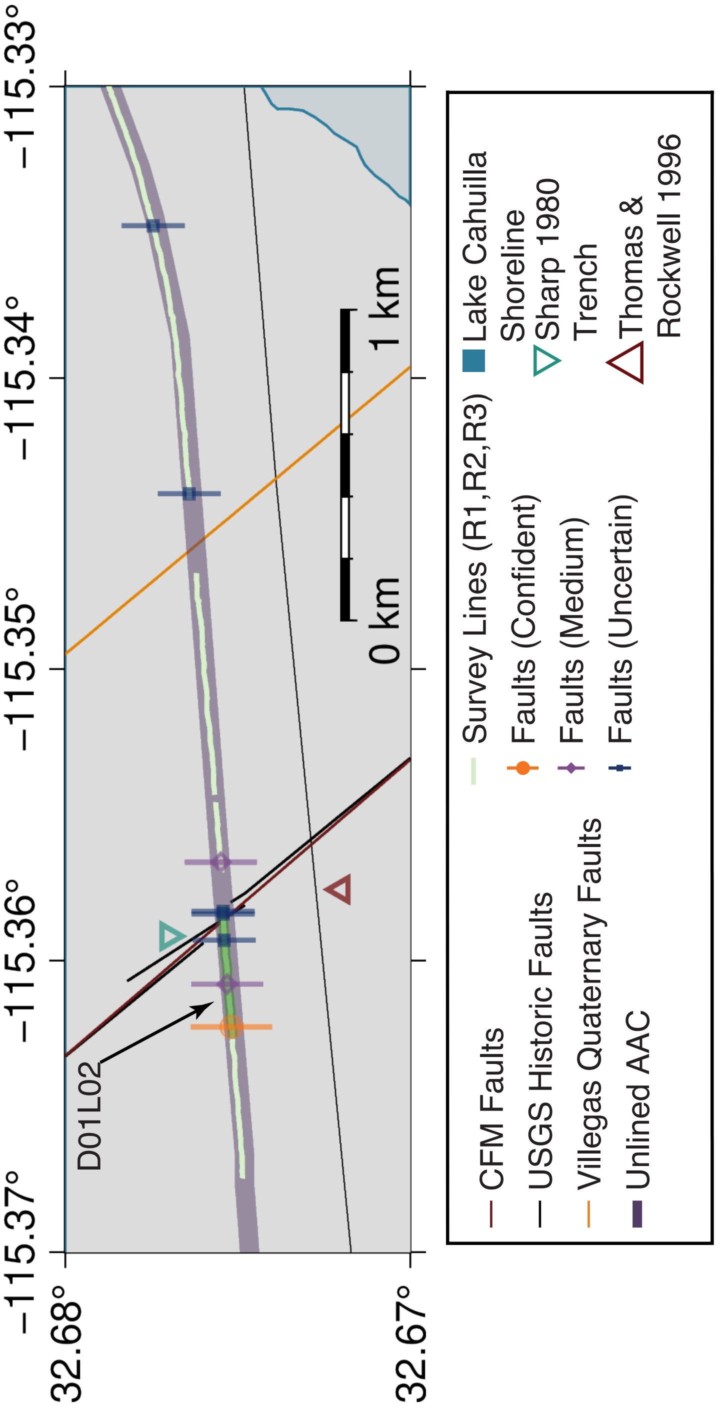

S 10 Zoom-in of Figure 1.

Map showing the Imperial Fault at the border, and respective locations of our mapped structures along with existing trenches (Sharp 1980, Thomas & Rockwell, 1996). Southern California Earthquake Center community fault model (SCEC CFM 5.3) faults (Plesch et al., 2020), US Geological Survey (USGS) historic faults (USGS, 2017), Mexico quaternary faults (Villegas et al., 2017), unlined All-American Canal (AAC), trenches of Sharp (1980) and Thomas & Rockwell (1996; T&R 1996), and the ancient Lake Cahuilla

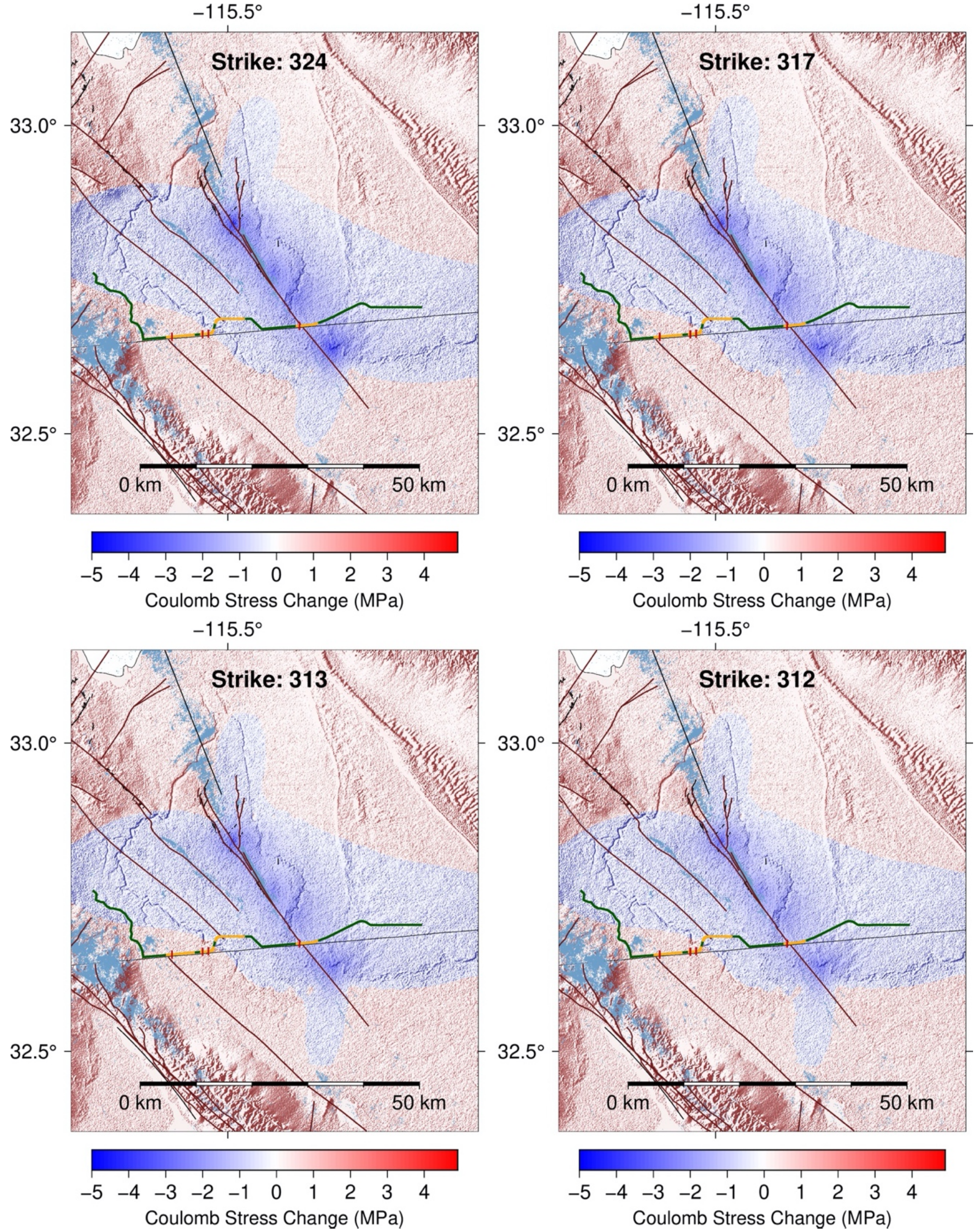

S 11 Coulomb stress changes for the Archuleta et al., (1984) 1979 Imperial Valley earthquake.

Source model on receiver faults of strike 324, 317, 313, and 312, and dip of 90 degrees.

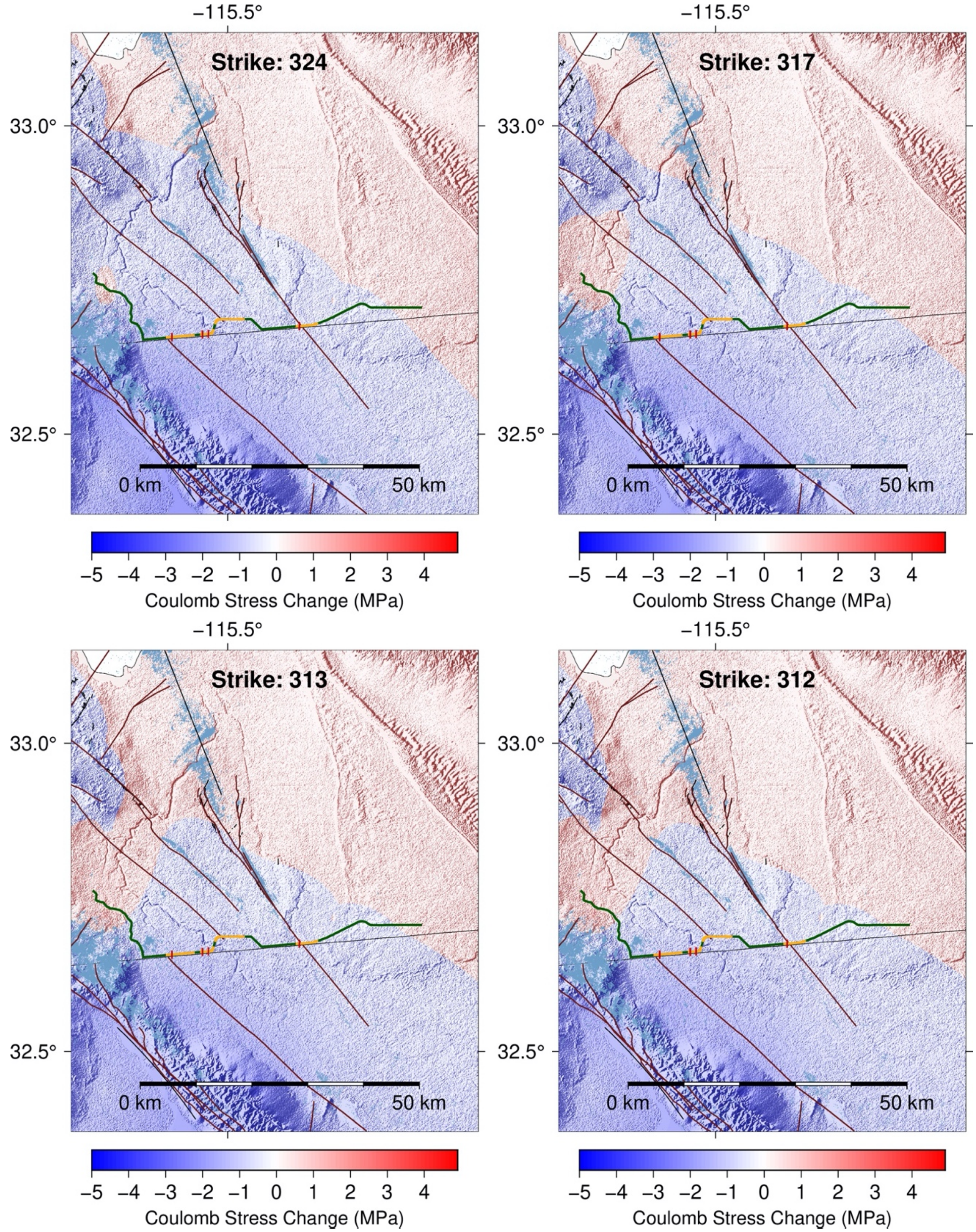

S 12 Coulomb stress changes for the Wei et al., (2011) 2010 El Mayor-Cucapah earthquake.

Source model on receiver faults of strike 324, 317, 313, and 312, and dip of 90 degrees.

# Chapter 6

# Conclusions

Despite decades of geophysical and geologic investigation, many unanswered questions exist regarding the deformational framework along Southern California's diffuse plate boundary. The goal of the research presented in the previous chapters is to identify and investigate specific questions regarding the region's geologic past and present, which can be addressed with new and legacy seismic reflection data. Within this dissertation, the stratal geometry and sea-floor morphology across Southern California's diffuse plate boundary have been observed and contextualized through the powerful lens of sequence stratigraphy.

Our findings suggest that the submerged marine terraces below LGM represent pre-Quaternary sea-level still stands. As a result, when these deeper pre-Quaternary terraces are put in context with other Miocene to present RSL indicators, such as Miocene marine sediments and fossil assemblages, a model explaining the subaerial and submarine terraces observed throughout Southern California Borderland presents itself. Our conceptual model describes how the Inner California Borderland experienced regional RSL fall through the Early to Middle Miocene. Following the Early to Middle Miocene RSL fall, there was a Middle Miocene to Pliocene increase of RSL on the order of ~1000m, followed by a Pliocene to present (~500m) decrease in RSL.

Two unconformable surfaces mapped throughout the Catalina Basin are likely associated with Early and Middle Miocene base-level falls. The timing of these surfaces is consistent with our conceptual model and agrees with regionally observed geology. In addition, these two mapped unconformities bracket a period where most likely the Catalina Basin had the environment of a shallow sea.

High-resolution sub-bottom data collected within the Outer California Borderland within the Tanner Basin suggests the Ferrelo Fault has been active within the last 1,000 years. This observation is important for the seismic hazard of Southern California as the Outer California Borderland is not generally thought of as being tectonically active.

The novel terrestrial application of a CHIRP sub-bottom within an unlined section of the All-American Canal imaged deformation associated with the Imperial, Dixieland, and Michoacán Faults in a region where anthropogenic activity has made direct observations difficult. This work provides valuable observational evidence of strain partitioning within the Imperial Valley and confirmation that the Michoacán/Cerro Prieto Fault extends northward into the US.

# REFERENCES

Adler, J.A., 2003, Chronology, Morphology, and Deformation of The Marine Terraces On San Clemente Island: Unpublished M. S. thesis, Department of Geological Sciences, San Diego State University, San Diego, p. 1–153.

Archuleta, R.J., 1984, A faulting model for the 1979 Imperial Valley earthquake: Journal of Geophysical Research: Solid Earth, v. 89, p. 4559–4585, doi:10.1029/JB089iB06p04559.

Arnal, R.E., and Vedder, J.G., 1974, Late Miocene Paleobathymetry of the California Continental Borderland North of 32°:

Atwater, T., 1970, Implications of Plate Tectonics for the Cenozoic Tectonic Evolution of Western North America: Geological Society of America Bulletin, v. 81, p. 3513–3535.

Atwater, T., and Stock, J., 1998, Pacific-North America Plate Tectonics of the Neogene Southwestern United States: An Update: International Geology Review, v. 40, p. 375–402, doi:10.1080/00206819809465216.

Balster-Gee, A.F., Brothers, D.., Roland, E.., Kluesner, J.., Hart, P.., Conrad, J.., Myers, E.., Ebuna, D.., and Edwards, J.., 2020, Multichannel minisparker and chirp seismic-reflection data of USGS field activity 2016-616-FA collected in the Catalina Basin offshore southern California in February 2016: U.S. Geological Survey data release,:, doi:https://doi.org/10.5066/P9BLAJ72.

Balster-Gee, A.., Kluesner, J.., Brothers, D.., Conrad, J.., and Sliter, R.W., 2017, Minisparker and chirp seismic-reflection data of field activity 2014-645-FA collected in the outer Santa Barbara Channel, California, between 2014-11-12 to 2014-11-25 (ver. 2.0, March 2020): U.S. Geological Survey data release:, doi:https://doi.org/10.5066/F7CV4FW6.

Behl, R.J., 1999, Since Bramlette (1946): The Miocene Monterey Formation of California revisited, *in* in Moores, E. M., Sloan, D., and Stout, D. L., eds., Classic Cordilleran Concepts: A View from California: Boulder, Colorado, Geological Society of America Special Paper 338, Geological Society of America, p. 301–313, doi:10.1130/0-8137-2338-8.301.

Berner, R. a, Lasaga, a C., and Garrels, R.M., 1983, Carbonate-silicate geochemical cycle and its effect on atmospheric carbon dioxide over the past 100 million years: Journal Name: Am. J. Sci.; (United States); Journal Volume: 283:7, p. Medium: X; Size: Pages: 641--683, doi:10.2475/ajs.283.7.641.

Biasi, G.P., and Wesnousky, S.G., 2016, Steps and Gaps in Ground Ruptures: Empirical Bounds on Rupture Propagation: Bulletin of the Seismological Society of America, v. 106, p. 1110–1124, doi:10.1785/0120150175.

Bohannon, R.G., and Geist, E., 1998, Upper crustal structure and Neogene tectonic development of the California continental borderland: Geological Society of America Bulletin, v. 110, p. 779–800, doi:10.1130/0016-7606(1998)110<0779:UCSANT>2.3.CO;2.

Bohannon, R.G., and Parsons, T., 1995, Tectonic implications of post–30 Ma Pacific and North American relative plate motions: Geological Society of America Bulletin, v. 107, p. 937–0959, doi:10.1130/0016-7606(1995)107<0937:TIOPMP>2.3.CO;2.

Brothers, D.S., Conrad, J.E., Maier, K.L., Paull, C.K., McGann, M., and Caress, D.W., 2015, The Palos Verdes Fault offshore Southern California: Late Pleistocene to present tectonic geomorphology, seascape evolution, and slip rate estimate based on AUV and ROV surveys: Journal of Geophysical Research: Solid Earth, v. 120, p. 4734–4758, doi:10.1002/2015JB011938.

Brothers, D.S., Driscoll, N.W., Kent, G.M., Harding, A.J., Babcock, J.M., and Baskin, R.L., 2009a, Tectonic evolution of the Salton Sea inferred from seismic reflection data: Nature Geoscience, v. 2, p. 581–584, doi:10.1038/ngeo590.

Brothers, D.S., Kent, G.M., Driscoll, N.W., Smith, S.B., Karlin, R., Dingler, J.A., Harding, A.J., Seitz, G.G., and Babcock, J.M., 2009b, New Constraints on Deformation, Slip Rate, and Timing of the Most Recent Earthquake on the West Tahoe-Dollar Point Fault, Lake Tahoe Basin, California: Bulletin of the Seismological Society of America, v. 99, p. 499–519, doi:10.1785/0120080135.

Buckles, J.E., Kashiwase, K., and Krantz, T., 2002, Reconstruction of prehistoric Lake Cahuilla in the Salton Sea Basin using GIS and GPS: Hydrobiologia, v. 473, p. 55–57, doi:10.1023/A:1016513214122.

Castillo, C.M., Klemperer, S.L., Ingle, J.C., Powell, C.L., Legg, M.R., and Francis, R.D., 2019, Late Quaternary subsidence of Santa Catalina Island, California Continental Borderland, demonstrated by seismic-reflection data and fossil assemblages from submerged marine terraces: GSA Bulletin, v. 131, p. 21–42, doi:10.1130/B31738.1.

Catuneanu, O., 2006, Principles of sequence stratigraphy, *in* Elsevier, Elsevier, p. 1–387.

Chaytor, J.D., Goldfinger, C., Meiner, M.A., Huftile, G.J., Romsos, C.G., and Legg, M.R., 2008, Measuring vertical tectonic motion at the intersection of the Santa Cruz-Catalina Ridge and Northern Channel Islands platform, California Continental Borderland, using submerged paleoshorelines: Geological Society of America Bulletin, v. 120, p. 1053–1071, doi:10.1130/B26316.1.

Chemical relaxation studies on the system liver alcohol dehydrogenase, NADH and imidazole.

Christie-Blick, N., 1991, Onlap, offlap, and the origin of unconformity-bounded depositional sequences: Sedimentary Geology, v. 70, p. 105–107, doi:10.1016/0037-0738(91)90137-3.

Christie-Blick, N., and Biddle, K.., 1985, Deformation and Basin Formation Along Strike-Slip Faults: Strike-Slip Deformation, Basin Formation, and Sedimentation, p. 1–34, doi:10.2110/pec.85.37.0001.

Christie-Blick, N., and Driscoll, N.W., 1995, Sequence Stratigraphy: Annual Review of Earth and Planetary Sciences, v. 23, p. 451–478, doi:10.1146/annurev.ea.23.050195.002315.

Cole, R.B., and Basu, A.R., 1995, Nd-Sr isotopic geochemistry and tectonics of ridge subduction and middle Cenozoic volcanism in western California: Geological Society of America Bulletin, v. 107, p. 167, doi:10.1130/0016-7606(1995)107<0167:NSIGAT>2.3.CO;2.

Crouch, J.K., and Suppe, J., 1993, Late Cenozoic tectonic evolution of the Los Angeles Basin and inner California borderland: a model for core complex-like crustal extension: Geological Society of America Bulletin, v. 105, p. 1415–1434, doi:10.1130/0016-7606(1993)105<1415:LCTEOT>2.3.CO;2.

Crowell, B.W., Bock, Y., Sandwell, D.T., and Fialko, Y., 2013, Geodetic investigation into the deformation of the Salton Trough: Journal of Geophysical Research: Solid Earth, v. 118, p. 5030–5039, doi:10.1002/jgrb.50347.

Le Dantec, N., Hogarth, L.J., Driscoll, N.W., Babcock, J.M., Barnhardt, W.A., and Schwab, W.C., 2010, Tectonic controls on nearshore sediment accumulation and submarine canyon morphology offshore La Jolla, Southern California: Marine Geology, v. 268, p. 115–128, doi:10.1016/j.margeo.2009.10.026.

Darigo, N.J., and Osborne, R.H., 1986, Quaternary stratigraphy and sedimentation of the inner continental shelf, San Diego County, California: Canadian Society of Petroleum Geologists, Memoir II: Shelf Sands and Sandstones, v. 11, p. 73–98.

Day, J.M.D., Koppers, A.A.P., Mendenhall, B.C., and Oller, B., 2019, The Scripps Dike and Its Implications for Mid-Miocene Volcanism and Tectonics of the California Continental Borderland, *in* From the Mountains to the Abyss: The California Borderland as an Archive of Southern California Geologic Evolution, SEPM (Society for Sedimentary Geology), v. 110, p. 43–55, doi:10.2110/sepmsp.110.02.

Detrick, R.S., Von Herzen, R.P., Parsons, B., Sandwell, D., and Dougherty, M., 1986, Heat flow observations on the Bermuda Rise and thermal models of midplate swells: Journal of Geophysical Research: Solid Earth, v. 91, p. 3701–3723, doi:10.1029/jb091ib03p03701.

Dickinson, W.R., 1997, OVERVIEW: Tectonic implications of Cenozoic volcanism in coastal California: Geological Society of America Bulletin, v. 109, p. 936–954, doi:10.1130/0016-7606(1997)109<0936:OTIOCV>2.3.CO;2.

Dokka, R.K. and, and Travis, J., 1990, Role of the eastern california shear zone in integrated shear along the to historic measurements mm yr present rate mm yr 4 determined: Geophysical Research Letters, v. 17, p. 1323–1326.

Donnelly, L.J., and Melton, N.D., 1995, Compression ridges in subsidence troughs: Géotechnique, v. 45, p. 555–560, doi:10.1680/geot.1995.45.3.555.

Dorsett, J.H., Madden, E.H., Marshall, S.T., and Cooke, M.L., 2019a, Mechanical models suggest fault linkage through the imperial valley, california, U.S.A.: Bulletin of the Seismological Society of America, v. 109, p. 1217–1234, doi:10.1785/0120180303.

Dorsett, J.H., Madden, E.H., Marshall, S.T., and Cooke, M.L., 2019b, Mechanical models suggest fault linkage through the imperial valley, california, U.S.A.: Bulletin of the Seismological Society of America, v. 109, p. 1217–1234, doi:10.1785/0120180303.

Driscoll, N.W., and Hogg, J.R., 1995, Stratigraphic response to basin formation: Jeanne d'Arc Basin, offshore Newfoundland: Geological Society, London, Special Publications, v. 80, p. 145–163, doi:10.1144/GSL.SP.1995.080.01.07.

Driscoll, N.W., and Karner, G.D., 1998, Lower crustal extension across the Northern Carnarvon basin, Australia: Evidence for an eastward dipping detachment: Journal of Geophysical Research: Solid Earth, v. 103, p. 4975–4991, doi:10.1029/97jb03295.

Driscoll, N.W., and Karner, G.D., 1999, Three-dimensional quantitative modeling of clinoform development: Marine Geology, v. 154, p. 383–398, doi:10.1016/S0025-3227(98)00125-X.

Emery, K.O., 1958, Shallow submerged marine terraces of Southern California: Bulletin of the

Geological Society of America, v. 69, p. 39–60.

Fairbanks, R.G., 1989, A 17,000-year glacio-eustatic sea level record: influence of glacial melting rates on the Younger Dryas event and deep-ocean circulation: Nature, v. 342, p. 637–642, doi:10.1038/342637a0.

Field, E.H., Arrowsmith, R.J., Biasi, G.P., Bird, P., Dawson, T.E., Felzer, K.R., Jackson, D.D., Johnson, K.M., Jordan, T.H., Madden, C. and Michael, A.J., 2014, Uniform California Earthquake Rupture Forecast, version 3 (UCERF3) -The time-independent model: Bulletin of the Seismological Society of America, v. 104, p. 1122–1180, doi:10.1785/0120130164.

Figueiredo, P.M., Cabral, J., and Rockwell, T.K., 2013, Recognition of Pleistocene marine terraces in the southwest of Portugal (Iberian Peninsula): Evidences of regional quaternary uplift: Annals of Geophysics, v. 56, doi:10.4401/ag-6276.

Fischer, P.J., Patterson, R., Rudat, J.H., and Darrow, A.C., 1987, The Palos Verdes Fault Zone: Onshore and off shore, *in* SPEM, v. Geology of, p. 91–133.

Francis, R.D., Legg, M.R., and Castillo, C.M., 2019, Shear zone faulting, basin evolution, and volcanism along a continental margin transform system: San Pedro basin, offshore Southern California: SEPM Special Publications, v. 110, p. 56–77, doi:10.2110/sepmsp.110.13.

Glazner, A.F., 1991, Plutonism, oblique subduction, and continental growth: An example from the Mesozoic of California: Geology, v. 19, p. 784, doi:10.1130/0091-7613(1991)019<0784:POSACG>2.3.CO;2.

Gold, R.D., Briggs, R.W., Crone, A.J., and DuRoss, C.B., 2017, Refining fault slip rates using multiple displaced terrace risers—An example from the Honey Lake fault, NE California, USA: Earth and Planetary Science Letters, v. 477, p. 134–146, doi:10.1016/j.epsl.2017.08.021.

Goldfinger, C.., Nelson, C.H., Morey, A.E., Johnson, J.E., Patton, J.R., Dunhill, G., Enkin, R.J., Dallimore, A., and Vallier, T.L., 2012, Turbidite Event History — Methods and Implications for Holocene Paleoseismicity of the Cascadia Subduction Zone: U.S. Geological Survey Professional Paper 1661–F, 170 p, http://pubs.usgs.gov/pp/pp1661/f%0A.

González-Escobar, M., Mares Agüero, M.A., and Martin, A., 2020, Subsurface structure revealed by seismic reflection images to the southwest of the Cerro Prieto pull-apart basin, Baja California: Geothermics, v. 85, p. 101779, doi:10.1016/j.geothermics.2019.101779.

Gonzalo, V., Mendoza, C., and Ferrari, L., 2017, Mexico Quaternary Fault Database / Base de datos de fallas Cuaternarias de México: Terra digitalis, v. 1, p. 1–9, doi:10.22201/igg.terradigitalis.2017.1.3.68.

Gorsline, D.S., Drake, D.., and Barns, P.W., 1968, Holocene Sedimentation in Tanner Basin, California Continental Borderland Abstract: GSA Bulletin, v. 79, p. 659–674.

Grant, L.B., Waggoner, J.T., Rockwell, T.K., and Von Stein, C., 1997, Paleoseismicity of the North Branch of the Newport-Inglewood fault zone in Huntington Beach, California, from cone penetrometer test data: Bulletin of the Seismological Society of America, v. 87, p. 277–293.

Grove, M., Bebout, G.E., Jacobson, C.E., Barth, A.P., Kimbrough, D.L., King, R.L., Zou, H., Lovera, O.M., Mahoney, B.J., and Gehrels, G.E., 2008, The Catalina Schist: Evidence for middle Cretaceous subduction erosion of southwestern North America, *in* Special Paper 436: Formation and Applications of the Sedimentary Record in Arc Collision Zones, Geological Society of America, p. 335–361, doi:10.1130/2008.2436(15).

Gurrola, L.D., Keller, E.A., Chen, J.H., Owen, L.A., and Spencer, J.Q., 2014, Tectonic geomorphology of marine terraces: Santa Barbara fold belt, California: Bulletin of the Geological Society of America, v. 126, p. 219–233, doi:10.1130/B30211.1.

Haaker, E.C., Rockwell, T.K., Kennedy, G.L., Grant Ludwig, L., Freeman, T.S., Zumbro, J.A., Muller, K.J.., and Edwards, L.R., 2016, Style and Rate of Long-Term Uplift of the Southern California Coast Between San Diego and Newport Beach with Potential Implications for Assessing Blind Thrust Models: Ch. 26, *in* Anderson, R.H.F. ed., Applied Geology in California, Environmental Engineering Geologists, Star Publishing, p. 679–719.

Han, L., Hole, J.A., Stock, J.M., Fuis, G.S., Kell, A., Driscoll, N.W., Kent, G.M., Harding, A.J., Rymer, M.J., González-Fernández, A. and Lázaro-Mancilla, O.,2016, Continental rupture and the creation of new crust in the Salton Trough rift, Southern California and northern Mexico: Results from the Salton Seismic Imaging Project: Journal of Geophysical Research: Solid Earth, v. 121, p. 7469–7489, doi:10.1002/2016JB013139.

Heider, F., Bock, J.M., Hendy, I., Kennett, J.P., Matzka, J., and Schneider, J., 2001, Latest Quaternary rock magnetic record of climatic and oceanic change, Tanner Basin, California borderland: Geological Society of America Bulletin, v. 113, p. 346–359, doi:10.1130/0016-7606(2001)113<0346:LQRMRO>2.0.CO;2.

Henkart, P., 2003, SIOSEIS "Software": Scripps Institution of Oceanography, La Jolla, CA, p. Available at "https://sioseis.ucsd.edu."

Hogarth, L.J., Babcock, J.M., Driscoll, N.W., Le Dantec, N., Haas, J.K., Inman, D.L., and Masters, P.M., 2007, Long-term tectonic control on Holocene shelf sedimentation offshore La Jolla, California: Geology, v. 35, p. 275–278, doi:10.1130/G23234A.1.

Hogarth, L.J., Driscoll, N.W., Babcock, J.M., and Orange, D.L., 2012, Transgressive deposits along the actively deforming Eel River Margin, Northern California: Marine Geology, doi:10.1016/j.margeo.2012.02.005.

Holmes, J.J., Driscoll, N.W., and Kent, G.M., 2021, High-Resolution 3D Seismic Imaging of Fault Interaction and Deformation Offshore San Onofre, California: Frontiers in Earth Science, v. 9, p. 1–19, doi:10.3389/feart.2021.653672.

Hornafius, J.S., Luyendyk, B.P., Terres, R.R., and Kamerling, M.J., 1986, Timing and extent of Neogene tectonic rotation in the western Transverse Ranges, California ( USA).: Geological Society of America Bulletin, v. 97, p. 1476–1487, doi:10.1130/0016-7606(1986)97<1476:TAEONT>2.0.CO;2.

Humphreys, E.D., 1995, Post-Laramide removal of the Farallon slab,western United States: Geology, v. 23, p. 987–990, doi:10.1130/0091-7613(1995)023<0987:PLROTF>2.3.CO;2.

Jerrett, A.S., 2016, PALEOSEISMOLOGY OF THE IMPERIAL FAULT AT THE U . S . - MEXICO BORDER , AND CORRELATION OF REGIONAL LAKE STRATIGRAPHY THROUGH ANALYSIS OF OXYGEN / CARBON ISOTOPE DATA Presented to the Faculty of San Diego State University In Partial Fulfillment of the Requ: M.S. thesis, Geological Sciences, San Diego State University, San Diego, CA, USA,.

Kamerling, M.J., and Luyendyk, B.P., 1979, Tectonic rotations of the Santa Monica Mountains region, western Transverse Ranges, California, suggested by paleomagnetic vectors: Bulletin of the Geological Society of America, v. 90, p. 331–337, doi:10.1130/0016-7606(1979)90<331:TROTSM>2.0.CO;2.

Karner, G.D., Driscoll, N.W., and Weissel, J.K., 1993, Response of the lithosphere to in-plane force variations: Earth and Planetary Science Letters, v. 114, p. 397–416, doi:10.1016/0012-821X(93)90072-H.

Kern, J.P., and Rockwell, T.K., 1992a, Chronology and deformation of Quaternary marine shorelines, San Diego County, California: Quaternary coasts of the United States, p. 377–382, doi:10.2110/pec.92.48.0377.

Kern, J.P., and Rockwell, T.K., 1992b, Chronology and deformation of Quaternary marine shorelines, San Diego County, California: Quaternary coasts of the United States: Published by SEPM (Society for Sedimentary Geology), p. 377–382.

Klotsko, S., Driscoll, N., Kent, G., and Brothers, D., 2015, Continental shelf morphology and stratigraphy offshore San Onofre, California: The interplay between rates of eustatic change and sediment supply: Marine Geology, v. 369, p. 116–126, doi:10.1016/j.margeo.2015.08.003.

Kreemer, C., Blewitt, G., and Hammond, W.C., 2010, Evidence for an active shear zone in southern Nevada linking the Wasatch fault to the Eastern California shear zone: Geology, v. 38, p. 475–478, doi:10.1130/G30477.1.

Lamar, D.L., Merifield, P.M., and Stout, M.L., 1968, Engineering Geology Of Rocks In Core Hole, Eel Point, San Clemente Island, California.:

Larsen, S., and Reilinger, R., 1991, Age Constraintsfor the Present Fault Configurationin the Imperial Valley, California: Evidence for Northwestward Propagation of the Gulf of California Rift System: Journal of Geophysical Research, v. 96, p. 10,339-10,346.

Legg, M.R., 1991, Developments in understanding the tectonic evolution of the California Continental Borderland: From shoreline to abyss: SEPM (Society for Sedimentary Geology) Special Publication, v. 46, p. 291–312, http://archives.datapages.com/data/sepm_sp/SP46/Developments_in_Understanding.htm.

Legg, M.R., Kohler, M.D., Shintaku, N., and Weeraratne, D.S., 2015, High-resolution mapping of two large-scale transpressional fault zones in the California Continental Borderland: Santa Cruz-Catalina Ridge and Ferrelo faults: Journal of Geophysical Research: Earth Surface, v. 120, p. 915–942, doi:10.1002/2014JF003322.

Legg, M.R., Wong, V.O., and Suarez-V, F., 1991, Geologic Borderland, structure and tectonics of the inner continental of northern Baja California: In: J. Dauphin and B. Simoneit eds., Gulf and Peninsular Province of the Californias, Am. Assoc. Pet. Geol., Mem., v. 47, p. 145–177.

Levi, S., and Yeats, R.S., 2003, Paleomagnetic definition of crustal fragmentation and Quaternary block rotations in the east Ventura Basin and San Fernando valley, southern California: Tectonics, v. 22, doi:10.1029/2002TC001377.

Lin, G., 2013, Three-Dimensional Seismic Velocity Structure and Precise Earthquake Relocations in the Salton Trough, Southern California: Bulletin of the Seismological Society of America, v. 103, p. 2694–2708, doi:10.1785/0120120286.

Lin, J., and Stein, R.S., 2004, Stress triggering in thrust and subduction earthquakes and stress interaction between the southern San Andreas and nearby thrust and strike-slip faults: Journal of Geophysical Research: Solid Earth, v. 109, p. 1–19, doi:10.1029/2003jb002607.

Lindsey, E.O., and Fialko, Y., 2016, Geodetic constraints on frictional properties and earthquake hazard in the Imperial Valley, Southern California: Journal of Geophysical Research: Solid Earth, v. 121, p. 1097–1113, doi:10.1002/2015JB012516.

Lindvall, S.C., and Rockwell, T.K., 1995, Holocene activity of the Rose Canyon fault zone in San Diego, California: Journal of Geophysical Research: Solid Earth, v. 100, p. 24121–24132, doi:10.1029/95JB02627.

Lisiecki, L.E., and Raymo, M.E., 2005, A Pliocene-Pleistocene stack of 57 globally distributed benthic δ 18 O records: Paleoceanography, v. 20, p. 1–17, doi:10.1029/2004PA001071.

Liu, L., and Stegman, D.R., 2012, Origin of Columbia River flood basalt controlled by propagating rupture of the Farallon slab.: Nature, v. 482, p. 386–9, doi:10.1038/nature10749.

Lonsdale, P., 1991, Structural patterns of the Pacific floor offshore of peninsular California, Chapter 7: Part (III), *in* AAPG Special Publications: The Gulf and Peninsular Province of the Californias, v. 47, p. 87–125, doi:https://doi.org/10.1306/M47542C7.

Luyendyk, B.P., Kamerling, M.J., and Terres, R., 1980, Geometric model for Neogene crustal rotations in southern California.: Geological Society of America Bulletin, v. 91, p. 211–217, doi:10.1130/0016-7606(1980)91<211:GMFNCR>2.0.CO;2.

Lyle, M., Koizumi, I., and Richter, C., 1996, OCEAN DRILLING PROGRAM LEG 167 PRELIMINARY REPORT CALIFORNIA MARGIN:, http://www-odp.tamu.edu/publications.

Magistrale, H., 2002, The relation of the southern San Jacinto Fault Zone to the Imperial and Cerro Prieto Faults: Special Papers-Geological Society of America,.

Maier, K.L., Roland, E.C., Walton, M.A.L., Conrad, J.E., Brothers, D.S., Dartnell, P., and Kluesner, J.W., 2018, The Tectonically Controlled San Gabriel Channel–Lobe Transition Zone, Catalina Basin, Southern California Borderland: Journal of Sedimentary Research, v. 88, p. 942–959, doi:10.2110/jsr.2018.50.

Maloney, J.M. et al., 2013, Paleoseismic history of the Fallen Leaf segment of the West Tahoe–Dollar Point fault reconstructed from slide deposits in the Lake Tahoe Basin, California-Nevada: Geosphere, v. 9, p. 1065–1090, doi:10.1130/GES00877.1.

Maloney, J.M., Driscoll, N.W., Kent, G.M., Bormann, J., Duke, S., Freeman, T.S., Maloney, J.M., and Ana, S., 2016a, Segmentation and Step-Overs Along Strike- Slip Fault Systems in the Inner California Borderlands : Implications for Fault Architecture and Basin Formation: Ch 37, *in* Anderson, R. and Ferriz, H. eds., Applied Geology in California, Environmental Engineering Geologists, Star Publishing, p. 655–677.

Maloney, J.M., Driscoll, N.W., Maloney, J.M., and Ana, S., 2016b, Segmentation and Step-

Overs Along Strike- Slip Fault Systems in the Inner California Borderlands : Implications for Fault Architecture and Basin Formation: Applied Geology in California, Environmental Engineering Geologists, p. 655–677.

Maloney, J.M., Grupe, B.M., Pasulka, A.L., Dawson, K.S., Case, D.H., Frieder, C.A., Levin, L.A., and Driscoll, N.W., 2015, Transpressional segment boundaries in strike-slip fault systems offshore southern California: Implications for fluid expulsion and cold seep habitats: Geophysical Research Letters, v. 42, p. 4080–4088, doi:10.1002/2015GL063778.

McInnis, M., and Pinter, N., 2021, Uplifted marine terraces on Santa Catalina Island, California, USA: Geology, v. 49, p. 804–809, doi:10.1130/G48219.1.

McKenzie, D., 1978, Some remarks on the development of sedimentary basins: Earth and Planetary Science Letters, v. 40, p. 25–32, doi:10.1016/0012-821X(78)90071-7.

McNeilan, T.W., Rockwell, T.K., and Resnick, G.S., 1996, Style and rate of Holocene slip, Palos Verdes fault, southern California: Journal of Geophysical Research, v. 101, p. 8317, doi:10.1029/95JB02251.

McNutt, M.K., 1998, SUPERSWELLS: AGU: Reviews of Geophysics, v. 38, p. 211–244.

McNutt, M.K., and Fisher, K.M., 1987, The South Pacific Superswell: American Geophysical Union: Seamounts, Islands, and Atolls, v. 43, p. 25–34.

Merifield, P.M., Lamar, D.L., and Stout, M.L., 1971, Geology of central San Clemente Island, California: Bulletin of the Geological Society of America, v. 82, p. 1989–1994, doi:10.1130/0016-7606(1971)82[1989:GOCSCI]2.0.CO;2.

Milliner, C.W.D., Dolan, J.F., Hollingsworth, J., Leprince, S., Ayoub, F., and Sammis, C.G., 2015, Quantifying near-field and off-fault deformation patterns of the 1992 M w 7.3 Landers earthquake: Geochemistry, Geophysics, Geosystems, v. 16, p. 1577–1598, doi:10.1002/2014GC005693.

Morton, D.M., Miller, F.K., Kistler, R.W., Premo, W.R., Lee, C.T.A., Langenheim, V.E., Wooden, J.L., Snee, L.W., Clausen, B.L., and Cossette, P., 2014, Framework and petrogenesis of the northern Peninsular Ranges batholith, southern California: Memoir of the Geological Society of America, v. 211, p. 61–143, doi:10.1130/2014.1211(03).

Mueller, K., Kier, G., Rockwell, T., and Jones, C.H., 2009, Quaternary rift flank uplift of the Peninsular Ranges in Baja and southern California by removal of mantle lithosphere: Tectonics, v. 28, p. 1–17, doi:10.1029/2007TC002227.

Muhs, D.R., 2002, Evidence for the Timing and Duration of the Last Interglacial Period from High-Precision Uranium-Series Ages of Corals on Tectonically Stable Coastlines: Quaternary Research, v. 58, p. 36–40, doi:10.1006/qres.2002.2339.

Muhs, D.R., 1983, Quaternary sea-level events on northern San Clemente Island, California: Quaternary Research, v. 20, p. 322–341, doi:10.1016/0033-5894(83)90016-9.

Muhs, D.R., and Groves, L.T., 2018, Little Islands Recording Global Events: Late Quaternary Sea Level History and Paleozoogeography of Santa Barbara and Anacapa Islands, Channel Islands National Park, California: Western North American Naturalist, v. 78, p. 540, doi:10.3398/064.078.0403.

Muhs, D.R., Kennedy, G.L., and Rockwell, T.K., 1994, Uranium-series ages of marine terrace corals from the pacific coast of north america and implications for last-interglacial sea level history: Quaternary Research, v. 42, p. 72–87, doi:10.1006/qres.1994.1055.

Muhs, D.R., Rockwell, T.K., and Kennedy, G.L., 1992, Late quaternary uplift rates of marine terraces on the Pacific coast of North America, southern Oregon to Baja California sur: Quaternary International, v. 15–16, p. 121–133, doi:10.1016/1040-6182(92)90041-Y.

Muhs, D.R., Schumann, R.R., Groves, L.T., Simmons, K.R., and Florian, C.R., 2021, The marine terraces of Santa Cruz Island, California: Implications for glacial isostatic adjustment models of last-interglacial sea-level history: Geomorphology, v. 389, p. 107826, doi:10.1016/j.geomorph.2021.107826.

Muhs, D.R., Simmons, K.R., Schumann, R.R., Groves, L.T., DeVogel, S.B., Minor, S.A., and Laurel, D.A., 2014, Coastal tectonics on the eastern margin of the Pacific Rim: Late Quaternary sea-level history and uplift rates, Channel Islands National Park, California, USA: Quaternary Science Reviews, v. 105, p. 209–238, doi:10.1016/j.quascirev.2014.09.017.

Muhs, D.R., Simmons, K.R., Schumann, R.R., Groves, L.T., Mitrovica, J.X., and Laurel, D., 2012, Sea-level history during the Last Interglacial complex on San Nicolas Island, California: implications for glacial isostatic adjustment processes, paleozoogeography and tectonics: Quaternary Science Reviews, v. 37, p. 1–25, doi:10.1016/j.quascirev.2012.01.010.

Muhs, D.R., and Szabo, B.J., 1982, Uranium-series age of the Eel Point terrace San Clemente Island, California.: Geology, v. 10, p. 23–26, doi:10.1130/0091-7613(1982)10<23:UAOTEP>2.0.CO;2.

Murphy, J.B., Oppliger, G.L., and Brimhall, G.H., 1998, Plume-modified orogeny: An example from the western United States: Geology, v. 26, p. 731–734, doi:10.1130/0091-7613(1998)026<0731:PMOAEF>2.3.CO;2.

National Geophysical Data Center, 2012, 2012. U.S. Coastal Relief Model - Southern California vers. 2: National Geophysical Data Center, NOAA, doi:10.7289/V5V985ZM.

Nicholson, C., Plesch, A., Sorlien, C.C., Shaw, J.H., and Hauksson, E., 2020, Updates, Evaluation and Improvements to the Community Fault Model (CFM version 5.3).: Poster Presentation at 2020 SCEC Annual Meeting. SCEC Contribution 10412, v. 08.

Nicholson, C., Sorlien, C.C., Atwater, T., Crowell, J.C., and Luyendyk, B.P., 1994, Microplate capture, rotation of the western Transverse Ranges, and initiation of the San Andreas transform as a low-angle fault system: Geology, v. 22, p. 491–495, doi:10.1130/0091-7613(1994)022<0491:MCROTW>2.3.CO;2.

NOAA- NGDC, 2003, U.S. Coastal Relief Model Vol.6 - Southern California (3 second).: NOAA National Centers for Environmental Information., doi:10.7289/V500001J.

NOAA-NCEI, 2015, Orange County, California 1/3 arc-second NAVD 88 Coastal Digital Elevation Model: National Geophysical Data Center, NOAA. National Centers for Environmental Information, https://www.ncei.noaa.gov/metadata/geoportal/rest/metadata/item/gov.noaa.ngdc.mgg.dem:11506/html# (accessed June 2020).

Normark, W.R., and Piper, D.J.W., 1972, Sediments and Growth Pattern of Navy Deep-Sea Fan, San Clemente Basin, California Borderland: The Journal of Geology, v. 80, p. 198–223, doi:10.1086/627725.

Okubo, K., Rougier, E., Lei, Z., and Bhat, H.S., 2020, Modeling earthquakes with off-fault damage using the combined finite-discrete element method: Computational Particle Mechanics, v. 7, p. 1057–1072, doi:10.1007/s40571-020-00335-4.

Olmsted, F.H., 1958, Geologic Reconnaissance of San Clemente Island California: Contributions to General Geology: Geological Survey Bulletin, v. 1071-B, p. 55–68.

Parsons, B., and Sclater, J.G., 1977, An analysis of the variation of ocean floor bathymetry and heat flow with age: Journal of Geophysical Research, v. 82, p. 803–827, doi:10.1029/JB082i005p00803.

Patruno, S., Hampson, G.J., and Jackson, C.A.L., 2015, Quantitative characterisation of deltaic and subaqueous clinoforms: Earth-Science Reviews, v. 142, p. 79–119, doi:10.1016/j.earscirev.2015.01.004.

Peacock, D.C.P., and Sanderson, D.J., 1994, Geometry and development of relay ramps in normal fault systems: American Association of Petroleum Geologists Bulletin, v. 78, p. 147–165, doi:10.1306/bdff9046-1718-11d7-8645000102c1865d.

Peltier, W.R., and Fairbanks, R.G., 2006, Global glacial ice volume and Last Glacial Maximum duration from an extended Barbados sea level record: Quaternary Science Reviews, v. 25, p. 3322–3337, doi:10.1016/j.quascirev.2006.04.010.

Philibosian, B., Fumal, T., and Weldon, R., 2011, San Andreas Fault Earthquake Chronology and Lake Cahuilla History at Coachella, California: Bulletin of the Seismological Society of America, v. 101, p. 13–38, doi:10.1785/0120100050.

Platt, J.P., and Becker, T.W., 2010, Where is the real transform boundary in California? Geochemistry, Geophysics, Geosystems, v. 11, p. 1–19, doi:10.1029/2010GC003060.

Plesch, A., Marshall, S.., Nicholson, C., Shaw, J.H., Maechling, P.., and Su, M., 2020, The Community Fault Model version 5.3 and new web-based tools: Poster Presentation at 2020 SCEC Annual Meeting. SCEC Contribution 10547, v. 08.

Posamentier, H., Allen, G., and James, D., 1992, High Resolution Sequence Stratigraphy--The East Coulee Delta, Alberta: SEPM Journal of Sedimentary Research, v. Vol. 62, p. 310–317, doi:10.1306/D42678ED-2B26-11D7-8648000102C1865D.

Ridlon, J.B., 1972, Pleistocene-holocene deformation of the san clemente island crustal block, california: Bulletin of the Geological Society of America, v. 83, p. 1831–1844, doi:10.1130/0016-7606(1972)83[1831:PDOTSC]2.0.CO;2.

Rivero, C., Shaw, J.H., and Mueller, K., 2000, Oceanside and thirtymile bank blind thrust: Implications for earthquake hazards in coastal Southern California: Geology, v. 28, p. 891–894, doi:10.1130/0091-7613(2000)028<0891:OATBBT>2.3.CO;2.

Rockwell, T.K., and Klinger, Y., 2019, Final Technical Report Testing Recurrence Models for a Simple Plate Boundary Fault : Continuation of a Paleoseismic Study of the Imperial Fault in the Region of Large 1940 Displacement: USGS NEHRP Award No. G18AP00004,.

Rockwell, T.K., and Klinger, Y., 2013, Surface Rupture and Slip Distribution of the 1940 Imperial Valley Earthquake, Imperial Fault, Southern California: Implications for Rupture Segmentation and Dynamics: Bulletin of the Seismological Society of America, v. 103, p. 629–640, doi:10.1785/0120120192.

Rockwell, T.., and Meltzner, A.J., 2008, Non-characteristic slip and earthquake clustering on the Imperial fault, Mesquite Basin, Imperial Valley, California.: In AGU Fall Meeting Abstracts, v. T11A-1845.

Rockwell, T.., Meltzner, A., and Tsang, R., 2011, A long record of earthquakes with timing and displacements for the Imperial fault: A test of earthquake recurrence models: Final Technical Report, U.S. Geological Survey, p. 1–28.

Rockwell, T.K., Muhs, D.R., Kennedy, G.L., Hatch, M.E., Wilson, S.H., and Klinger, R.E., 1989, Uranium-Series Ages, Faunal Correlations and Tectonic Deformation of Marine Terraces Within the Agua Blanca Fault Zone at Punta Banda, Northern Baja California, Mexico, *in* In: Abbott, P.L. (Ed.), Geologic Studies in Baja California, Los Angeles, Pacific Section, Society of Economic Paleontologists and Mineralogists Book, v. 63, p. 1–16, papers3://publication/livfe/id/88733%5Cnpapers3://publication/uuid/8E13F081-8D35-4F85-AC1E-CBAEA995C7D1.

Romanyuk, T., Mooney, W.D., and Detweiler, S., 2007, Two lithospheric profiles across southern California derived from gravity and seismic data: Journal of Geodynamics, v. 43, p. 274–307, doi:10.1016/j.jog.2006.09.011.

Ross, Z.E., Trugman, D.T., Hauksson, E., and Shearer, P.M., 2019, Searching for hidden earthquakes in Southern California: v. 771, p. 767–771.

Ryan, H.F., Conrad, J.E., Paull, C.K., and McGann, M., 2012, Slip rate on the San Diego trough fault zone, inner California Borderland, and the 1986 Oceanside earthquake swarm revisited: Bulletin of the Seismological Society of America, v. 102, p. 2300–2312, doi:10.1785/0120110317.

Ryan, H.F., Legg, M.R., Conrad, J.E., and Sliter, R.W., 2009, Recent faulting in the Gulf of Santa Catalina : San Diego to Dana Point: The Geological Society of America. Special Paper 454, p. 291–315, doi:10.1130/2009.2454(4.5).

Sahakian, V., Bormann, J., Driscoll, N., Harding, A., Kent, G., and Wesnousky, S., 2017, Seismic constraints on the architecture of the Newport-Inglewood/Rose Canyon fault: Implications for the length and magnitude of future earthquake ruptures: Journal of Geophysical Research: Solid Earth, v. 122, p. 2085–2105, doi:10.1002/2016JB013467.

Sahakian, V., Kell, A., Harding, A., Driscoll, N., and Kent, G., 2016, Geophysical Evidence for a San Andreas Subparallel Transtensional Fault along the Northeastern Shore of the Salton Sea: Bulletin of the Seismological Society of America, v. 106, p. 1963–1978, doi:10.1785/0120150350.

Sandwell, D.T., Gonzalez-Ortega, A., Gonzalez, J., and Thatcher, W.R., 2016, 2016 SCEC Annual Report Assembly of the Community Geodetic Model and GPS Survey of the Cerro Prieto Fault: Proposal 16072, p. 1–7, https://urldefense.proofpoint.com/v2/url?u=https-3A__files.scec.org_s3fs-2Dpublic_reports_2016_16072-5Freport.pdf&d=DwQFAg&c=-35OiAkTchMrZOngvJPOeA&r=sPv2o51sZLASnRk9ctYcXOWh73_EcBJaw--

4qtWyOec&m=JdCkNKOWhkQGdku3B5vkmDX6qIjIjhKfURZO14pXzthst17haSzvO31aacF.

Savage, K.L., and Weigand, P.W., 1994, Petrology and Geochemistry of the Volcanic Clasts from the Miocene Blanca Formation, Santa Cruz Island, California: 74–87 p.

Schumann, R.R., Minor, S.A., Muhs, D.R., Groves, L.T., and McGeehin, J.P., 2012, Tectonic influences on the preservation of marine terraces: Old and new evidence from Santa Catalina Island, California: Geomorphology, v. 179, p. 208–224, doi:10.1016/j.geomorph.2012.08.012.

Schwartz, D., 2019, Large Coherent Block Versus Microplate Rotation of the Western Transverse Range : a New Examination of Paleomagnetic Constraints: University of California, San Diego, 1–40 p., https://escholarship.org/uc/item/9605873g.

Severinghaus, J.P., and Atwater, T., 1990, Cenozoic geometry and thermal state of the subducting slabs beneath western North America: Basin and Range extensional tectonics near the latitude of Las Vegas, Nevada, v. 176, p. 1–22, doi:10.1130/MEM176-p1.

Shanmugam, G., and Moiola, R.J., 1982, Eustatic control of turbidites and winnowed turbidites: Geology, v. 10, p. 231–235, https://pubs.geoscienceworld.org/geology/article/11/1/58/186048.

Sharp, R.V., 1980, 1940 and Prehistoric earthquake displacements on the Imperial fault, Imperial and Mexicali Valleys, California and Mexico: California Seismic Safety Commission Symposium Proceedings, The Human Settlements on the San Andreas Fault, p. 68–81.

Smith, P.B., 1960, Foraminifera of the Monterey Shale and Puente Formation, Santa Ana Mountains and San Juan Capistrano Area, California: Geological Survey Professional Paper, v. 294–M.

Smith, W.S.T., 1933, Marine terraces on Santa Catalina Island: American Journal of Science, v. 146, p. 123–136.

Smith, W., and Sandwell, D., 2004, Conventional Bathymetry, Bathymetry from Space, and Geodetic Altimetry: Oceanography, v. 17, p. 8–23, doi:10.5670/oceanog.2004.63.

Sonder, L.J., and Jones, C.H., 1999, WESTERN UNITED STATES EXTENSION: How theWest was Widened: Annual Review Earth Planet Science, p. 417–462.

Southard, J.B., 1991, Experimental Determination of Bed-form Stability: Annual Review Earth Planet Science, v. 19, p. 423–455, https://doi.org/10.1146/annurev.ea.19.050191.002231.

St.-Onge, G., Mulder, T., Piper, D.J.W., Hillaire-Marcel, C., and Stoner, J.S., 2004, Earthquake and flood-induced turbidites in the Saguenay Fjord (Québec): A Holocene paleoseismicity record: Quaternary Science Reviews, v. 23, p. 283–294, doi:10.1016/j.quascirev.2003.03.001.

Stephenson, W.J., Rockwell, T.K., Odum, J.K., Shedlock, K.M., and Okaya, D.A., 1995, Seismic Reflection and Geomorphic Characterization of the Onshore Palos Verdes Fault Zone, Los Angeles, California: Bull. Seismol. Soc. Am., v. 85, p. 943- 950.

Teng, L.S., and Gorsline, D.S., 1989, Late Cenozoic sedimentation in California Continental Borderland basins as revealed by seismic facies analysis: Geological Society of America

Bulletin, v. 101, p. 27–41, doi:10.1130/0016-7606(1989)101<0027:LCSICC>2.3.CO;2.

Thomas, A.., and Rockwell, T.., 1996, A 300-to 550-year history of slip on the Imperial fault near the US-Mexico border: Missing slip at the Imperial fault bottleneck: Journal of Geophysical Research: Solid Earth, v. 101, p. 5987–5997.

Thompson, W.G., and Goldstein, S.L., 2006, A radiometric calibration of the SPECMAP timescale: Quaternary Science Reviews, v. 25, p. 3207–3215, doi:10.1016/j.quascirev.2006.02.007.

Thorkelson, D.J., 1996, Subduction of diverging plates and the principles of slab window formation: Tectonophysics, v. 255, p. 47–63, doi:10.1016/0040-1951(95)00106-9.

Toda, S., Stein, R.S., Richards-Dinger, K., and Bozkurt, S.B., 2005, Forecasting the evolution of seismicity in southern California: Animations built on earthquake stress transfer: Journal of Geophysical Research: Solid Earth, v. 110, p. 1–17, doi:10.1029/2004JB003415.

Trifunac, M.., and Brune, J.., 1970, Complexity of Energy Release During the Imperial Valley, California, Earthquake of 1940: Bulletin of the Seismological Society of America, v. 60, p. 137–160.

U.S. Geological Survey Quaternary fault and fold database for the United States:, https://www.usgs.gov/natural-hazards/earthquake-hazards/faults (accessed August 2021).

Vedder, J.G., 1990, Maps of California continental borderland showing compositions and ages of bottom samples acquired between 1968 and 1979, U.S. Geologic Survey Miscellaneous Field Studies Map 2122.:, doi:https://doi.org/10.3133/mf2122.

Vedder, J.G., and Howell, D.G., 1976, Review of the Distribution and Tectonic Implications of Miocene Debris From the Catalina Schist, California Continental Borderland and Adjacent Coastal Areas: 326–340 p.

Vedder, J.G., and Howell, D.G., 1980, Topographic Evolution of the Southern California Borderland During Late Cenozoic Time: proceedings of a multidisciplinary symposium, v. SantaBarba, p. 7–32.

Vedder, J.G., Howell, D.G., and Forman, J.A., 1979, Miocene strata and their relation to other rocks Santa Catalina Island, CA, *in* Cenozoic paleogeography of the western United States, p. 239–256.

Vedder, J.G., and Moore, E.J., 1976, Paleoenvironmental implications of fossiliferous Miocene and Pliocene strata on San Clemente Island, California.:

Van Wagoner, J.C., Mitchum, R.M., Campion, K.M., and Rahmanian, V.D., 1990, Siliciclastic sequence stratigraphy in well logs, core, and outcrops: concepts for high-resolution correlation of time and facies: American Association of Petroleum Geologists Methods in Exploration Series, v. 7, p. 55, doi:https://doi.org/10.1306/Mth7510.

Walton, M.A.L., Brothers, D.S., Conrad, J.E., Maier, K.L., Roland, E.C., Kluesner, J.W., and Dartnell, P., 2020, Morphology , structure , and kinematics of the San Clemente and Catalina faults based on high-resolution marine geophysical data , southern California Inner Continental Borderland ( USA ): Geosphere, v. 16, p. 1–24, doi:https://doi.org/10.1130/GES02187.1.

Ward, S.N., and Valensise, G., 1996, Progressive growth of San Clemente Island, California, by blind thrust faulting: Implications for fault slip partitioning in the California Continental Borderland: Geophysical Journal International, v. 126, p. 712–734, doi:10.1111/j.1365-246X.1996.tb04699.x.

Ward, S.N., and Valensise, G., 1994, The Palos Verdes terraces, California: bathtub rings from a buried reverse fault: Journal of Geophysical Research, v. 99, p. 4485–4494, doi:10.1029/93JB03362.

Weigand, P.W., 1994, Petrology and Geochemistry of Miocene Volcanic Rocks from Santa Catalina and San Clemente Islands, California:

Weissel, J.K., and Karner, G.D., 1989, Flexural uplift of rift flanks due to mechanical unloading of the lithosphere during extension: Journal of Geophysical Research: Solid Earth, v. 94, p. 13919–13950, doi:10.1029/JB094iB10p13919.

Wesnousky, S.G., 2005, Active faulting in the Walker Lane: Tectonics, v. 24, p. 1–35, doi:10.1029/2004TC001645.

Wesnousky, S.G., 2008, Displacement and Geometrical Characteristics of Earthquake Surface Ruptures: Issues and Implications for Seismic-Hazard Analysis and the Process of Earthquake Rupture: Bulletin of the Seismological Society of America, v. 98, p. 1609–1632, doi:10.1785/0120070111.

Wessel, K.N., 2016, 500 Year Rupture History of the Imperial Fault At the International Border Through Analysis of Faulted Lake Cahuilla Sediments, Carbon-14 Data, and Climate Data: M.S. thesis, Geological Sciences, San Diego State University, San Diego, CA, USA.,.

Wright, T.L., 1991, Structural Geology and Tectonic Evolution of the Los Angeles Basin, California: in Biddle, K.T., ed., Active margin basins: American Association of Petroleum Geologists Memoir 52, v. 52, p. 35–134.

Zavala, C., and Arcuri, M., 2016, Intrabasinal and extrabasinal turbidites: Origin and distinctive characteristics: Sedimentary Geology, v. 337, p. 36–54, doi:10.1016/j.sedgeo.2016.03.008.